RETROGRESSIVE THAW SLUMPS: INDICATORS OF HOLOCENE CLIMATE CHANGES IN THE RICHARDSON MOUNTAINS-PEEL PLATEAU, NORTHWESTERN CANADA

Roxanne Frappier

Laboratory for Paleoclimatology and Climatology (LPC)
CryoLab for Arctic, Antarctic and Planetary Studies (CLAAPS)

A Thesis Submitted to the
Faculty of Graduate and Postdoctoral Studies
in Partial Fulfillment of the Requirements
for the Degree of
Master of Science in Geography

uOttawa

L'Université canadienne
Canada's university

Department of geography, environment and geomatics
University of Ottawa

Abstract

The ongoing climate warming is expected to increase thermokarst activity and their impacts by inducing permafrost degradation and active layer deepening. A retrogressive thaw slump, which represents the most dynamic thermokarst landform, was investigated in the Richardson Mountains-Peel Plateau region. The exposed material at the thaw slump represents an opportunity to characterize the cryostratigraphy of the uppermost 5 m of permafrost. Analyses of the stratigraphy, sedimentology, isotope geochemistry and radiocarbon dating is presented. Six sites were also identified on an elevation-vegetation gradient to provide complementary data on thaw layer thickness. Summer air temperatures, vegetation cover type, mesoscale conditions modifying the snowpack, timing of the snow accumulation and winter air temperature inversions are identified as the main drivers of thaw layer thickness in the region. The physical and chemical parameters of the massive ground ice exposed at the thaw slump are characteristic of buried glacier ice that experienced water infiltration and partial refreezing. The layer between the massive ground ice units and the thaw layer in the thaw slump is identified as a relict thaw layer and represents the period of maximum active layer deepening. It dates to the Holocene thermal maximum, which represents a period of important thermokarst activity that resulted in widespread paleo-thaw unconformities across northwestern Canada. Association of the region's thaw slump activity with paleoclimatic parameters provide indication that the combination of formerly glaciated continuous permafrost, hummocky rolling moraine terrain, stream-incised relief, and massive ground ice, coupled with major rainfall events, represents a set of condition that is favourable to thaw slump activity.

Résumé

Il est prévu que le réchauffement climatique en cours aura pour effet d'augmenter les activités thermokarstiques et leurs impacts, en induisant la dégradation du pergélisol et l'approfondissement de la couche active. Un glissement de fonte régressif, la forme thermokarstique la plus dynamique, a été étudié dans la région des Monts Richardson et du Plateau de la Peel. Le matériel exposé dans le glissement de fonte représente une opportunité de caractériser la cryostratigraphie des cinq premiers mètres du pergélisol. Les analyses de la stratigraphie, la sédimentologie, la géochimie isotopique et la datation au radiocarbon sont présentées. Six sites ont été identifiés sur un gradient d'élévation-végétation pour fournir des données complémentaires sur l'épaisseur de la couche de dégel. Les températures de l'air en été, le type de végétation, les conditions à moyenne échelle qui modifient le manteau neigeux, le timing de l'accumulation de la neige et les inversions de température de l'air en hiver sont identifiés comme les principaux déterminants de l'épaisseur de la couche de dégel dans la région. Les paramètres physiques et chimiques de la glace massive exposée au glissement de fonte sont caractéristiques de la glace de glacier enfouie qui a fait l'expérience d'infiltration d'eau et de regel partiel. La couche qui se trouve entre les unités de glaces massives et la couche de dégel dans le glissement de fonte est identifiée comme une paléo-couche active qui représente la période d'approfondissement de la couche active maximal. Elle date du maximum thermique de l'Holocène, une période d'activité thermokarstique importante qui a mené à une discordance de paléo-fonte répandue à travers le nord-ouest du Canada. L'association de l'activité des glissements de fonte de la région avec certains paramètres paléoclimatique permet d'indiquer que la combinaison d'un pergélisol continu qui a été englacé, d'un terrain de moraines vallonné caractérisé par la présence d'hummocks, d'un relief incisé par les cours d'eau and de glace massive dans le sol, couplés avec des évènements de précipitations majeures, représente un ensemble de conditions favorable à l'activité des glissements de fonte.

Acknowledgements

Cette recherche a été financée par le Conseil de Recherches en Sciences Naturelles et en Génie du Canada (CRSNG), le Programme du Plateau Continental Polaire (PPCP) et le Programme de Formation Scientifique dans le Nord (PFSN). Je suis reconnaissante de leur support pour l'accomplissement de ce projet.

J'aimerais remercier mes deux superviseurs, Dr. Denis Lacelle and Dr. André Viau, pour leurs précieux conseils. Je crois que vos spécialités et perspectives respectives ajoutent à ma thèse, et c'est pourquoi je me considère chanceuse d'avoir eu l'opportunité de vous avoir tous les deux en tant que superviseur. Denis, merci pour ton humeur toujours calme et rassurante tout au long du travail de terrain et de laboratoire. André, merci de ne pas m'avoir laisser m'égarer pendant l'accomplissement de ma maîtrise.

Un grand merci à mes collègues et amis, B. Faucher et M. Verret, pour votre aide sur le terrain et au laboratoire. Je serai toujours reconnaissante de votre total dévouement lors du sondage de l'épaisseur de la couche active.

Thank you to S. Kokelj for his assistance in the field regarding the thaw layer thickness sites. A warm thank you to Christine, our gwich'in guide, for keeping us safe during our field work and telling us captivating stories about your people and your land.

I would like to thank the staff at the A.E. Lalonde AMS Laboratory and at the G.G. Hatch Stable Isotope Laboratory for their work, especially C. Crann and S. Murseli for teaching me about the methods of radiocarbon dating.

Merci à J. Bjornson. Tu m’as aidé à de nombreux niveaux, de mon application à la maîtrise au travail de laboratoire et j’en suis très reconnaissante. Aussi, F. Oliva, merci. Peut-être que tu ne le sais pas, mais notre conversation à l’extérieur du Café-Alt a tout changé.

Sur une note plus personnelle, j’aimerais remercier mes parents, Gilles et Caroline. La fierté dans vos yeux est une source infinie de motivation. Merci pour tout. Merci à David qui me soutient toujours, tout en m’aidant à garder les pieds sur terre. Merci aussi à ma sœur Sophie, mes four french Canadians et les membres de ma famille pour leurs nombreux encouragements. Je ne vous dirai jamais assez à quel point votre support a fait toute la différence tout au long de mon parcours.

Table of Contents

Abstract ii
Résumé iii
Acknowledgements iv
List of Figures viii
List of Acronyms x
Chapter 1: Introduction 1
1.1 Research Questions and Objectives 2
Chapter 2: Background 3
2.1 Permafrost 3
2.1.1 Ground Ice 5
2.1.2 Thermokarst Terrain 9
2.1.3 Retrogressive thaw slumps 11
2.2 Climate changes 13
2.2.1 Climate Changes since the Last Glacial Maximum 14
2.3 Climate changes and permafrost 17
Chapter 3: Study Area 19
3.1 Geology and physiography 19
3.2 Vegetation 22
3.3 Climate 24
3.4 Glaciation 26
3.6 Climate history and permafrost conditions 27
Chapter 4: Methodologies 31
4.1 Determination of Thickness of Thaw Layer 31
4.2 Sampling of Thaw Layer and Permafrost at Thaw Slump 31
4.3 Ground Ice Analyses 33
4.3.1 Samples Preparation 33
4.3.2 Major Ions 34
4.3.3 Stable Isotopes 34
4.3.4 Radiocarbon dating of Dissolved Organic Carbon 35
4.4 Thaw layer and Permafrost Soil Analyses 37

4.4.1 Particle Size Analysis 37
4.4.2 Water Content and Organic Carbon Content 38
4.4.3 Radiocarbon Dating of organics 39
Chapter 5: Results 40
5.1 Stratigraphy 40
5.1.1 Thaw Layer 41
5.1.2 Relict Thaw Layer 42
5.1.3 Massive Ice 42
5.2 Sedimentology 42
5.2.1 Thaw Layer 42
5.2.2 Relict Thaw Layer 44
5.2.3 Unit 2 44
5.3 Geochemistry 44
5.3.1 Dissolved Organic Carbon 44
5.3.2 Major Ions 44
5.3.3 Stable Isotopes 45
5.4 Age Determination 49
Chapter 6: Discussion 51
6.1 Thaw Layer Thickness 51
6.2 Massive Ground Ice Origin 53
6.3 Relict Thaw Layer 56
6.4 Thaw Slump Activity during the Holocene 57
Chapter 7: Conclusions 64
7.1 Conclusions 64
7.2 Limitations of Study 65
7.3 Future Work 66
References 67
APPENDIX A: LABORATORY ANALYSES RESULTS 78
APPENDIX B: A.E. LALONDE AMS LABORATORY RESULTS 95
APPENDIX C: EXTERNAL DATA 98
APPENDIX D: R CODE 99

List of Figures

Fig. 2.1 Permafrost thermal regime and terminology. (from French, 1996)……4

Fig. 2.2 Cryostratigraphic evidence of the thawing and refreezing of permafrost. T-U^1 is the primary thaw unconformity at the top of permafrost (A). When thawing occurs, T-U^1 deepens (B), and when refreezing occurs, it moves back towards the surface, leaving T-U^2, a paleo-thaw unconformity, as evidence of previous thawing (C). (from French, 2007)……..…11

Fig. 2.3 Modulation of summer insolation by eccentricity near 100 000 years. (from Ruddiman, 2008)……..……14

Fig. 3.1 Study area map showing sampling sites and other locations mentioned in this thesis……..……..……..……..……..……..……..……..……..……..……..……..……..……..……..……..……...19

Fig. 3.2 Surficial geology of the study area……..……..……...21

Fig. 3.3 Ecoregions of the study area……..……...……23

Fig. 3.4 Mean air temperatures in Old Crow, YK (1952-2007), Fort McPherson, NWT (1985-2007) and Inuvik, NWT (1957-2006). Trends based on an average of the three stations. Pearson Product-Moment Correlation Coefficient shown for trends as r(*df*)=*a*, p=*b*, where *df* is the degree of freedom, *a* is the correlation coefficient and *b* is the p-value.……..……24

Fig. 3.5 Total annual precipitation in Old Crow, YK (1952-2007), Fort McPherson, NWT (1985-2007) and Inuvik, NWT (1957-2006). Trends based on an average of the three stations. Pearson Product-Moment Correlation Coefficient shown for trends as r(*df*)=*a*, p=*b*, where *df* is the degree of freedom, *a* is the correlation coefficient and *b* is the p-value.……..……25

Fig. 4.1 Photograph of the thaw layer at Roger Thaw Slump, NWT, on August 1st 2016 (RTS; 67°37'05.2"N, 135°33'23.2"W, 350 m a.s.l.)……..…..……32

Fig. 4.2 Photograph of the headwall at Roger Thaw Slump, NWT, on August 1st 2016, showing the four massive ice units, and the limit of the relict thaw layer (RTL) (RTS; 67°37'05.2"N, 135°33'23.2"W, 350 m a.s.l.)……..……33

Fig. 5.1 Field photograph taken at Roger Thaw Slump, NWT on August 1st 2016 (RTS; 67°37'05.2"N, 135°33'23.2"W, 350 m a.s.l.). **A.** Overview of the headwall showing the paleo-thaw unconformity delimiting the relict thaw layer (RTL) and the four massive ice units sampling sites. **B.** Close up on the eastern part of the headwall showing the extent of Unit 4, the relict thaw layer (RTL) and the thaw layer (TL) **C.** Unit 4 overlain by the relict thaw layer (RTL) and thaw layer (TL) **D.** Unit 1, 2 and 3 overlain by the relict thaw layer (RTL)……..……40

Fig. 5.2 Depth model showing thaw layer thickness from surface in different vegetation types on an elevation gradient in the Richardson Mountains-Peel Plateau region. Mean depth is shown as μ = x. **A.** Grassy Alpine Tundra (GAT; 957 m a.s.l.) **B.** Hummocky Alpine Tundra (HAT; 790 m

a.s.l.) **C.** Sub-alpine Tundra (SAT; 611 m a.s.l.) **D.** Dwarf Shrub Tundra (DST; 493 m a.s.l.) **E.** Tall Shrub Tundra (TST; 425 m a.s.l.) **F.** Lowland Spruce Forest (LSF; 31 m a.s.l.)……...….41

Fig. 5.3 **A.** Gravimetric water content (GWC), grain size, organic carbon content, Deuterium excess, $\delta^{18}O$, and radiocarbon dates of the thaw layer and relict thaw layer at Roger Thaw Slump ,NWT (RTS; 67°37'05.2"N, 135°33'23.2"W, 350 m a.s.l.). Dashed line represents thaw layer thickness on August 1st 2016. Below is the relict thaw layer (RTL) **B.** Radiocarbon dates inset.……43

Fig. 5.4 Dissolved organic carbon (DOC) and $\delta^{13}C$ concentrations of ice from the relict thaw layer (RTL) and four massive ice units samples taken at Roger Thaw Slump, NWT (RTS; 67°37'05.2"N, 135°33'23.2"W, 350 m a.s.l.).……..……45

Fig. 5.5 Major anions and cations profile of ice from the relict thaw layer (RTL) and four massive ice units samples taken at Roger Thaw Slump, NWT (RTS; 67°37'05.2"N, 135°33'23.2"W, 350 m a.s.l.).……..……..46

Fig. 5.6 Stable water isotope composition ($\delta^{18}O$ and Deuterium Excess) of ground water from the thaw layer (TL), ice from the relict thaw layer (RTL) and four massive ice units samples taken at Roger Thaw Slump, NWT (RTS; 67°37'05.2"N, 135°33'23.2"W, 350 m a.s.l.).……..……..47

Fig. 5.7 δD and $\delta^{18}O$ scatter plot of ground water from the thaw layer (TL), ice from the relict thaw layer (RTL) and four massive ice units samples taken at Roger Thaw Slump ,NWT (RTS; 67°37'05.2"N, 135°33'23.2"W, 350 m a.s.l.). LMWL = Local Meteoric Water Line for Inuvik, NWT ($\delta D = 7.3\ \delta^{18}O - 3.37$; Lacelle, 2011). Pearson Product-Moment Correlation Coefficient shown as r(*df*)=*a*, p=*b*, where *df* is the degree of freedom, *a* is the correlation coefficient and *b* is the p-value.……48

Fig. 5.8 δD and D-Excess scatter plot of ground water from the thaw layer (TL), ice from the relict thaw layer (RTL) and four massive ice units samples taken at Roger Thaw Slump, NWT (RTS; 67°37'05.2"N, 135°33'23.2"W, 350 m a.s.l.)..……...…….49

Fig. 5.9 Radiocarbon dating results.……...…50

Fig. 6.1 Insolation (July 65°N, Berger and Loutre, 1991), July temperature, January temperature and annual precipitation anomalies for western Canada (Viau and Gajewski, 2009), elevation of thaw slumps in the Bonnet Plume Creek terraces and at Roger Thaw Slump (Lacelle et al., 2010; this study), and thaw slumps activity in the Richardson Mountains region (Lacelle et al., 2004; this study). The light gray area represents the extent of the Holocene Thermal Maximum, and the dark gray shaded area represents the extent of the Little Ice Age.……..58

Fig. 6.2 Comparison of shotholes massive ice occurrence at given depths between the Last Glacial Maximum (LGM) and the Tutsieta Lake Phase, and between the Tutsieta Lake Phase and the Peel River.……..……62

List of Acronyms

ACIA	Arctic Climate Impact Assessment
AMS	Accelerator Mass Spectrometer
ARC	Advanced Research Complex
a.s.l.	Above Sea Level
CF-IRMS	Continuous-Flow Isotope Ratio Mass Spectrometer
CLIMAP	Climate: Long range Investigation, Mapping, and Prediction
CRREL	Cold Regions Research Engineering Laboratory
DIC	Dissolved Inorganic Carbon
DOC	Dissolved Organic Carbon
EA	Elemental Analyzer
GWC	Gravimetric Water Content
HTM	Holocene Thermal Maximum
ICP-AES	Inductively Coupled Plasma Atomic Emission Spectrometer
IPA	International Permafrost Association
IPCC	Intergovernmental Panel on Climate Change
LGM	Last Glacial Maximum
LGR	Los Gatos Research
LOI	Loss On Ignition
MAAT	Mean Annual Air Temperature
NDIR	Non-Destructive Infrared
OA-ICOS	Off-Axis Integrated Cavity Output Spectroscopy
RTL	Relict Thaw Layer
RTS	Roger Thaw Slump

SCI	Spectral Contamination Identifier
TL	Thaw Layer
TLT	Thaw Layer Thickness
VSMOW	Vienna Standard Mean Ocean Water
WCO	Wet Chemical Oxidation
$\delta^{13}C_{DOC}$	Delta ^{13}C of Dissolved Organic Carbon

Chapter 1: Introduction

Permafrost degradation in Arctic regions has gained attention in recent years, mostly because of the ongoing climate warming, which is enhanced in Arctic regions (IPCC, 2013). In ice-rich permafrost terrain, permafrost degradation can lead to the formation of thermokarst terrain, landscapes that are characterized by irregular topography that result from the subsidence of the ground following the thawing and the subsequent release of excess water (Harry, 1986; Van Everdingen, 1998). Multiple thermokarst landforms can be found in permafrost terrain (i.e., mounds, slumps, lakes and depressions, such as retrogressive thaw slumps, collapsed pingos, and thaw lakes), the most impressive being retrogressive thaw slumps (Burn and Lewkowicz, 1990). Thaw slumps frequently expose meters to tens of meters of permafrost terrain and offer an opportunity to examine the cryostratigraphy of permafrost. Periods of permafrost aggradation and degradation are logged into frozen soils as cryostratigraphic evidence such as paleo-thaw unconformities, truncated ice bodies and variations in cryostructures. Studying cryostratigaphy in combination with isotopic geochemistry and dating, and multiple proxy data allows for a better understanding of the genesis of permafrost terrain and its climatic significance, which is notably relevant in the context of the study of Holcoene climate changes (French and Shur, 2010; French, 2007).

This thesis focuses on describing the cryostratigraphy of permafrost at a site in the Richardson Moutains-Peel Plateau region, NWT, Canada. The region is underlain by ice-rich permafrost as inferred from the presence of nearly 200 active thaw slumps. However most of the thaw slumps (70%) are concentrated between the maximum extent of the Laurentide Ice Sheet and a recessional limit (Lacelle et al., 2015). Past studies in the region determined the origin and age

of ground ice and timing of past thaw slumping at sites near the maximum extent of the Laurentide Ice Sheet (Lacelle et al., 2004; 2010; 2013); here the first site within the recessional limit of the LIS is investigated. This thesis will contribute to reconstruct the overall regional glacial and permafrost history in the Richardson Moutains-Peel Plateau region. It is organized in a series of chapters: Ch. 1) introduction to the thesis along with the research questions and objectives; Ch. 2) background on the subjects of permafrost, thaw slumps, and climate changes; Ch. 3) description of the study area; Ch. 4) methodologies used during this project; Ch. 5) the results; Ch. 6) discussion of the results; Ch. 7) the conclusions, limitations of this study, and future work to be undertaken.

1.1 Research Questions and Objectives

The main goal of the thesis is to characterize the cryostratigraphy of the uppermost 5 m of permafrost at a site on the lower Peel Plateau, NWT. The specific objectives of the thesis are to determine:

a) The origin and age of the ground ice exposed in a retrogressive thaw slump;
b) The response of permafrost to Holocene climate changes.

Chapter 2: Background

2.1 Permafrost

Permafrost is, by definition, ground that remains at or below 0°C for at least two consecutive years (French, 1996). However, it may or may not be frozen depending on whether water or ice is present or absent in the soil. In addition, unfrozen water may exist in permafrost for several reasons such as 1) a depression of the standard melting point due to the dilution of solutes from the soil, 2) particles' surface melting where free energy is reduced by a melted layer at the surface of solid particles and 3) the presence of curved surface particles where the surface energy varies upon freezing because of the associated change in surface area, known as the Gibbs-Thomson effect (Sparrman et al., 2004). Therefore, not all water freezes at 0°C and, in certain frost-susceptible soils, as much as 40% of water content may remain unfrozen at −1°C (French, 1996). The terms "cryotic" and "non-cryotic" are used to clarify the difference between the state and the temperature of permafrost. These terms refer to the temperature of the ground material itself (van Everdingen, 1998). Cryotic is synonymous with permafrost, meaning that the ground could be frozen or unfrozen, that is contain water in its solid or its liquid state, and still be at a temperature below 0°C. Non-cryotic means that the ground temperature is above 0°C.

Permafrost growth is determined by a balance between heat loss from ground surface and internal earth heat gain from depth. The deepest limit of permafrost, the permafrost base, is found where the temperature increase explained by the geothermal gradient offsets the amount by which the freezing point exceeds the mean surface temperature (Fig. 2.1) (French, 1996). The depth of the upper limit of the permafrost, the permafrost table, is determined by the thickness of the active layer, that is the layer that thaws and freezes seasonally (van Everdingen, 1998).

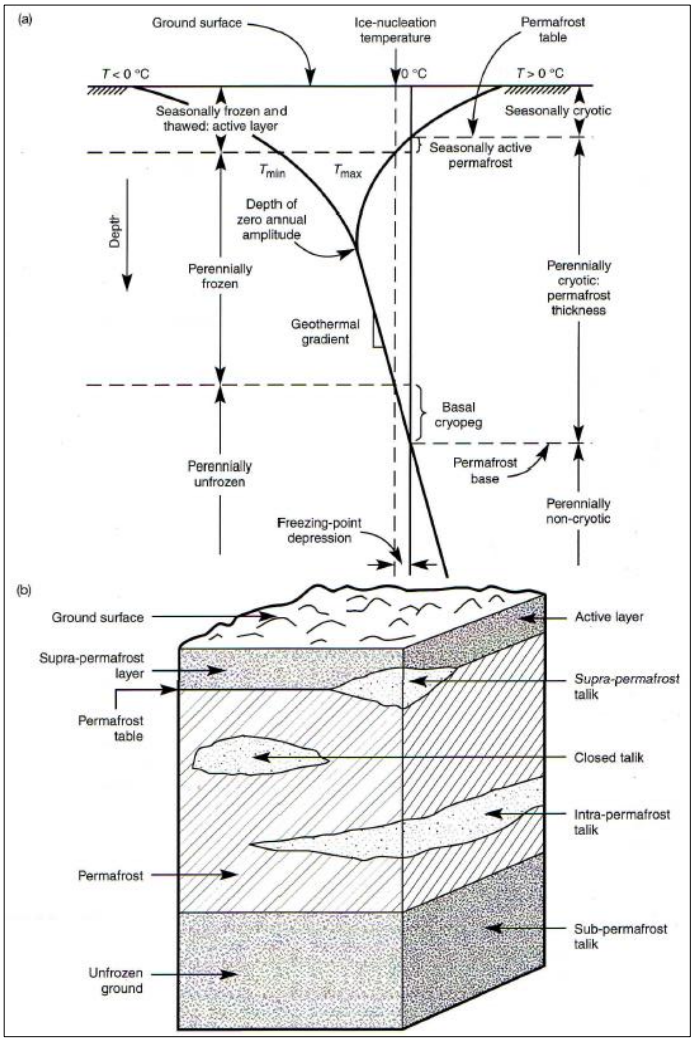

Fig. 2.1 Permafrost thermal regime and terminology. (from French, 1996)

Generally, the lower limit of the active layer is located at the depth where the maximum mean annual temperature is 0°C. However, the surface of the permafrost table can sometimes be separated from the active layer by a surficial water layer that thaws and freezes every year, but still remains cryotic. Some scientists propose that this seasonally active permafrost in terms of state, that is frozen or unfrozen, should still be included in the active layer (French, 1996).

2.1.1 Ground Ice

Ground ice is a key component in the study of permafrost. It refers to any type of ice present in frozen ground and can occur in many forms such as lenses, wedges, veins, sheets, seams, irregular masses, or individual crystals or coatings on mineral or organic particles (Van Everdingen, 1998). There are two quantitative parameters that define ground ice conditions: the ice content, which describes the percentage of ice to dry soil (French, 1996); and the excess ice, which represents the volume of water that exceeds the total pore volume that a frozen ground would have if unfrozen (Van Everdingen, 1998).

Ground ice is usually the product of four main freezing mechanisms. These include: 1) freezing of water that infiltrated from the surface by gravity along thermal contraction cracks, which creates single or multiple ice veins, or ice wedges, 2) *in situ* freezing of subsurface water, which forms crystals or grains of pore ice in the sediment interstices, 3) freezing of water that migrated to the freezing front, which creates lenses and layers of segregated ice and results in an ice-rich aggradational ice layer at the base of the active layer and sometimes in thick sheets of massive segregated ice and 4) freezing of moisture injected under pressure into permafrost sediments, which forms layers and flame-like bodies of intrusive ice (Harry, 1986). The freezing processes of ground ice can be identified by the cryostructures and cryotextures of frozen ground. The cryostructures define the type and arrangement of ice in the frozen ground, and cryotextures describe the grains or ice crystals size and shape and the contacts between them (French, 1996).

In northwestern Canada, massive ground ice bodies are commonly attributed to two different origins: 1) segregated-intrusive ice or 2) buried glacier ice (French and Harry, 1988, 1990; French and Pollard, 1986; Harry, French and Pollard, 1988; Mackay, 1971, 1973; Rampton, 1988).

Theoretically, segregated ice is formed by freezing of groundwater that migrated through soil pores to the freezing front, and intrusive ice is formed by freezing of moisture injected under pressure into permafrost sediments and to the freezing front (Harry, 1986; Williams and Smith, 1989). Segregated ice is usually aligned horizontally and presents bubbles elongated in the same direction, but it can also occur vertically as the result of lateral shrinkage of the soil that causes vertical cracks where ice lenses form (Mackay, 1974; Williams and Smith, 1989). Segregated ice is often found as aggradational ice layers at the base of the active layer, and sometimes as thick bodies of massive ground ice in the uppermost layers of permafrost (Harry, 1986; O'Neill and Burn, 2012). That is because when the permafrost table rises, it traps the aggradational ice layers and as segregated ice forms at the base of the active layer annually, this trapped ice grows vertically into an ice-rich zone at the top of permafrost (Mackay, 1972). In that case, the rate of permafrost aggradation is important because it determines the amount of segregated ice lenses that will be incorporated to this ice rich zone (Kokelj and Burn, 2003). Permafrost may aggrade because of a climate cooling (e.g., following the Holocene Thermal Maximum in Northwestern Canada; Burn 1988, 1997; Burn et al. 1986; Kokelj et al. 2002; Kokelj and Burn 2003; Mackay, 1978), or because of the thinning and retreat of an ice sheet (Rampton, 1984, 1978). Because segregated-intrusive ice is the result of freezing of water under equilibrium conditions, fractionation occurs and modifies the isotopic composition of both the water and the ice: the ice becomes enriched in the heavier isotopes (^{18}O and D) compared to the source water (Knight, 1997; Lacelle, 2011). In the case of freezing under equilibrium in a closed-system, if the water reservoir freezes entirely, the last layers to freeze will have a lighter isotopic composition because less heavy isotopes are available (Knight, 1997). The ice that is enriched in the heavier isotopes will have less negative

$\delta^{18}O$ values, which means that δD and $\delta^{18}O$ will plot on a lower regression slope compared to the local meteoric water line (LMWL) (Lacelle, 2011).

Glacier ice turns into buried glacier ice during deglaciation when a cover of till, originating from melt out of sediment-rich glacier ice, mass movement, lacustrine and aeolian processes, or glacial thrusting and shearing, is deposited on top of the ice (Harris and Murton, 2005; Moorman and Michel, 2000). The thickness of the deposit must exceed the active layer thickness to insulate the ice and keep it from atmosphere conditions and thawing. Basal glacier ice is the most susceptible to be preserved that way, because it would be rapidly insulated and integrated in the permafrost (Lacelle et al., 2004). That is why it is important to highlight the difference between the two types of glacier ice: 1) firnified glacier ice, and 2) basal glacier ice. The firnified ice represents the vast majority of the ice mass and it is the result of firnification processes that take place at or near the ice surface (Hubbard and Sharp, 1989). Because it is resulting from the compaction of snow which comes from meteoric precipitation, the isotopic composition of the ice will correspond to the LMWL (Knight, 1997). The ice at the base of a glacier is very different from this overlying firnified ice because it interacts with the bedrock (Waller, Murton and Knight, 2009). Basal ice usually has a high sediment content, with stratified debris in the lower layers and dispersed debris in the upper layers, and it is highly deformed, with layers, lenses and pods of different chemical composition (Hubbard and Sharp, 1989). The incorporation of sediment in the basal layers is due to regelation of basal water (Waller, Murton and Knight, 2009). Also, regelation (or refreezing) of water at the base of the glacier causes for changes in the isotopic composition of the ice. When basal glacier ice experiences refreezing of meltwater in a closed system, the first ice to form is characterized as being enriched in ^{18}O because of fractionation, and therefore δD-$\delta^{18}O$ will plot on a lower regression slope than for firnified glacier ice or the LMWL, similarly to

segregated-intrusive ice (Knight, 1997; Waller, Murton and Knight, 2009). However, if the freezing occurs in an open system, where the water reservoir is constantly fed with water that is isotopically lighter or if it is supplied with water from different sources, the isotopic composition can be similar to that of meteoric precipitation (Hubbard and Sharp, 1989; Knight, 1997). On the other hand, if the water input has the same isotopic composition as the initial water, the slope will be similar than that of the closed system (Hubbard and Sharp, 1989). However, basal glacier ice has been inferred has being the result of partial refreezing of basal meltwater which means it should normally show an enriched ^{18}O composition and a lower δD-$\delta^{18}O$ regression slope (Knight, 1997).

The differentiation between segregated-instrusive ice and buried glacier ice is therefore very difficult, as they may have a very similar appearance and isotopic composition (French and Harry, 1990; Lacelle, 2011). That is especially true if the ice is basal glacier ice, as it can theoretically be identified as segregated ice because of its high sediment content and its potential for enriched ^{18}O and D values (French and Harry, 1990; Hubbard and Sharp, 1989; Knight, 1997; Waller, Murton and Knight, 2009). A combination of the analysis of the ice physical and chemical parameters is then essential. Some diagnostic criteria described by French and Harry (1990) are taken into consideration. First, the contact between segregated-intrusive ice bodies and the enclosing (i.e., overlying or underlying) soil should be gradual and sediments can be suspended in the ice up to 20 cm beneath the contact, whereas for glacier ice the contact should be sharp (e.g., a thaw unconformity) and the ice must be older than the overlying material. Second, for segregated-intrusive ice, water chemistry should change following a trend continuing into the ice found in the surrounding sediments, and for buried glacier there should be no trend but rather a discontinuity between the massive body and the ice in the overlying sediments. Third, as explained above, if freezing took place under equilibrium in a closed system (e.g., segregated-intrusive ice

or basal glacier ice), the consequent isotopic fractionation will result in an enrichment of ^{18}O and D and in δD-$\delta^{18}O$ plotting on a lower regression slope (approx. 6) compared to the LMWL. Lacelle (2011) also identified a slope value between δD and $\delta^{18}O$ of less than 7.3 as indicative of freezing under equilibrium conditions. Because this threshold corresponds to the meteoric water line of our study area ($\delta D = 7.3\ \delta^{18}O - 3.37$), which is also true for a number of sites in the Arctic, the relation between δD and $\delta^{18}O$ might not help to differentiate the ice origin. The research made by Lacelle (2011) determined that considering the relation between D-Excess and δD is more efficient. In fact, it was shown that in freezing resulting of meteoric precipitation (i.e. firnified glacier ice), D-Excess and δD plot on a broad horizontal band with a very low slope (approx. 0.04), whereas in freezing of water under equilibrium conditions (i.e. segregated-intrusive ice or basal glacier ice), because of the depletion in δD due to fractionation, the ice is enriched in D-Excess, therefore D-Excess and δD plot on a distinctively negative slope (Lacelle, 2011).

It should be kept in mind that results of isotopic analysis of ground ice typically cannot give direct answers as to the origin of the ice, because the accumulation is not continuous. Isotopic results should therefore be interpreted together with other evidences to draw a big picture (Williams and Smith, 1989).

2.1.2 Thermokarst Terrain

While the growth of ground ice results in many landforms, degradation of ice-rich permafrost triggers the development of landscapes of irregular topography caused by the compression of the ground following the thawing and the subsequent draining of excess water (Harry, 1986; Van Everdingen, 1998). These are known as thermokarst terrain.

Periods of degradation of permafrost and the resulting formation of thermokarst terrain are described as thermokarst events and they are logged in the permafrost stratigraphy as paleo-thaw unconformities (Harry, 1986). These unconformities represent layers of permafrost that once were non-cryotic, meaning that ground ice or cryostructures were destroyed or amputated (French, 1996). When this formally non-cryotic layer refroze, new cryostructures formed, which means that it is possible to easily identify the paleo-thaw unconformity as a transition between two zones of different cryofacies (i.e., cryostructures and ice contents) (Fig. 2.2) (French, 1996; Harry, 1986). Differences in stable isotope contents, heavy mineral and pollen assemblages are also indicators of transitions between cryofacies. These paleo-thaw unconformities represent a valuable source of evidence for reconstructing past permafrost conditions (French, 1996).

Humans can be the cause of the creation of thermokarst terrain, but natural thermokarst events are the most active process affecting permafrost landscapes (Harry, 1986). Consequences of the formation of thermokarst terrain are multiple. Among those are changes in ecosystem, for example in Alaska where areas of upland forests changed into wetlands (Osterkamp et al., 2000); disturbance of biota, through oversaturation or drying (Callaghan and Jonasson, 1995); creation of depressions that catches snow or water, inducing more warming of the ground and thawing of slopes that can lead to land failures and mass movements; damages on infrastructures underlain by permafrost and consequent reparation issues; a reduced bearing capacity and creep resistance of the ground, which diminishes the strength of the soil itself and induces slope instability (Smith, 1993); and others. Regarding these effects of thermokarst events, one component is critical to the determination of the intensity of the consequences, namely the ground ice content. The amount of ground ice has a crucial influence on subsidence of a thawing or thawed ground, as

grounds with small ice content will be less affected by effects of permafrost thawing because they experience less subsidence (ACIA, 2005).

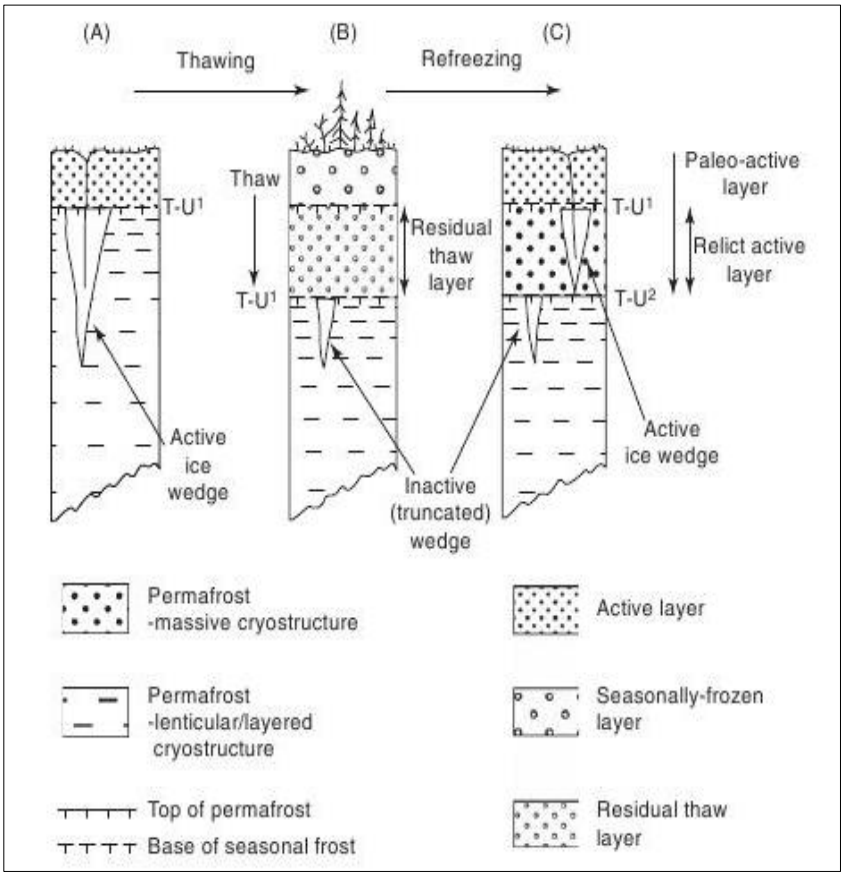

Fig. 2.2 Cryostratigraphic evidence of the thawing and refreezing of permafrost. T-U^1 is the primary thaw unconformity at the top of permafrost (A). When thawing occurs, T-U^1 deepens (B), and when refreezing occurs, it moves back towards the surface, leaving T-U^2, a paleo-thaw unconformity, as evidence of previous thawing (C). (from French, 2007)

2.1.3 Retrogressive thaw slumps

The most dynamic landforms of thermokarst terrain are retrogressive thaw slumps (Burn and Lewkowicz, 1990). These are horseshoe-shaped depressions initiated by ablation of ground ice following ice-rich permafrost exposure, which can be caused by diverse sources of disturbance and erosion (Lacelle et al., 2015; Burn and Lewkowicz, 1990). Lacelle et al. (2010) described these

sources as being either climatic or geomorphic. A majority of thaw slumps are found on lakeshores, coastlines or river banks and are caused by thermal and mechanical coastal erosion (Lewkowicz, 1987; Lantz et Kokelj, 2008; Kokelj, Zajdlik and Thompson, 2009). However, in highlands, coastal erosion cannot justify initiation of thaw slumps. Lacelle et al. (2015) rather identified water tracks forming at diverse location following significant precipitations or mass wasting, and streams undercutting the base of moderately steep hillslopes to be crucial points for formation of thaw slumps, especially following important rainfall events. Other sources of disturbance and erosion are wildfires and warmer summer and annual air temperatures, which have been proven to contribute to active layer deepening and detachment causing initiation of thaw slumps (e.g., Lantz and Kokelj, 2008; Kokelj, Zajdlik and Thompson, 2009; Burn and Lewkowicz, 1990; Lewkowicz and Harris, 2005)

Following the ground ice ablation, sediments drop to the base of the headwall and form an accumulation of fluid mud (Lantz and Kokelj, 2008). Once the creation of a thaw slump is completed, other factors contribute to its growth. A thaw slump remains active as long as summer ablation of ground ice is possible (Lewkowicz, 1987). The rate of headwall retreat is mainly determined by ground ice content (French, 1974), but in order for ground ice to ablate, permafrost must be exposed, net radiation must be sufficient, and summer air temperatures must be warm enough (Lewkowicz, 1986; Lacelle et al., 2015). Other factors such as ground ice content, face orientation, slump geometry, and relief have an influence (Lewkowicz, 1986, 1987). The headwall can be kept from exposure if slumping sediments accumulate at its base. These sediments are transported away from the headwall through their mobilisation in water. Meltwater from ground ice thawing is often not sufficient as it is rapidly drained from the sediment accumulations. However, periods of heavy and continuous precipitations have shown a positive impact on

evacuation of slumped sediments at the base of the headwall, as they make the sediments fluid enough to generate mudflows (Lacelle et al., 2010). Precipitations, by increasing soil moisture, have the potential to reduce the soil strength and trigger large mass flow events (Kokelj et al., 2015). Also, as mentioned above, thaw slumps were proven to develop more often on moderately steep hillslopes, which means that after important rainfall events, the movement of slumped sediment would be even easier (Lacelle et al., 2015). All of these factors allow for the headwall to be exposed to solar radiation and warm air temperatures. Thaw slump will stabilize if the ice-rich headwall is no longer exposed, which often occurs when the rate of accumulation of sediments at the base of the headwall is greater than the rate of evacuation of these sediments which end up insulating the headwall, or if the ice-rich ground supply is exhausted (Burn, 2000; French, 1974).

2.2 Climate changes

The most considerable climate change Earth has known during the last tens of thousands of years is the passage from the cold, dry, windy and sparsely vegetated glacial world of 21 ka ago to the warm, widely vegetated, interglacial world of today (Ruddiman, 2008). About 900 ka ago, Earth's climate started to respond to approximately the 100,000-year eccentricity cycles in terms of oscillations in ice volume. This shift from the previous 41,000-year cycles to the 100,000-year cycles of glacial worlds was probably linked to the slow cooling of the Earth that had been ongoing for millions of years, which gradually reduced ablation in high latitudes enough so that ice would persist through relatively weak insolation maxima. The 100,000-year oscillations of glacial worlds are clearly explained by the summer insolation trends of the last hundreds of thousands of years; the trends follow the 23,000-year precession cycle, with a modulation of the precession signal by eccentricity at a period near 100,000 years (Fig. 2.3). The explanation of these 100,000-year oscillations of glacial worlds is still the subject of many studies, but results define large ice sheets

as producers of internal responses that act as positive feedbacks to the melting or formation of the ice that was first initiated by changes in insolation (Ruddiman, 2008). Processes such as ice-albedo feedback and deepwater formation in the North Atlantic most likely contribute (Serreze and Barry, 2005).

2.2.1 Climate Changes since the Last Glacial Maximum

2.2.1.1 Last Glacial Maximum

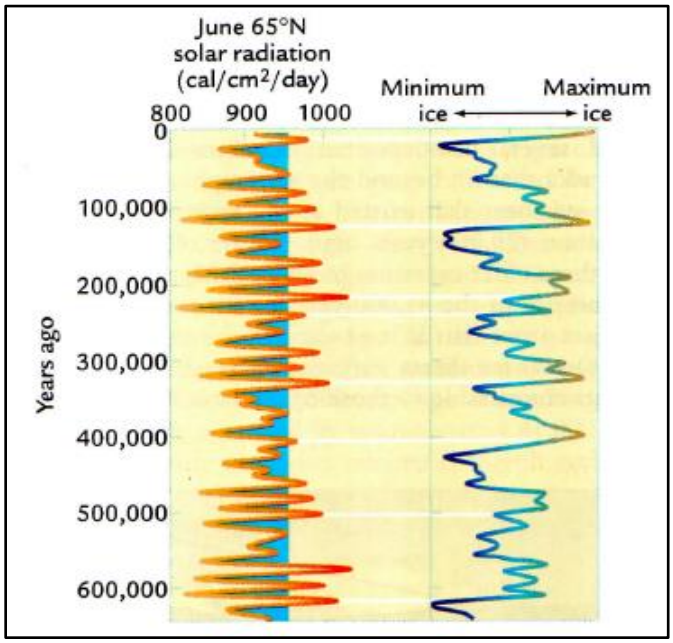

Fig. 2.3 Modulation of summer insolation by eccentricity near 100 000 years. (from Ruddiman, 2008)

The most recent 100,000-year cycle occurred around 21 ka ago. This period is known as the Last Glacial Maximum (LGM), the time at which ice sheets were at their maximum extent, and it lasted from about 25 to 18 ka, depending on the region and interpretation (Serreze and Barry, 2005). CLIMAP, a large interdisciplinary reconstruction of Earth's conditions during a typical northern summer of the LGM, describes a world covered by 35 million km^2 of ice, which corresponds to 25% of the planet's land surface, compared to today's 14.2 million km^2, with a sea

level 110 to 125 m lower than today, joining Asia with Australia and Britain with mainland Europe, and global temperatures almost 4°C colder than today. This reconstruction is still questioned, notably on the aspect of the extent and thickness of the ice sheets and the temperature anomaly. For example, ice sheets in the northern hemisphere are thought by many researchers to have been less extensive than during previous glaciations because of the dryer climate of the LGM that led to a lesser availability of moisture (Ruddiman, 2008). Other studies have also found greater cooling of global temperatures, describing a global mean cooling of 5.8 ± 1.4°C because of the added effects of atmospheric dust content and vegetation (Schneider Von Deimling et al., 2006).

2.2.1.2 Deglaciation

After the Last Glacial Maximum (LGM), Earth has undergone an irregular deglaciation before entering the present warm interglacial period, the Holocene. The deglaciation started approximately between 15 and 13 ka, and ended around 6 ka (Ruddiman, 2008; Serreze and Barry, 2005). Just like for the glaciation, the deglaciation and the Holocene warmth occurred in response to Earth's orbital variations (Kaufman et al., 2004). Around 20 ka ago, Earth's angle of tilt and precessional motion caused the summer insolation to increase, reaching maxima around 10 ka (Ruddiman, 2008). Even though the deglaciation was driven mainly by a gradual increase in summer insolation, combined with increased concentrations in CO_2 and methane in the atmosphere, it was not uniform (Ruddiman, 2008; Serreze and Barry, 2005). That is due to the major role of processes that relate the atmosphere, ocean and ice sheet systems (Serreze and Barry, 2005). Indeed, according to a study made by Menviel et al. (2011) using an Earth system model and paleo-proxy data, the irregularity that characterizes the deglaciation was driven by changes in the strength of deep water formation induced by freshwater input from ice sheets in the North Atlantic (Menviel et al., 2011). Some of the major events that define the variability of the

deglaciation are the Heinrich event 1, a cold interval that lasted from about 17.8 to 15.2 ka (Menviel et al., 2011), the Bølling-Allerød, an abrupt warming event that lasted from about 14.7 to 13 ka, and the Younger Dryas, a sudden cooling episode that lasted from about 13 to 11.7 ka (Serreze and Barry, 2005).

Even though the deglaciation was punctuated by colder intervals that sometimes contributed to a re-advance of the ice sheets (e.g., The Laurentide Ice Sheet during the Younger Dryas) (Serreze and Barry, 2005), they still gradually melted, and, as they disappeared, their influence on climate reduced. The present interglacial period, the Holocene, theoretically started about 11.5 ka ago, at the end of the Younger Dryas. Around 10 ka, orbital factors started to change again, gradually shifting insolation values towards today's. By 10 ka the CO_2 levels had stabilized and by 6 ka the ice sheets had melted to their modern extent (Ruddiman, 2008).

2.2.1.3 Holocene Thermal Maximum

The most important event of the beginning of the Holocene is the Holocene thermal maximum (HTM), a warmer interval that represents the temperature peak of the Holocene (Kaufman et al., 2004). According to a study conducted by Kaufman et al. (2004) on 140 sites across the North American Arctic, the HTM start, end and duration varied widely depending on the location. Generally, it started around 8.9 ± 2.1 ka and ended around 5.9 ± 2.6 ka, starting and ending earlier in the northwest. All of northern America seemed to have warmed and cooled in the same order, which is starting in central and eastern Beringia, followed by Greenland and Iceland, the Canadian Arctic Islands and northern continental Canada (Kaufman et al., 2004).

During the HTM, temperatures across northern Canada increased following a range of 0.5 to 3°C and an average 1.6 ± 0.8°C. For Alaska and northwestern Canada, temperatures increased

approximately in-phase with the summer insolation anomaly, while the rest of northern Canada entered the HTM several thousand years later, due particularly to the presence of the residual Laurentide Ice Sheet (Kaufman et al., 2004).

2.3 Climate changes and permafrost

Permafrost depth is defined by the mean surface temperature and the geothermal heat flux, and the active layer thickness is determined by seasonal and interannual temperature variations. If the mean annual air temperature rises due to a change in climatic conditions, the active layer will thicken. If the climate warming persists, the permafrost table will deepen and the permafrost base will rise as surface warming migrates downwards. Ground conditions could reach a point where permafrost would disappear completely (Smith, 1993).

Heat conduction defines how ground temperatures will react to changes in surface temperatures. It is determined by the thermal properties of the ground, more exactly by the thermal diffusity, that is the ratio of thermal conductivity to volumetric heat capacity. The higher the diffusity of a ground, the faster it will respond to changes in surface conditions. This property varies depending on the type of soil, but most importantly depending on the moisture content of the ground, especially in frozen ground where temperature changes are highly influenced by water phase changes that release latent heat and that can make the ground temperatures stagnate near melting point (Smith, 1993). If increased surface temperatures carry on for a long period of time, the thawing of permafrost at depth can be delayed for as long as decades or centuries (Riseborough, 1990). This means that under warming conditions permafrost with a high ground ice content is especially susceptible to have a smaller rate of degradation in terms of time and extent (Smith, 1993), unless active layer detachment occurs and exposes the permafrost in which case a high

ground ice content augments the rate of growth of thermokarst landforms such as retrogressive thaw slumps (Lewkowicz, 1987; French, 1974).

Permafrost not only is affected by climatic changes, but it also plays a role in the climate system. At depth where seasonal changes have no influence, permafrost represents a good record of climate changes. Also, it transfers air temperature changes to the hydrological and biological systems by, for example, modifying the subsurface water circulation. Moreover, permafrost as an impact on climate as it has the ability to act as a positive feedback to warming through the release of gases like CO_2 and CH_4 (Koven et al., 2011), which links climate changes in the Arctic to the global climate change (Anisimov, Shiklomanov and Nelson, 1997; Fukuda, 1994).

Measurements of ground temperature in Canada, Alaska, and Russia have proven a general warming of permafrost over the last several decades (Couture et al., 2003; Lachenbruch and Marshall, 1986; Nelson, 2003). With increasing air temperatures in regions underlain by permafrost and recent evidence of warming ground temperatures, the study of permafrost is growing in importance, especially within the framework of past and present climatic changes (IPCC, 2013).

Chapter 3: Study Area

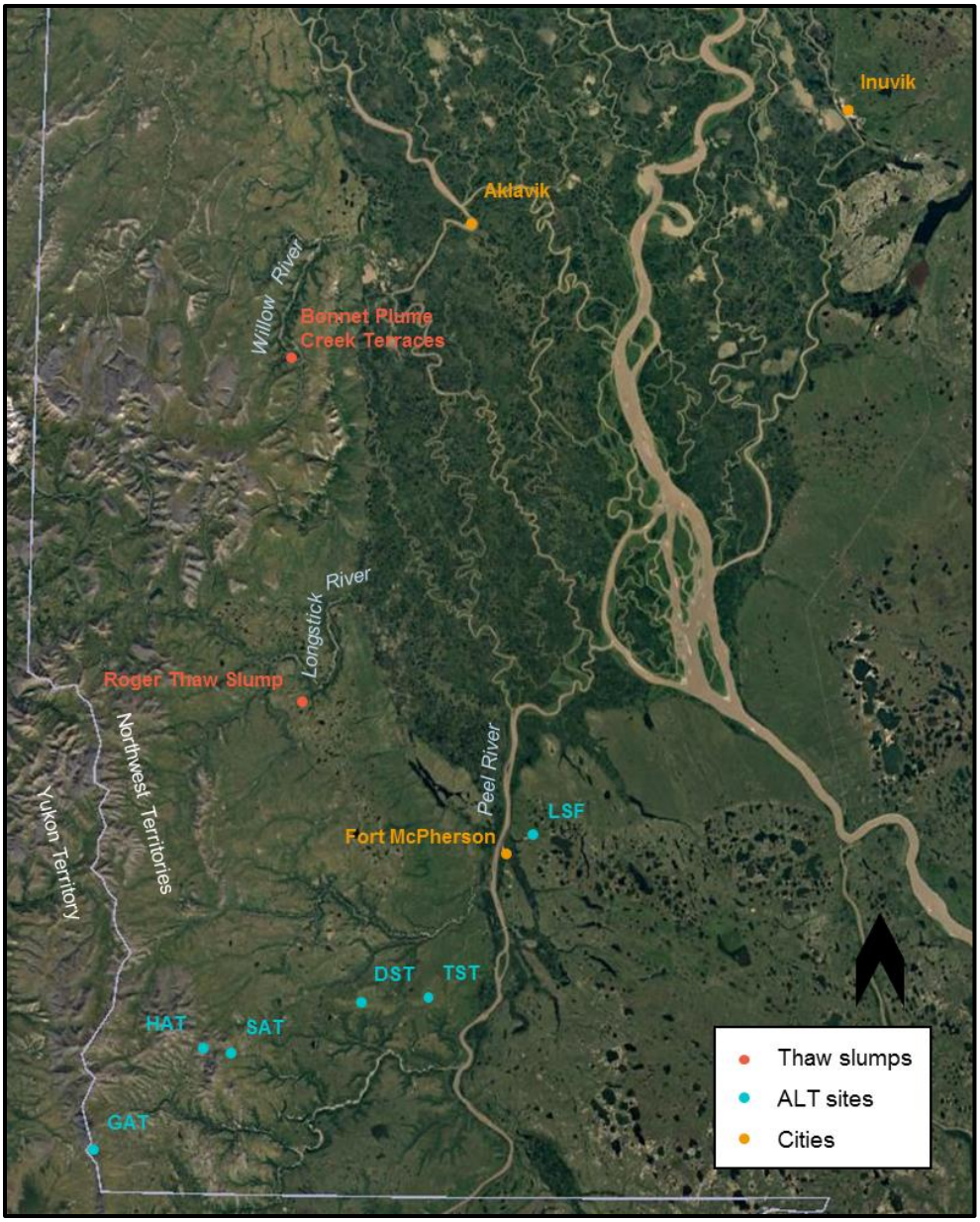

Fig. 3.1 Study area map showing sampling sites and other locations mentioned in this thesis.

3.1 Geology and physiography

The study area is located in the Richardson Mountains-Peel Plateau region, northwestern Canada (Fig. 3.1). The Richardson Mountains stand at the northeast extremity of the North American Cordillera and they consist of a series of north-south orientated smooth ridges separated

by wide valleys (Catto, 1996). The mountains are elevated between 320 and 1575 m a.s.l., although they are generally above 500 m a.s.l.. The ridges of the mountains are formed of resistant quartzites and sandstones, and the valleys are shaped in weathered siltstones and shales (Norris, 1985). The Peel Plateau region is located about halfway of the north-south orientated Richardson Mountains, where a vast plateau extends eastward from the mountains with a gentle slope and elevation varying from 650 to100 m a.s.l., with a relatively even relief of less than 100 m (Catto, 1996).

The north-south trending mountains are the result of the regional tectonic of east-west convergence that caused the uplifting of Paleozoic deep-water clastic sediments along the western paleo-coastline of North America during the latest Cretaceous or early Tertiary (Ecosystem Classification Group, 2010; Lane, 1996; Smith, Meikle and Roots, 2004). The sediments were truncated, folded and overturned, and water, ice and wind sculpted the ridges and valleys (Ecoystem Classification Group, 2010). The southern Richardson Mountains are a fractured anticlinorium with sandstones and limestone of Lower and Middle Cambrian age in the hinges, bordered by more resistant chert and limestone of Ordovician to Middle Devonian age (Smith, Meikle and Roots, 2004). The mountains are still seismically active (Forsyth, Wetmiller and Basham, 1996).

Surficial deposits in the study area are separated in two broad categories: exposed bedrock and thin colluvial deposits in the unglaciated region, and till in the formerly glaciated areas (Duk-Rodkin and Hughes, 1992; Hughes, Hodgson and Pilon, 1972) (Fig. 3.2). The region is incised by a network of rivers and stream valleys that were shaped after the deglaciation, resulting in low relief V-shaped valleys in the highlands, and canyon-like valleys of about 350 m of relief near the Peel river (Lacelle et al., 2015).

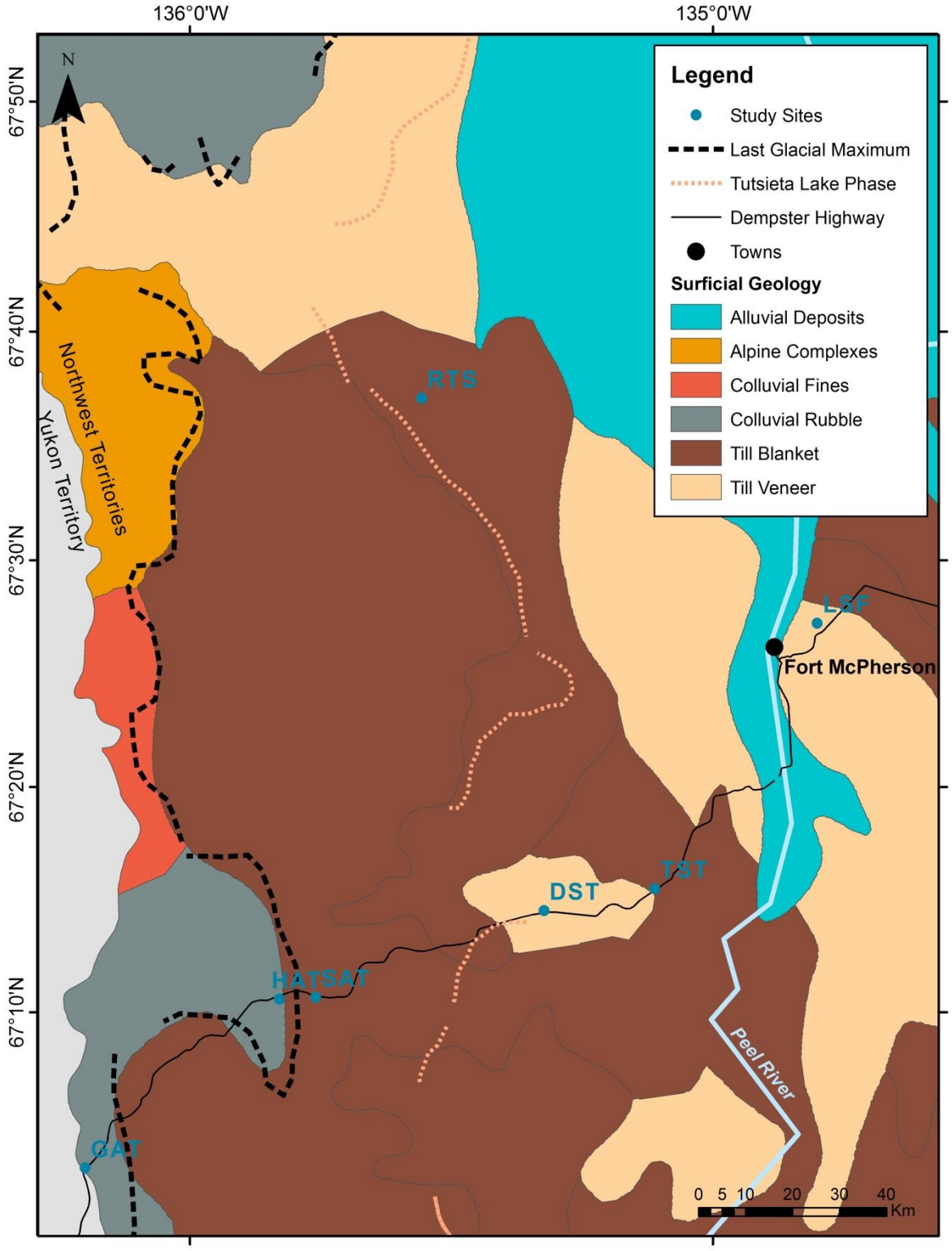

Fig. 3.2 Surficial geology of the study area.

3.2 Vegetation

Vegetation in the Richardson Mountains-Peel Plateau is characterized by alpine and arctic tundra communities consisting of sedges, cottongrasses, low shrubs and a few herbs on higher elevated plateaus; krummholz colonies of spruce on south-facing slopes below 1000 m a.s.l.; open spruce woodlands in lower elevated southern plateaus; tall willow, green alder and dwarf birch shrub thickets in the valley bottoms; and white spruce communities with paper birch and balsam poplar on south-facing slopes and alluvial terraces below 500 m a.s.l. (Ecosystem Classification Group, 2010) (Fig. 3.3).

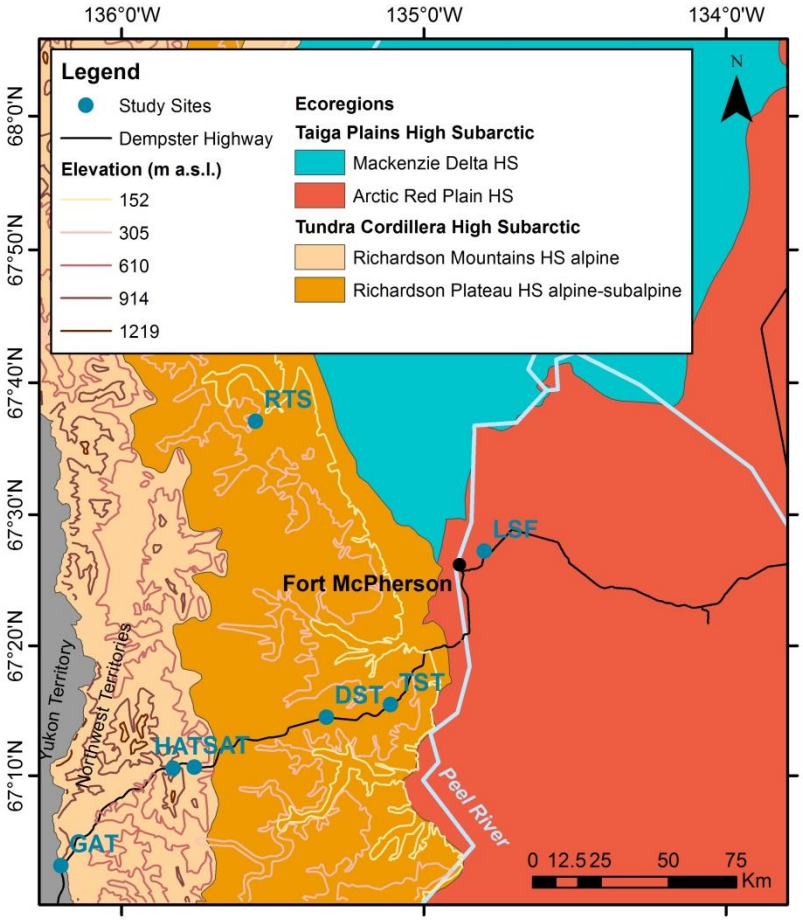

Fig. 3.3 Ecoregions of the study area.

Palynological and fossil evidence from regions surrounding the Richardson Mountains-Peel Plateau area sustain that there were important changes in the vegetation in the region following the deglaciation (Ritchie, Cwynar and Spear, 1983; Dyke, 2005; Ritchie, 1982; Ritchie and Hare, 1971). There was first a transition from tundra to boreal forest, with the tree line migrating northward up to the Tuktoyaktuk Peninsula. Presence of *Picea* on the Peninsula is recorded from about 10 to 6 ka (Ritchie, Cwynar and Spear, 1983). Similar evidence of this transition to boreal forest was found at Lateral Pond, at the south end of the Richardson Mountains, with the spread of dwarf shrubs, increased organic sedimentation, soil humification and paludification following the rapid transition from a warming glacial to a non-glacial climate around 12 ka, and the total pollen influx reaching a maximum around 10.3 ka (Ritchie, 1982). Generally, in northwestern Canada, genera such as *Myrica*, *Typha*, *Populus*, and *Picea* extended their limit northward between 11.6 and 5.6 ka, reaching maxima around 10.3 ka (Cwynar, 1982; Ritchie, Cwynar and Spear, 1983; Ritchie and Hare, 1971). While sites at the Tuktoyaktuk Peninsula have transitioned to a tall shrub tundra with only dispersed *Picea* around 5.6 ka, and reached the present dwarf birch heath tundra around 4 ka (Ritchie and Hare, 1971), evidence from sites at the south end of the Richardson Mountains show that the gradual increase in *Picea* reached its modern extent in the forest profile around 7.5 ka and that only slight changes occurred until 6 ka, as alder and tree birch grew to their modern position in the vegetation (Ritchie, 1982).

3.3 Climate

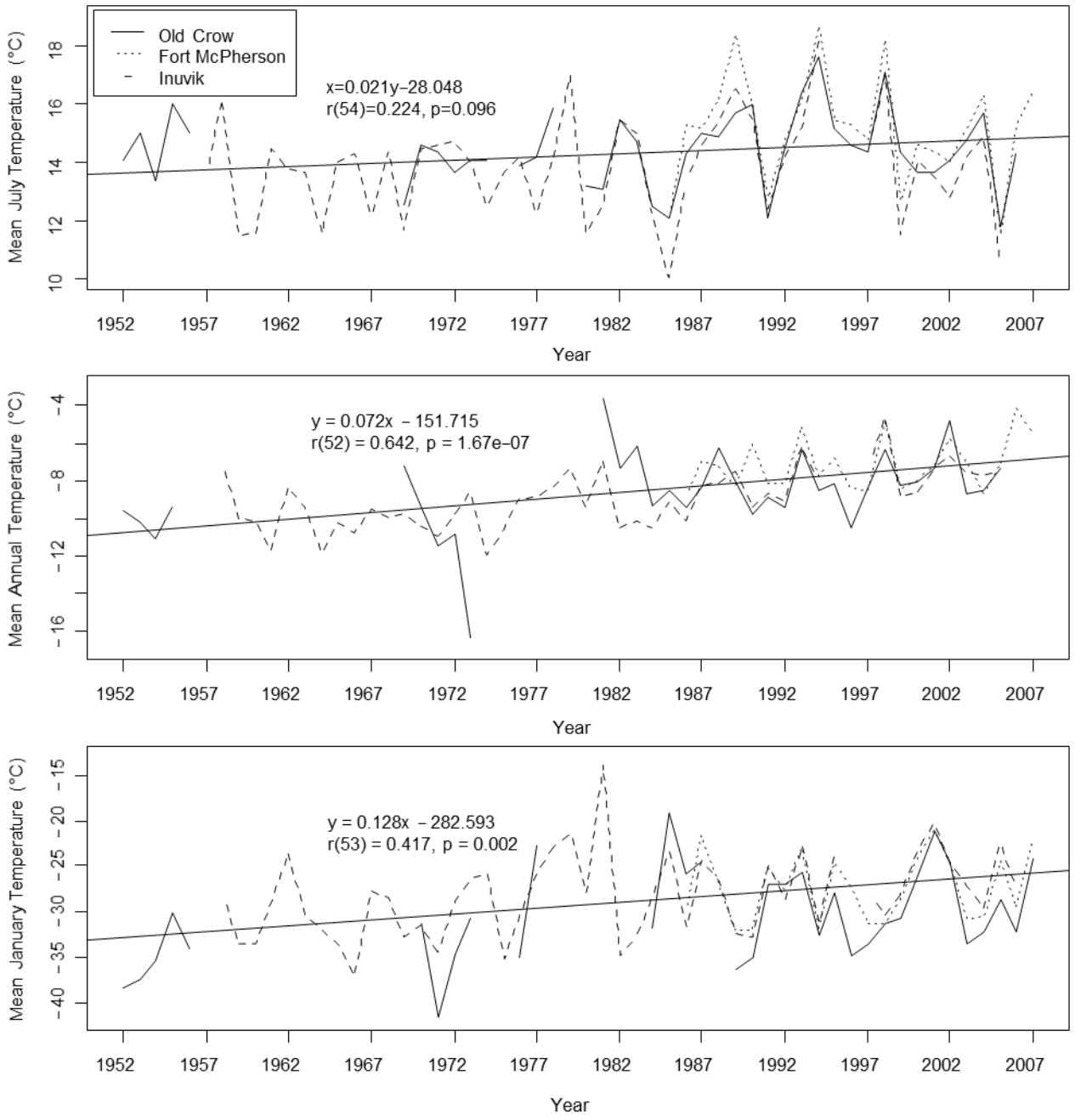

Fig. 3.4 Mean air temperatures in Old Crow, YK (1952-2007), Fort McPherson, NWT (1985-2007) and Inuvik, NWT (1957-2006). Trends based on an average of the three stations. Pearson Product-Moment Correlation Coefficient shown for trends as r(*df*)=*a*, p=*b*, where *df* is the degree of freedom, *a* is the correlation coefficient and *b* is the p-value.

The regional contemporary climate is characterized by short cool summers and long cold winters. Mean July temperature at the closest meteorological station, namely Fort McPherson, NWT, is 15.2°C (1985-2007), and mean January temperature is −27.5°C (1986-2007). The mean annual air temperature is −7.3 ± 1.8°C (1986-2007). Average total annual precipitation at Fort McPherson is 297.7 mm (1981-2007), with a little more than half of it being snowfall (Environment Canada, 2015). Based on three meteorological stations surrounding the study area, that is in Fort McPherson, NWT, Inuvik, NWT, and Old Crow, YK, recent mean annual air temperatures have experienced a slight increase, especially since the end of the 1970s. While mean July temperatures remained fairly stable, but with greater interannual variations since the end of the 1970s, mean January temperatures have had a more pronounced increase since the mid-1970s (Fig. 3.4) (Environment Canada, 2015). Total annual precipitations have also experienced an increase, especially since the end of the 1980s (Fig. 3.5).

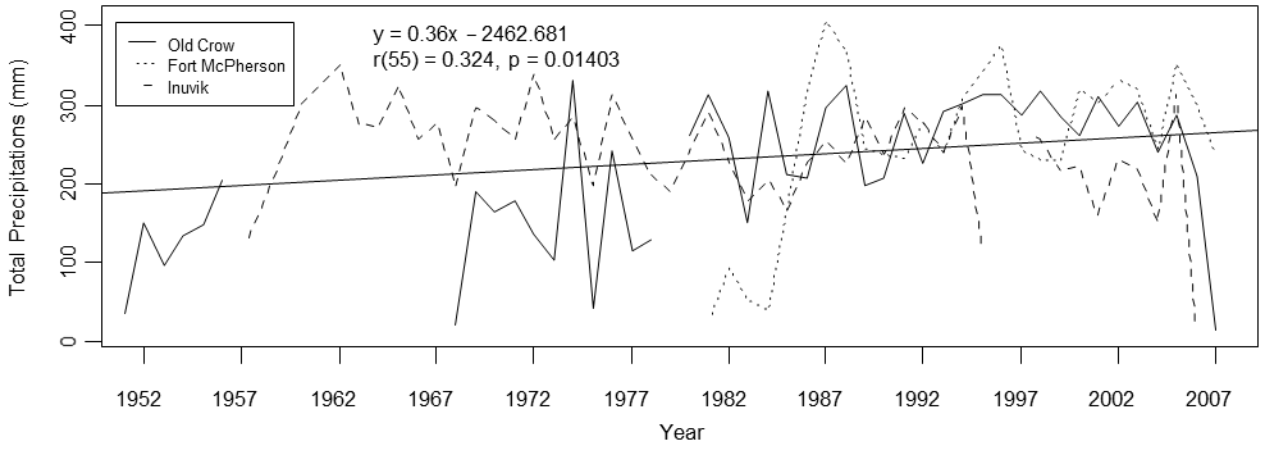

Fig. 3.5 Total annual precipitation in Old Crow, YK (1952-2007), Fort McPherson, NWT (1985-2007) and Inuvik, NWT (1957-2006). Trends based on an average of the three stations. Pearson Product-Moment Correlation Coefficient shown for trends as r(*df*)=*a*, p=*b*, where *df* is the degree of freedom, *a* is the correlation coefficient and *b* is the p-value.

3.4 Glaciation

The Richardson Mountains represent the western limit of the extent of the Laurentide Ice Sheet (Duk-Rodkin and Hughes, 1992) and their eastern slope was covered by ice during the Last Glacial Maximum (Lacelle et al., 2013) up to about 750 m a.s.l. (Duk-Rodkin and Hughes, 1992). The region was the subject of two re-advances of the Laurentide Ice Sheet, that is the Tutsieta Lake Phase around 15 ka cal yr BP, and an unnamed phase a few kilometers east of the Tutsieta Lake Phase (Duk-Rodkin and Hughes, 1992). It has been ice-free since approximately 13 ka cal yr BP as suggested by the presence of *Bison priscus* near the community of Tsigetchiic (Zazula et al., 2009). The basal condition of the Laurentide Ice Sheet is inferred to have been warm-based, as evidenced from its reconstructed thickness, presence of eskers in the region and carbonates found in buried aufeis ice beneath till (Beget, 1987; Lacelle et al., 2013). Permafrost aggraded in the glacial sediments during the late Pleistocene, prior to the onset of the early Holocene warm interval, as supported by modeled three-dimensional bed thermal field and related permafrost conditions (Tarasov and Peltier, 2007).

3.5 Permafrost

The climate and vegetation conditions of the Richardson Mountains-Peel Plateau region ensure that permafrost is continuous, thick (ca. 100-300 m) and relatively warm (mean annual ground temperatures > –2.5°C). Measurements made by Lacelle et al., 2004 and Malone et al., 2013 indicate that uppermost 10 m of permafrost is ice-rich (ice content ranging from 50 vol.% to tabular bodies of massive ice) (Lacelle et al., 2015). Similarly, analysis of qualitative data from 121 seismic shothole drillers' log records (Smith and Lesk-Winfield, 2012) indicate that massive ice is present in more than 50% of the case in the 6 meters below ground surface. This is consistent with the region's surficial geology, which is characterized by moraine plains less than 6 m thick,

and broad hummocky rolling moraines up to 20 m thick (Duk-Rodkin and Hughes, 1992; Hughes, Hodgson and Pilon, 1972), as hummocks are typically found in areas of continuous permafrost with high ice content (van Everdingen, 1988).

The modern active layer fluctuates in terms of thickness across the region and its surroundings. Data varies from 50-90 cm near Mayo in central Yukon (Burn, Michel and Smith, 1986), to 25-90 cm at Crumbling Point in the Tuktoyaktuk Coastlands, NWT (Murton, Whiteman and Allen, 1995), to 40-60 cm on Pelly and Gary Islands, near Illisarvik, and at Todd Lake also in the Tuktoyaktuk Coastlands (Burn, 1997). At Inuvik, in hummocky terrain beneath an open canopy forest, active layer thickness is about 1 m, which is 2 times the thickness of the active layer at the coast (Burn, 1997; Mackay, 1995). Moreover, in mountainous regions, such as in the Richardson Mountains, south and west facing slopes may have a thicker active layer because of the higher amount of insolation they receive (Lacelle et al., 2015).

3.6 Climate history and permafrost conditions

In northwestern Canada, summer temperatures began to be warmer than today's around 10.6 ka and the transition to near-present temperatures occurred between 6.7 and 5.6 ka (Kaufman et al., 2004). Kaufman et al. (2004) gathered evidence of this warmer climate, notably on the Tuktoyaktuk Peninsula, central Yukon and the coastal plain of northwestern Canada, suggesting a general warming of temperatures between approximately 12.2 and 5.6 ka, with a peak around 10.3 ka (Kaufman et al., 2004). However, a subsequent review of diverse proxy records indicates that temperature and moisture values in the region were spatially variable during the early Holocene and that the temperature maximum could have been reached between 7 and 5 ka, suggesting a mid-Holocene thermal maximum (Kaufman et al., 2016).

Studies conducted in northwestern Canada indicate varying results in terms of temperature anomaly for the Holocene thermal maximum (HTM). On the Tuktoyaktuk Peninsula, on the northwest coast of the Northwest Territories, proof of the northward shift of the tree line during the HTM was interpreted as a mean annual air temperature (MAAT) 3°C higher than today (Ritchie, 1984). Other evidence based on shelled invertebrates from the Richardson Mountains and the Mackenzie Delta in the Northwest Territories indicate that the MAAT was from 8.2 to 11.6°C higher than today, with a peak around 10.5 ka (Delorme et al., 1977). Palynological and megafossil record from the Tuktoyaktuk Peninsula imply mean daily temperatures for the warmest months (June, July, and August) about 5°C higher than today, accompanied by a growing season about 30 days longer (Ritchie and Hare, 1971). Similarly, evidence from endrostromatolites from permafrost karst in central Yukon reflects summer air temperatures 7 ± 2 °C higher than today (Clark et al., 2004).

Based on this variety of evidence of the early Holocene thermal maximum from northwestern Canada, it is possible to assume that mean summer air temperatures were between 2.5 and 11.6°C higher than today in the region (Clark et al., 2004; Delorme et al., 1977; Ritchie and Hare, 1971).

During this early Holocene warm interval, permafrost has known important changes. The active layer thickness was on average 2 to 3 times greater than today, with sites reaching up to 8 times the modern thickness. The paleo-active layer in the Tuktoyaktuk Coastlands was estimated as being 2.5 times as deep as the modern active layer based on botanical and cryostratigraphic evidence (Burn, 1997). Similarly, ice-rich glaciolacustrine sediments near Mayo, central Yukon Territory, showed an early Holocene active layer that was approximated as having a thickness of 132 cm. Compared to today's active layer, it represents on average 2 times the modern thickness

(Burn, Michel and Smith, 1986). Other evidence from the Herschel Island, northern Yukon Territory, revealed a paleo-active layer as much as 150 to 300 cm thick, representing about 5 to 7 times the modern thickness (Fritz et al., 2012). Moreover, sedimentary structures observed on the Tuktoyaktuk Coastlands reflected a paleo-active layer as much as 8 times thicker than today (Murton, 2001). The active layer deepening during the HTM is not only linked to summer temperatures being higher than today (Fritz et al., 2012), but it is also largely due to the presence of forest, snow trapping, and increasing ground temperatures in winter (Burn, 1997). This warmer climate induced active layer deepening also led to a larger rate of thermokarst activity (Rampton, 1982). As temperatures reached near-modern values, permafrost aggregated and a paleo-thaw unconformity marking the extent of a relict thaw layer was left as proof of this Holocene warm interval (e.g., Burn, 1997; Burn, Michel and Smith, 1986; Fritz et al., 2016; Kokelj, Smith and Burn, 2002; Malone et al., 2013; Murton, 2001; Murton and French, 1994; Worsley, 2000;)

Global circulation models project an increase of 0.3 to 4.8 °C in global air temperature over the 21st century, depending on the model (IPCC, 2013), and an increase of 3 to 6 °C for the Arctic by 2080 (Callaghan et al., 2011). Recent projections of the magnitude of permafrost degradation vary greatly depending on the forcing mechanisms and physics of the climate models, but considerable degradation and active layer thickening is expected over much of the areas underlain by permafrost (Collins et al., 2013). Regional models project that the upper 2 to 3 meters of 16% to 20% of permafrost in Canada will thaw by the end of the 21st century, and that widespread permafrost degradation will occur over about 57% of Alaska (Callaghan et al., 2011). Currently, numerical models of permafrost degradation are accused of not effectively considering permafrost distribution and parameters, such as surface cover, ground ice content, presence of excess ice, and

vegetation changes, which in turn have an impact on the frequency of wild fires (Callaghan et al., 2011; Froese et al., 2008).

As mentioned before, initiation of retrogressive thaw slumps is caused by heavy rainstorms, wildfires and increased air temperatures, which all lead to active layer deepening and detachment (Burn and Lewkowicz, 1990; Kokelj, Zajdlik and Thompson, 2009; Lacelle et al., 2015; Lantz and Kokelj, 2008; Lewkowicz and Harris, 2005), and their growth is maintained by solar radiation and warmer air temperatures, as long as ice-rich permafrost is exposed, which remains true when enough meltwater is available or if heavy rainfalls occur (Lacelle et al., 2015; Lacelle, Bjornson and Lauriol, 2010; Lewkowicz, 1986). Therefore, as the recent climate warming continues, retrogressive thaw slump activity will most likely rise, especially in hilly ice-rich terrain, and their impact on permafrost landscapes will intensify the already felt impacts of this warming on soil and water ecosystems (Lantz and Kokelj, 2008).

Chapter 4: Methodologies

4.1 Determination of Thickness of Thaw Layer

In July 2016, the thaw layer thickness (TLT) was determined at six sites along the Dempster Highway between Fort McPherson (NWT) and the frontier between the Yukon Territory and the Northwest Territories (Fig. 3.1). This layer is characterized as a thaw layer, because the measurements were not done during the period of maximum thaw, in which case it would have been referred to the as the active layer. The method used is based on the frost probing procedure described in the International Permafrost Association (IPA) Working Group on Periglacial Processes and Environments' Handbook on Periglacial Field Methods (Nelson and Hinkel, 2004). A metal rod was pushed in the ground at each intersection of a 11 × 11 m grid separated into 121 squares of 1 m^2. The thickness of the thaw layer was considered reached when resistance made it impossible to continue probing and depth of penetration was measured. Two measurements were made at each intersection and the average of the two was taken. Sediment samples were also taken at each site, every five centimeters when horizons were visible, and only one when the ground was cryoturbated. The choice of the sites was determined by an elevation gradient, which also has an effect on the vegetation cover; each site was located at approximately 1000, 800, 600, 500, 425 and 30 m of elevations, with vegetation changing from grassy alpine tundra (GAT), to hummocky alpine tundra (HAT), to sub-alpine tundra (SAT), to dwarf shrub tundra (DST), to tall shrub tundra (TST), and to lowland spruce forest (LSF).

4.2 Sampling of Thaw Layer and Permafrost at Thaw Slump

A hole was dug above the headwall of Roger Thaw Slump until the permafrost table was reached at 60 cm below surface. The thaw layer was sampled in 5 cm sections using a knife, the

first 15 cm being litter and humus (Fig. 4.1). Pieces of wood of around 1 cm of diameter and 5 cm long were found at the bottom of the thaw layer, between 50 and 55 cm below surface. A permafrost core was collected using a Cold Region Research Engineering Laboratory (CRREL) corer. Coring was made to a depth of 105 cm below surface. The core was also subdivided in 5 cm sections. All samples were put in sealed plastic bags for transportation to the University of Ottawa (ON, Canada).

Fig. 4.1 Photograph of the thaw layer at Roger Thaw Slump, NWT, on August 1st, 2016 (RTS; 67°37'05.2"N, 135°33'23.2"W, 350 m a.s.l.).

Samples of massive ice and permafrost were also collected from different units exposed in the headwall using a trowel and ice pick. These were also placed in sealed plastic bags and left to thaw before being transported. The headwall samples were divided in five units in the field based on visible cryostratigraphy (Fig. 4.2). Unit 1 is a horizontal body of massive ice starting 250 cm below surface extending to the floor of the slump. West of the body of massive ice is Unit 2; a zone of vertically banded ice and sediments. Unit 3 is a body of bluish ice situated between Units 1 and 4. Unit 4 is a massive milky white ice body rich in air bubbles located east of Unit 3 in the middle of the thaw slump. All of these units are overlain by a mixture of fine sands and sections of buried organics, identified as a relict thaw layer (RTL). Sediments and buried organic debris were sampled and are referred to as RTL samples.

Fig. 4.2 Photograph of the headwall at Roger Thaw Slump, NWT, on August 1st 2016, showing the four massive ice units, and the limit of the relict thaw layer (RTL) (RTS; 67°37'05.2"N, 135°33'23.2"W, 350 m a.s.l.).

4.3 Ground Ice Analyses

4.3.1 Samples Preparation

Once in Ottawa, all samples were stored in a refrigerator kept at 4°C until preparation and analyses. Meltwater from massive ice samples and from excess ice of permafrost and thaw layer samples were filtered through a 0.45 µm filter and placed in the appropriate vials for analysis.

4.3.2 Major Ions

Melted ground ice samples were analyzed for major cations (Ca^{2+}, Mg^{2+}, Na^{+}, K^{+}, Fe^{+}) and anions (Cl^{-}, SO_4^{2-}, NO^{3-}) at the Geochemistry Laboratory of the University of Ottawa. The approach of this study for determining major ions concentrations is comparable to that of studies analyzing the geochemistry of groundwater in the active layer or non-permafrost soils, as it uses melt-water from thawed ice-bearing permafrost and massive ice samples to measure the concentration of solute per liter of solution (mg L^{-1}) (Lacelle et al., 2014).

For major cations analysis, the samples were first acidified with ultra-pure HNO_3 acid to pH 2. The measurement of the concentrations of major cations was done using a Varian Vista-Pro Inductively Coupled Plasma Atomic Emission Spectrometer (ICP-AES). The measurement of the concentrations of major anions was done by ion chromatography using a Dionex-100. All of the analyzed samples had two duplicates and internal standards were added to the analysis. The analytical reproducibility of the analyses is ±5%.

4.3.3 Stable Isotopes

Filtered melted ground ice samples were analyzed for stable water isotopes ($\delta^{18}O$ and $\delta^{2}H$, or δD) using a Los Gatos Research (LGR) Triple Isotope Water Analyzer (TIWA-45-EP). The analyzer uses Off-Axis Integrated Cavity Output Spectroscopy (OA-ICOS) laser absorption technology to simultaneously and directly measure $^{18}O/^{16}O$, $^{17}O/^{16}O$ and $^{2}H/H$ ratios in liquid water samples (Berman et al., 2013). One ml of water sample along with ten duplicates were analyzed in the laser analyzer through a CTC LC-PAL autoinjector. Seven measurements were taken and the mean of the four last measurements was retrieved to obtain one high-throughput result (Berman et al., 2013). The analyzer contains a Spectral Contamination Identifier (SCI) software that

determines and corrects for the presence of organic contaminants, which confirmed that the samples were free of contaminants. The results were calibrated to three water standards that were previously calibrated relative to Vienna Standard Mean Ocean Water (VSMOW) (Lis, Wassenaar and Hendry, 2008; Berman et al., 2013). The results are expressed in the δ-notation referenced to VSMOW. The precisions of the $\delta^{18}O$ and δD analysis are ±0.3‰ and ±1‰, respectively.

The relation between $\delta^{18}O$ and δD was plotted against the global and local meteoric water lines. Globally, it plots along a regression slope of 8, which defines the global meteoric water line (GMWL; $\delta D = 8\ \delta^{18}O + 10$; Craig, 1961). However, since precipitations' isotopic composition vary based on air temperature, proximity to moisture sources and trajectories of weather systems over land masses, the regression slope values of the meteoric water line also vary regionally (Lacelle, 2011). That defines different local meteoric water lines (LMWL). In the case of this study, Inuvik's LMWL was used ($\delta D = 7.3\ \delta^{18}O - 3.37$; Lacelle, 2011).

Finally, Deuterium excess was determined since the relation between D-Excess and δD can be a good indicator of ice origin (Lacelle, 2011).:

$$\text{D-Excess} = \delta D - 8\ \delta^{18}O\ (\text{Dansgaard}, 1964) \qquad (4.1)$$

4.3.4 Radiocarbon dating of Dissolved Organic Carbon

The concentration of dissolved organic carbon (DOC) in the melted ground ice samples was first determined to measure the volume of water required for $^{14}C_{DOC}$ analyses. The DOC content was analyzed at the G.G. Hatch Stable Isotope Laboratory at the Advanced Research Complex (ARC) of the University of Ottawa. Dissolved organic carbon extraction was done by wet chemical oxidation based on Zhou et al. (2015) and Lang et al. (2016). The potential presence of dissolved inorganic carbon was first purged from the samples as CO_2 by acidification (85%

H_3PO_4). The acidified samples were heated to 60°C for an hour, sparged with helium and the inorganic CO_2 was eliminated from the samples to the atmosphere (Lang et al., 2016). The DIC purged samples were oxidized with sodium persulfate and a catalyst. The samples were then heated to 98°C for an hour, cooled to room temperature, sparged with helium, purified in a vacuum line to convert DOC to pure CO_2, which was then trapped in a breakseal containing a few grains of silver cobaltous that were previously baked at 500°C for two hours, and baked overnight at 200°C to remove sulphur (Palstra and Meijer, 2014). The organic CO_2 samples then passed through a non-destructive infrared (NDIR) detector which measured the CO_2 concentrations (ppm) that are proportional to the DOC content of the samples (St-Jean, 2003). ^{13}C stable isotope analysis was also done in an automated continuous-flow isotope ratio mass spectrometer (CF-IRMS) system (St-Jean, 2003).

DOC concentrations and collected volume of water were sufficient in massive ice samples of units 1, 3 and 4 to permit radiocarbon dating ($^{14}C_{DOC}$). The wet chemical oxidation method was applied to larger water samples of these sites (approx. 250 ml). The resulting DOC CO_2 samples underwent graphitization where they were converted to elemental carbon in the presence of iron and hydrogen on a semi-automated graphitization line designed and built at the A.E. Lalonde AMS Laboratory (ARC, University of Ottawa) (St-Jean et al., 2016; Crann et al., 2016). The graphitized samples were pressed into targets that were loaded in the 3MV tandem accelerator mass spectrometer (High Voltage Engineering) at the A.E. Lalonde AMS Laboratory for determination of ^{12}C and ^{14}C. The fraction modern carbon ($F^{14}C$) is calculated as the ratio of the sample $^{14}C/^{12}C$ ratio to the Ox-II standard 14C/12C ratio, and the 14C ages are calculated as −8033ln(F14C) and reported in 14C and then corrected to cal yr BP (BP = AD 1950) using OxCal v4.2.4 (Bronk

Ramsey, 2009) and the IntCal13 calibration curve (Reimer et al., 2013). For more details on the procedures and protocols of the A.E. Lalonde AMS Laboratory, see Crann et al. (2016).

4.4 Thaw layer and Permafrost Soil Analyses

4.4.1 Particle Size Analysis

Particle size distribution of thaw layer and permafrost soil samples was done using a laser diffraction analyzer (Microtrac S3500). Soil sample preparation consisted of two series of three hydrogen peroxide (H_2O_2) solution attacks spread over 8 days to remove organic matter, a method derived from a procedure proposed by van Reeuwijk, 2002. Two cm^3 sub-samples of soils were transferred into 50 ml centrifuge tubes. First series of attack consisted of adding 5 ml of 30% H_2O_2 to the samples on days 1, 4 and 8. Second series of attack also consisted of adding 5 ml of 30% H_2O_2, but this time the tubes were placed in a hot water bath consisting of 500 ml beaker filled with water and placed on a hot plate. Samples that reacted violently during the first series were transferred in 250 ml beaker and placed directly on the hot plate for the attack. Attacks were considered complete after a reaction had happened or after one hour without any reaction. Samples that were transferred into beakers were rinsed back into their centrifuge tubes with deionised water. All tubes were filled with deionised water, put in the centrifuge (2700 rpm for 7 minutes), and the supernatant water was discarded. The tubes were then filled with a 3% sodium hexametaphosphate solution ($(NaPO_3)_6$) which acts as a dispersing agent, mixed on a vortex mixer for two minutes, and put in the refrigerator for three days before being loaded into the particle sizer analyzer. A sand standard was analyzed before every set of analyses (3) to assure the good functioning of the Microtrac analyzer. Out of the 37 samples analyzed, 14 were duplicated and their mean particle size determined an error of ±2.5% (0.02 µm).

4.4.2 Water Content and Organic Carbon Content

Gravimetric Water Content (GWC) was determined for all samples according to the equation (van Everdingen, 1998):

$$\text{GWC (\%)} = \frac{\text{Mass of water (g)}}{\text{Mass of dry soil (g)}} \times 100 \quad (4.2)$$

Permafrost samples which had been kept in sealed plastic bags in a refrigerator at 4°C were weighted to obtain the mass of moist soil. Some samples had excess water which was extracted and filtered through a 0.45 µm filter and put in the appropriate vials for ground ice analyses outlined above. The samples were then dried in a furnace at 105°C for 24 hours and weighted again to obtain the mass of dry soils. The difference between mass of dry soil and mass of moist soil and excess water represents the mass of water contained in the soil samples.

Organic carbon content was determined through loss on ignition (LOI) using a Leco thermos-gravimetric analyzer (TGA701). This LOI procedure is described as successive heatings of the samples to specific temperatures. Organic matter is combusted to ash and carbon dioxide at a temperature of 550°C (Heiri et al., 2001). The organic matter content is then determined according to the following equation:

$$\text{Organic matter (\%)} = \frac{\text{LOI}_{105}(\text{g}) - \text{LOI}_{550}(\text{g})}{\text{LOI}_{105}(\text{g})} \times 100 \quad (4.3)$$

where LOI_{150} represents the weight of the sample after being dried in the furnace at 105°C and LOI_{550} is the weight of the sample after combustion to 550°C. The weight loss between 105°C and 550°C is proportional to the amount of organic matter in the sample (Heiri, Lotter and Lemcke, 2001). To obtain the organic carbon content from the organic matter content, a conversion factor of 2 was used (Pribyl, 2010). Out of the 43 samples analyzed, 11 were duplicated and determined

an error of ±18.8% (0.19 g). A Calcium Oxalate Standard is analyzed with every set of analyses and defines an analytical accuracy of ±2% (0.02 g).

4.4.3 Radiocarbon Dating of Organics

Organic debris extracted from the RTL was observed under a microscope and fragments of wood and leaves were extracted, along with a sample of bulk fragments of between 0.5 and 1 mm. These organic samples, along with the wood pieces found at the bottom of the thaw layer, were radiocarbon dated at the A.E. Lalonde AMS Laboratory (ARC, University of Ottawa). There, they underwent pre-treatments. The leaves fragment sample was given an AAA (standard acid-alkali-acid) pre-treatment. Following the protocol described by Brock et al. (2010), the samples undergo a first acid wash (HCl, 1N, 80°C, 30 mins) to remove carbonates. They are then rinsed in an alkali solution (NaOH, 0.2N, 80°C, 30 mins) to remove humics. Finally, they undergo a second acid wash (HCl, 1N, 80°C, 30 mins) to remove any CO_2 absorbed during the alkali step. The samples are rinsed in Milli-Q water after each step. The wood and bulk samples were given an A pre-treatment, because they were smaller and more fragile samples, so they were only subjected to the first acid treatment of the AAA protocol, before being freeze-dried overnight (Crann et al., 2016). These pretreated, freeze-dried samples are combusted in a Thermo Flash 1112 elemental analyzer (EA) and the resulting CO_2 is trapped in breakseals. The samples then undergo graphitization and AMS measurement, as described in Section 4.3.4.

Chapter 5: Results

5.1 Stratigraphy

Roger Thaw Slump (RTS) consists of a 70 m wide and ca. 5 to 6 m high headwall that exposes a thaw layer, a relict thaw layer and massive ice (Fig. 5.1).

(RTS; 67°37'05.2"N, 135°33'23.2"W, 350 m a.s.l.). **A.** Overview of the headwall showing the paleo-thaw unconformity delimiting the relict thaw layer (RTL) and the four massive ice units sampling sites. **B.** Close up on the eastern part of the headwall showing the extent of Unit 4, the relict thaw layer (RTL) and the thaw layer (TL) **C.** Unit 4 overlain by the relict thaw layer (RTL) and thaw layer (TL) **D.** Unit 1, 2 and 3 overlain by the relict thaw layer (RTL).

5.1.1 Thaw Layer

Based on the core taken on top of RTS and on observations of the headwall, the thaw layer has a thickness of ca. 60 cm. That is consistent with the other measurements of thaw layer thickness taken along the Richardson Mountains-Peel Plateau elevation gradient, which vary from 63.71 to 43.71 cm below surface (Fig. 5.2). The thaw layer is shallower in the lowland spruce forest (LSF) at 31 m a.s.l. (μ=43.71) and in the tall shrub tundra (TST) at 425 m a.s.l. (μ=47.01), and deeper in the sub-alpine (SAT), hummocky alpine (HAT), and grassy alpine (GAT) tundra at 611, 790, and 957 a.s.l. (μ=57.08, μ=57.79, μ=58.83, respectively). There is a discontinuity in relation between the thaw layer thickness and the elevation gradient in the dwarf shrub tundra (DST) site at 493 m a.s.l., where the thaw layer is the deepest (μ=63.71).

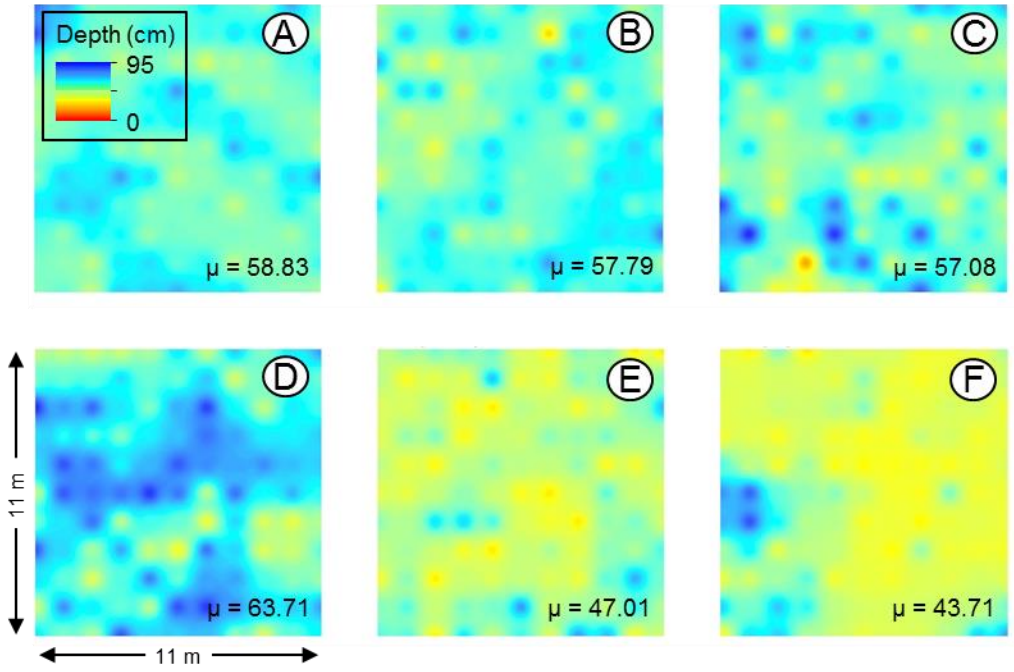

Fig. 5.2 Depth model showing thaw layer thickness from surface in different vegetation types on an elevation gradient in the Richardson Mountains-Peel Plateau region. Mean depth is shown as μ = x. **A.** Grassy Alpine Tundra (GAT; 957 m a.s.l.) **B.** Hummocky Alpine Tundra (HAT; 790 m a.s.l.) **C.** Sub-alpine Tundra (SAT; 611 m a.s.l.) **D.** Dwarf Shrub Tundra (DST; 493 m a.s.l.) **E.** Tall Shrub Tundra (TST; 425 m a.s.l.) **F.** Lowland Spruce Forest (LSF; 31 m a.s.l.).

5.1.2 Relict Thaw Layer

The relict thaw layer (RTL) at RTS extends from the base of the thaw layer at 60 cm to ca. 250 cm below surface. It is identified through the presence of a sharp discontinuity above the massive ice units. Beyond this discontinuity lie sediments of lighter color (compared to the thaw layer) containing buried organic sections (Fig. 5.1B).

5.1.3 Massive Ice

The exposed massive ice is separated into four units based on appearance. Unit 1 is a 1 m wide body of massive ice poor in 1 × 2 mm elongated air bubbles (Fig. 5.1D). Unit 2 is a 1 m wide zone of vertically banded ice and sediments west of Unit 1 body of massive ice (Fig. 5.1D). The ice is poor in air bubbles and the sediments are fine with aggregates of 2 to 10 mm. Unit 3 is a 2 m wide body of bluish ice that is poor to average in elongated air bubbles situated between Units 1 and 4 (Fig. 5.1D). Unit 4 is a 10 m wide zone of white ice, rich in round air bubbles of 1 to 3 mm of diameter located east of Unit 3 in the middle of the thaw slump (Fig. 5.1B-C). Units 1, 3, and 4 extend from below the relict thaw layer down to the floor of the slump.

5.2 Sedimentology

5.2.1 Thaw Layer

Fig. 5.3 presents the results of gravimetric water content, grain size and organic carbon analysis for sediment samples taken at RTS. The thaw layer (TL) consists of 10 cm of litter and hummus and 45 cm of sediments, which is overlain by about 5 cm of tundra vegetation (Fig. 4.1). The litter and hummus horizon, along with the underlying 5 cm of sediments have the largest gravimetric water content (GWC), with values ranging from 640 to 1200%. The values for the rest of the TL are lower but still show a high water content, with all values ranging from 45.5 to 59.6%

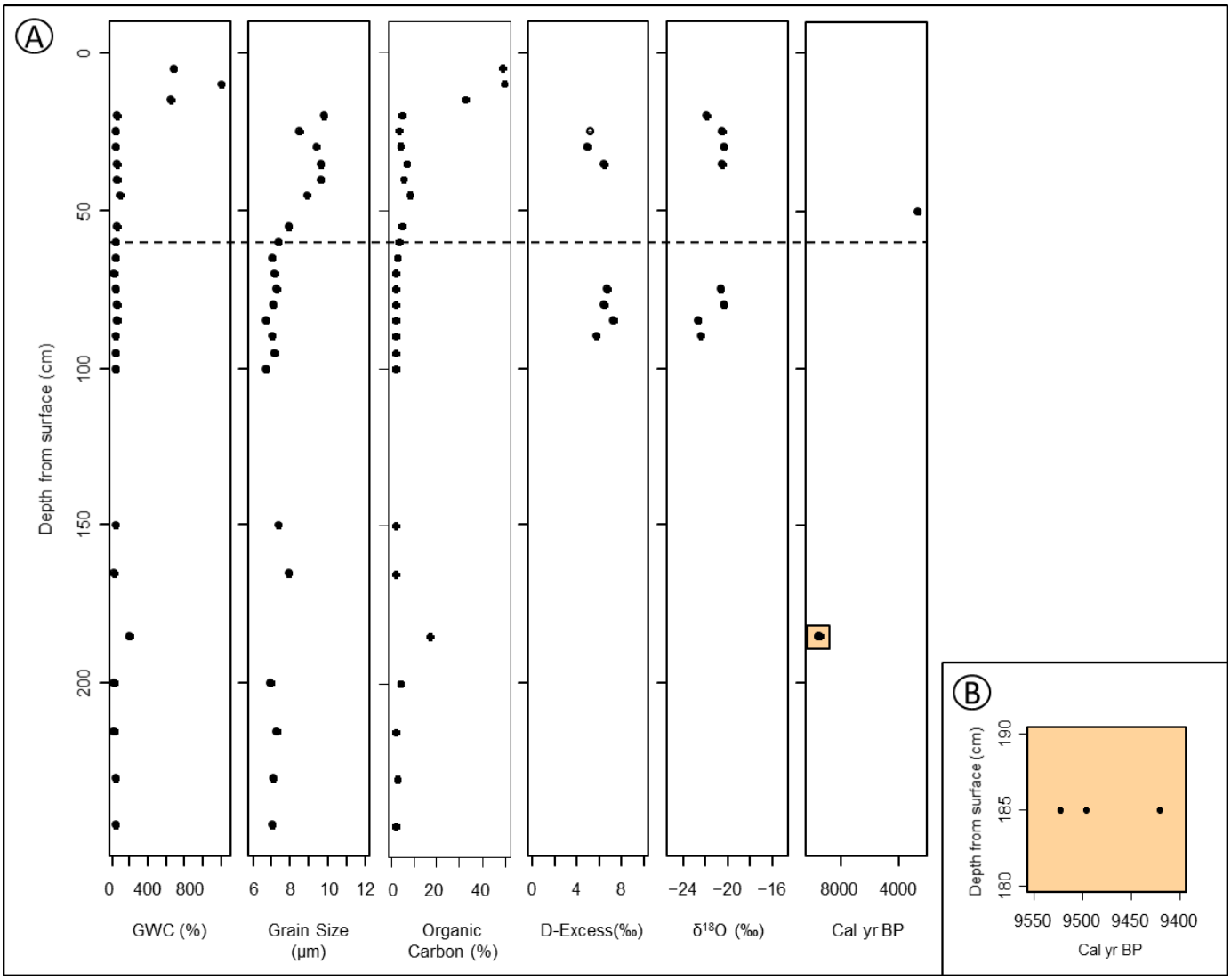

Fig. 5.3 **A.** Gravimetric water content (GWC), grain size, organic carbon content, Deuterium excess, $\delta^{18}O$, and radiocarbon dates of the thaw layer and relict thaw layer at Roger Thaw Slump, NWT (RTS; 67°37'05.2"N, 135°33'23.2"W, 350 m a.s.l.). Dashed line represents thaw layer thickness on August 1st 2016. Below is the relict thaw layer (RTL) **B.** Radiocarbon dates inset.

and an outlier of 94.3% at 45 cm of depth. Sediments of the TL consist of very fine to fine silts (7.9-9.8 µm). The organic carbon content is higher in the litter and hummus and in the 5 cm below these horizons (32.28-49.64%). The rest of the TL has an organic carbon content ranging from 3.38 to 8.1% with a peak at 45 cm depth.

5.2.2 Relict Thaw Layer

The relict thaw layer (RTL) has a lower GWC compared to the TL, ranging from 25.4 to 40.3%, with an outlier of 200%, which corresponds to a sample of buried organics (Fig. 5.3). The RTL sediments have smaller grains compared to the TL, with grain sizes corresponding to very fine silts (6.7-7.9 µm). The organic carbon content is also smaller. The values range from 1.97 to 4.31%, with an outlier of 16.98%, which also corresponds to the sample of buried organics.

5.2.3 Unit 2

Sediments from Unit 2 which are vertically banded with ice have varying GWC, with values ranging from 77.2 to 930.7% (Fig. 5.3). Sediments are within the range of clays and very fine silts (3.35-6.52 µm). The organic carbon content is low, varying between 10.1 and 12%.

5.3 Geochemistry

5.3.1 Dissolved Organic Carbon

The dissolved organic carbon (DOC) and $\delta^{13}C_{DOC}$ results of 35 massive ice samples and excess ice extracted from the RTL of RTS are shown in Fig. 5.4. DOC is highest in the ice taken from the RTL (30.15 ppm). Concentrations of the massive ice units range between 1.83 and 8.4 ppm and Unit 2 has slightly higher concentrations. $\delta^{13}C_{DOC}$ is also highest for the RTL (−26.33‰). For the massive ice units, values range from −29.82 and −26.89‰, and Unit 2 has a higher median and a bigger spread than the other three.

5.3.2 Major Ions

Fig. 5.5 shows the major ions concentrations for 51 massive ice samples and for excess ice extracted from the RTL of RTS. Unit 2 has higher concentrations and spread of values for SO^{4-},

NO^{3-}, Ca^{2+}, K^{+}, Mg^{2+}, and Na^{+}. Values are very similar for Cl^{-} and Fe^{+}, except for Unit 3 which is slightly lower concentrations of Cl^{-} and Unit 4 which has higher concentrations of Fe^{+}.

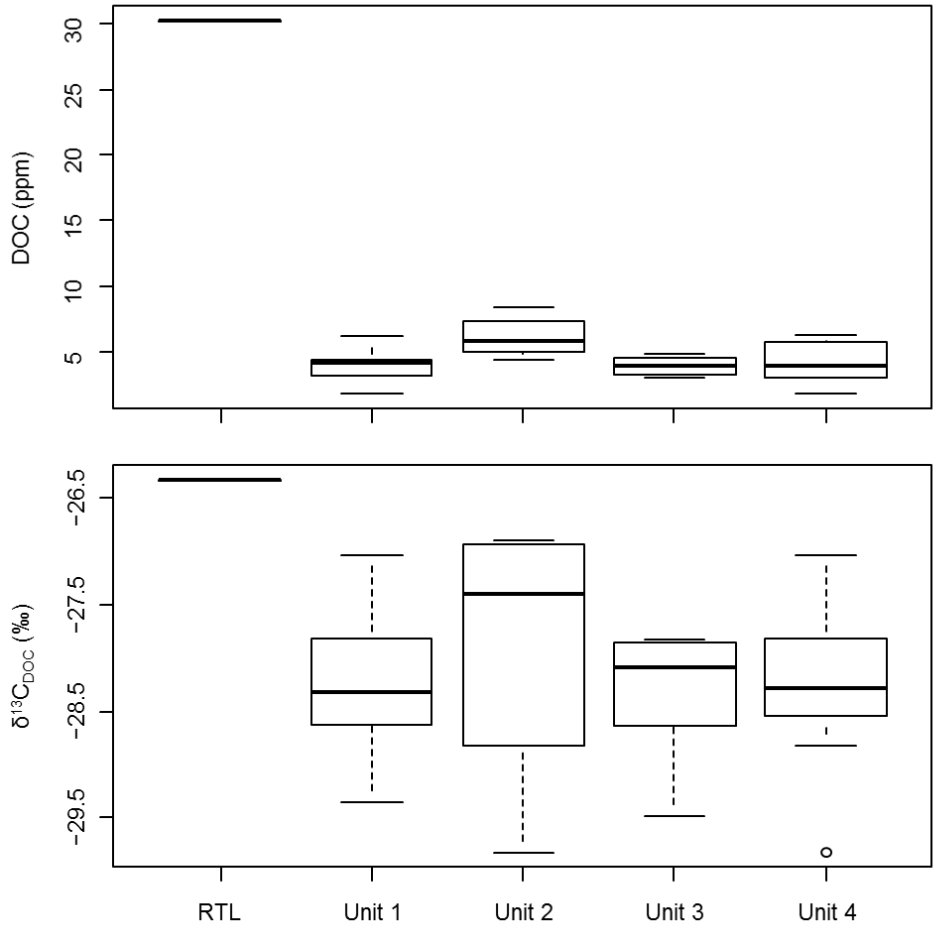

Fig. 5.4 Dissolved organic carbon (DOC) and $\delta^{13}C$ concentrations of ice from the relict thaw layer (RTL) and four massive ice units samples taken at Roger Thaw Slump, NWT (RTS; 67°37'05.2"N, 135°33'23.2"W, 350 m a.s.l.).

5.3.3 Stable Isotopes

$\delta^{18}O$ and D-Excess values for the TL and the RTL are shown in Fig. 5.3, and Fig. 5.6. The $\delta^{18}O$ values are higher in the TL and RTL, and the majority of the values are highest in the TL (−21.8-−20.4‰) then in the RTL (−22.7-−20.4‰). $\delta^{18}O$ is similar for Units 1 and 2 (−31.3‰-

−28.7‰), higher for Unit 3 (−28.2‰—27.3‰), and slightly lower for Unit 4 (−32‰-−29.5‰). D-excess is similar for the TL, the RTL, and Units 1 and 2. It is a little higher in the RTL (5.7-7.2‰) than in the TL (4.7‰-6.4‰). In comparison, Unit 3 values are lower (−0.5‰-2‰), and Unit 4 values are higher (5‰-9.8‰).

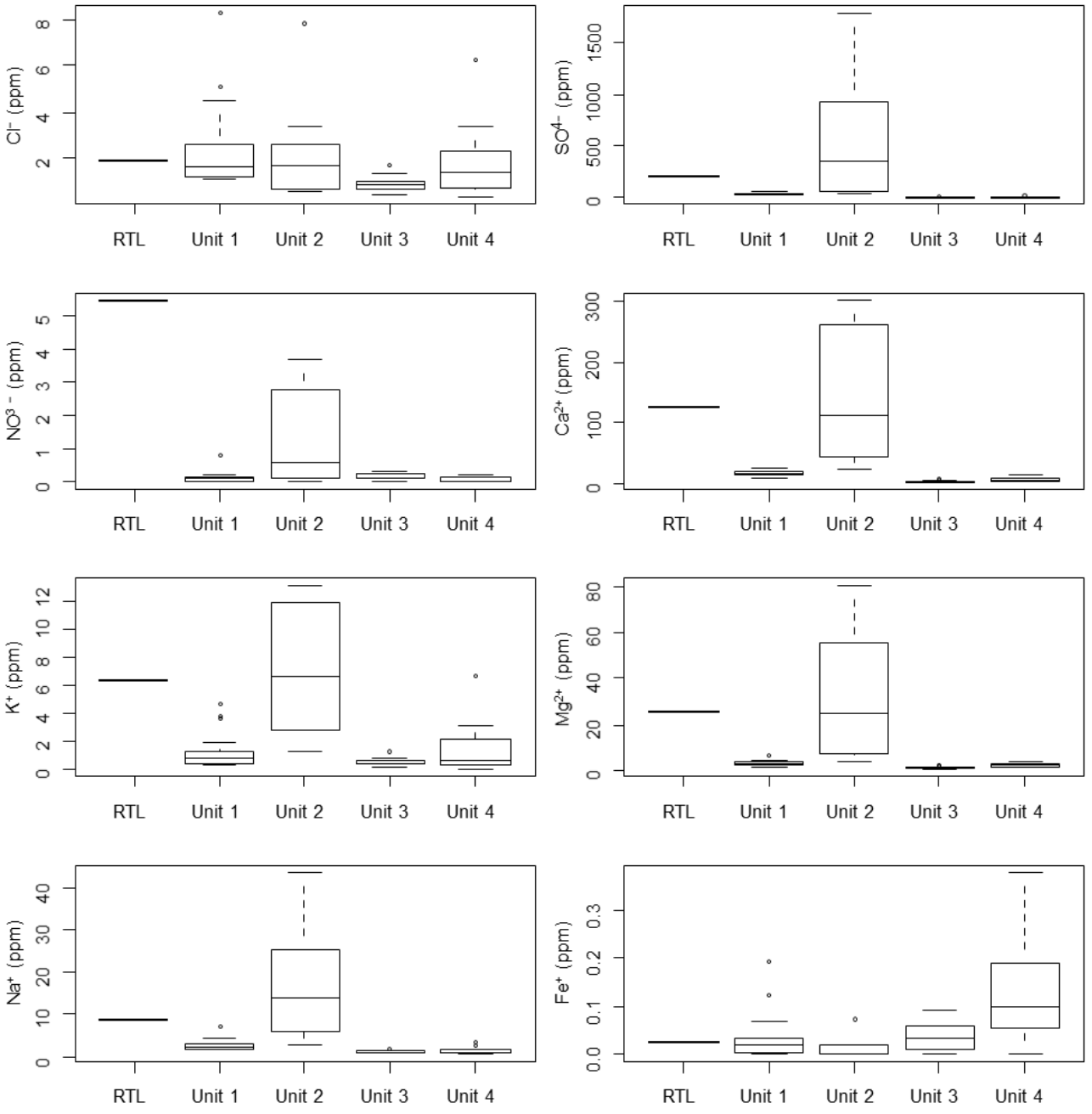

Fig. 5.5 Major anions and cations profile of ice from the relict thaw layer (RTL) and four massive ice units samples taken at Roger Thaw Slump, NWT (RTS; 67°37'05.2"N, 135°33'23.2"W, 350 m a.s.l.).

Correlation between δD and $\delta^{18}O$ is shown in Fig. 5.7 in comparison to the local meteoric water line (LMWL) for Inuvik, NWT ($\delta D = 7.3\ \delta^{18}O - 3.37$; Lacelle, 2011). All data sets have a high degree of correlation. The TL and RTL plot along higher regression slopes of 8.573 and 8.001 respectively, compared to the LMWL, whereas the four massive ice units have lower slopes of 6.539, 6.911, 5.64, and 6.3 respectively, which is especially true for Unit 3.

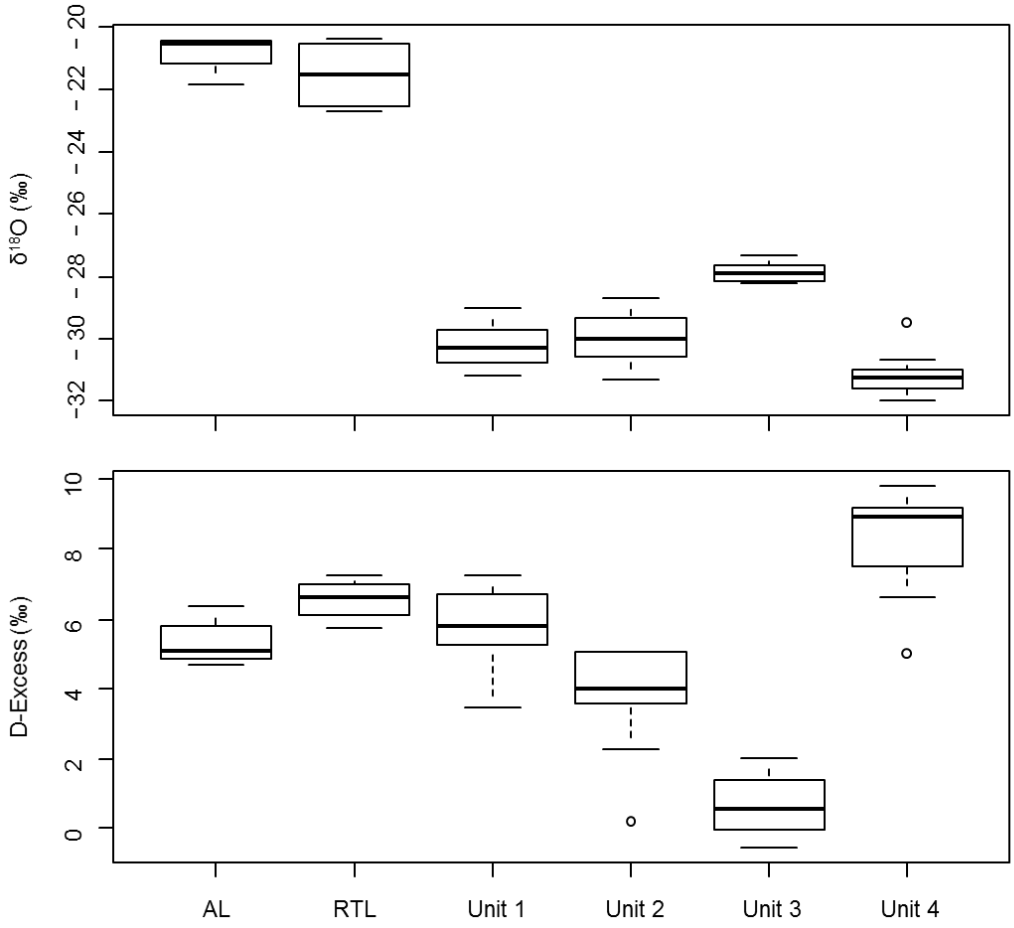

Fig. 5.6 Stable water isotope composition ($\delta^{18}O$ and Deuterium Excess) of ground water from the thaw layer (TL), ice from the relict thaw layer (RTL) and four massive ice units samples taken at Roger Thaw Slump, NWT (RTS; 67°37'05.2"N, 135°33'23.2"W, 350 m a.s.l.).

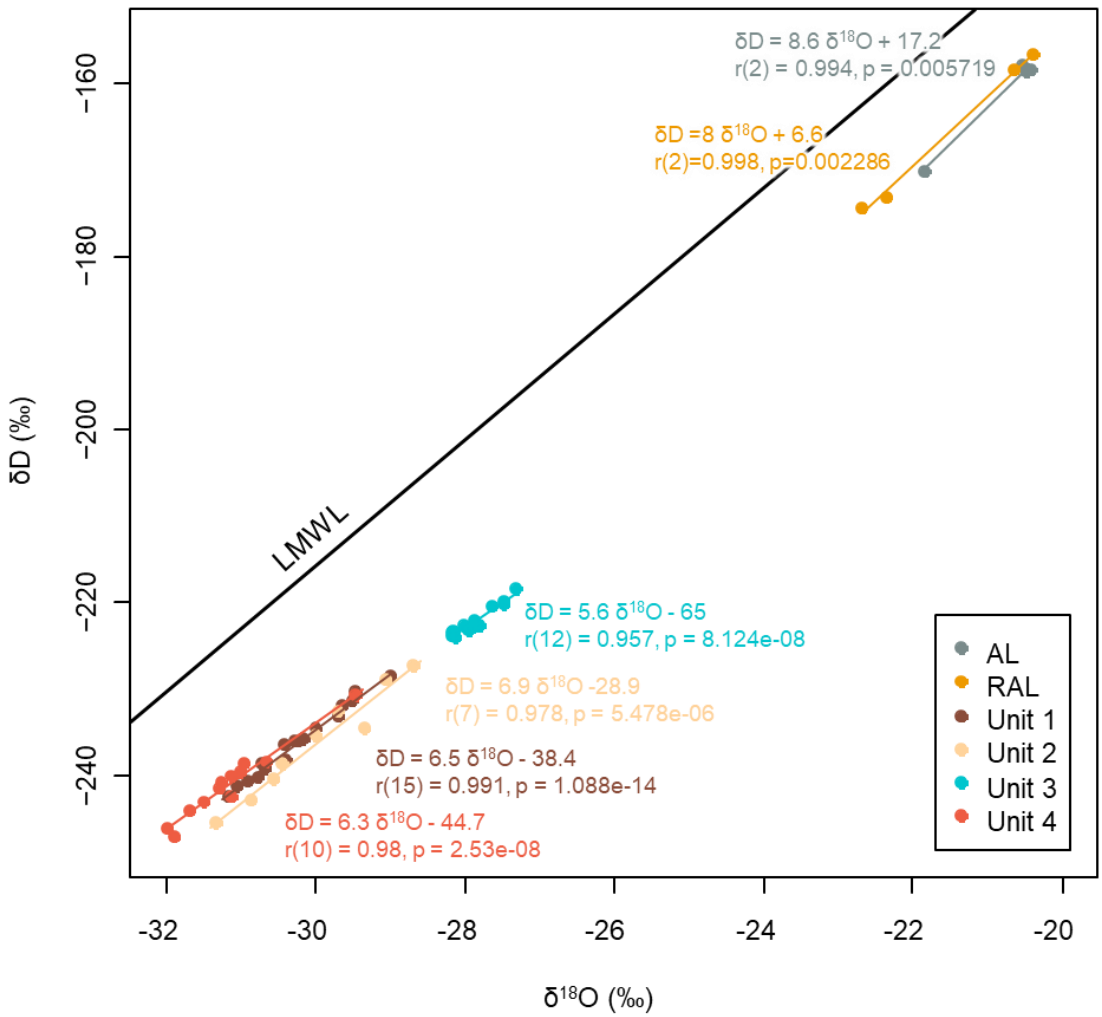

Fig. 5.7 δD and $\delta^{18}O$ scatter plot of ground water from the thaw layer (TL), ice from the relict thaw layer (RTL) and four massive ice units samples taken at Roger Thaw Slump ,NWT (RTS; 67°37'05.2"N, 135°33'23.2"W, 350 m a.s.l.). LMWL = Local Meteoric Water Line for Inuvik, NWT (δD = 7.3 $\delta^{18}O$ – 3.37; Lacelle, 2011). Pearson Product-Moment Correlation Coefficient shown as r(*df*)=*a*, p=*b*, where *df* is the degree of freedom, *a* is the correlation coefficient and *b* is the p-value.

Fig. 5.8 presents the correlation between D-Excess and δD. The TL plots on a positive slope (0.077) and the RTL on a very low positive slope (0.005). The four massive units, however, plot on highly negative slopes of −0.203, −0.106, −0.3, and −0.219, respectively. The degrees of correlation are fairly low for most of the data sets.

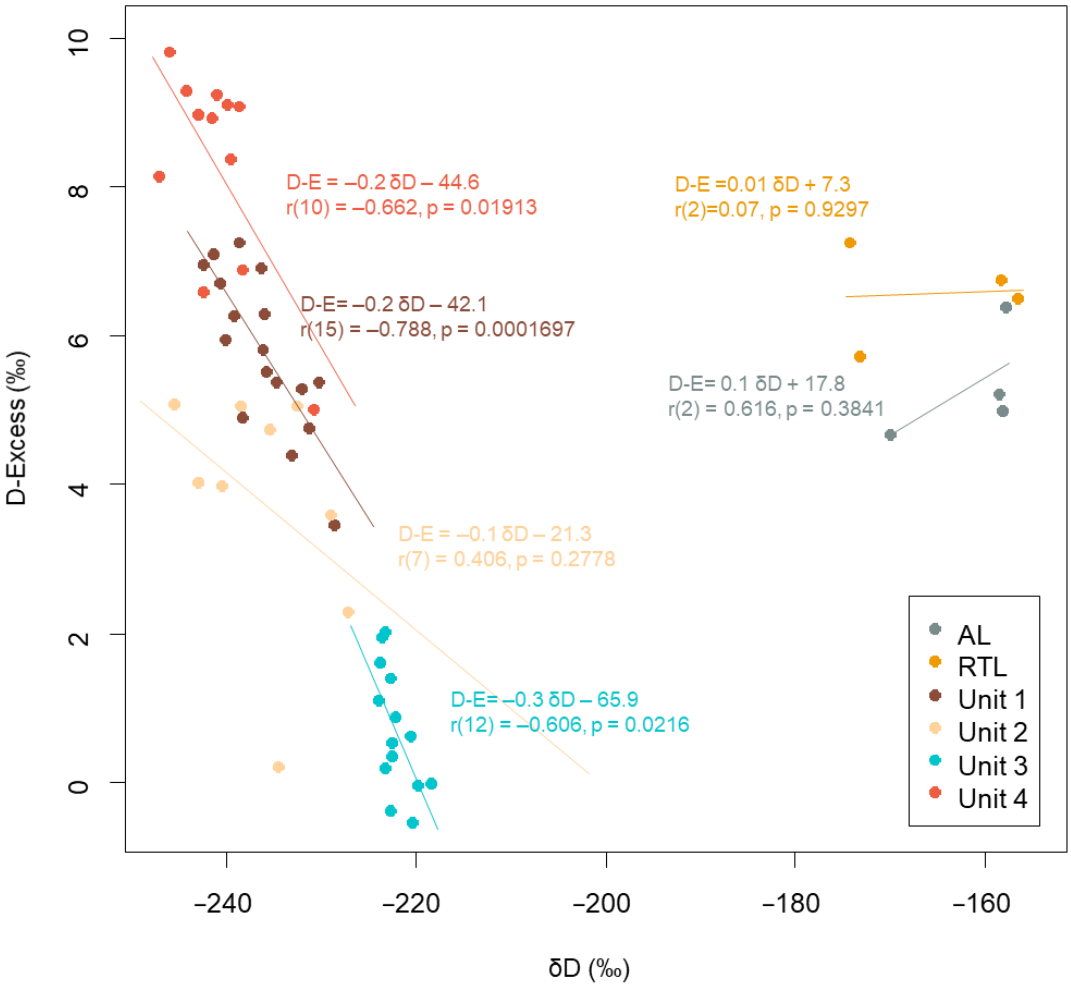

Fig. 5.8 δD and D-Excess scatter plot of ground water from the thaw layer (TL), ice from the relict thaw layer (RTL) and four massive ice units samples taken at Roger Thaw Slump ,NWT (RTS; 67°37'05.2"N, 135°33'23.2"W, 350 m a.s.l.).

5.4 Age Determination

Pieces of wood found at the bottom of the TL and leaves, wood and bulk fragments from buried organics in the RTL were radiocarbon dated (Fig. 5.3 and 5.9). The wood pieces at the bottom of the TL date to 2805 cal yr BP, where BP = AD 1950 (2860–2755 (95.4%)). The buried organics samples are dated to an average age of 9498.3 cal yr BP, with leaves fragment dating at 9460 cal yr BP (9540–9302 (95.4%)), wood fragments dating at 9534 cal yr BP (9560–9485 (95.4%)), and bulk fragments dating at 9501 cal yr BP (9539–9453 (95.4%)). Macrofossils were

also dated but results showed low confidence (9962–9531 (83.1%)) so they are not presented, and they are not included in the average age of the buried organics.

Lab ID	Sample ID	Material	Mat. Code	Method	^{14}C Age (yr BP)	cal yr BP[b]	Median cal yr BP	Location	Date sampled
UOC-3457	RS2-16-MI-23-A	Macrofossil	AAA	AMS	8717	10152-10053(8.3%) 10044-9986(4.0%) 9962-9531(83.1%)	9746	Roger Thaw Slump, NWT (67°37'05.2"N, 135°33'23.2"W).	August 1st 2016
UOC-3458	RS2-16-MI-23-B	Leaves fragment	AAA	AMS	8442	9540-9302(95.4%)	9460	Roger Thaw Slump, NWT (67°37'05.2"N, 135°33'23.2"W)	August 1st 2016
UOC-3459	RS2-16-MI-23-C	Wood	AAA	AMS	8566	9560-9485(95.4%)	9534	Roger Thaw Slump, NWT (67°37'05.2"N, 135°33'23.2"W)	August 1st 2016
UOC-2460	RS2-16-MI-23-D	Bulk (<1mm; >0.5mm)	AAA	AMS	8488	9539-9453(95.4%)	9501	Roger Thaw Slump, NWT (67°37'05.2"N, 135°33'23.2"W)	August 1st 2016
UOC-3461	RS1-16-11	Wood	AAA	AMS	2706	2860-2755(95.4%)	2805	Roger Thaw Slump, NWT (67°37'05.2"N, 135°33'23.2"W)	August 1st 2016

Fig. 5.9 Radiocarbon dating results.

Chapter 6: Discussion

6.1 Thaw Layer Thickness

Active layer thickness is recognized as being a function of three main factors: 1) shortwave radiation, 2) vegetation density and height, and 3) snowpack depth (Chang et al., 2015).

In summer, shortwave radiation warms the ground surface. In areas of denser and higher vegetation cover, such as forests and tall shrub tundra, this radiation cannot reach the ground surface as easily because of the vegetation cover and this moderates ground warming (Chang et al., 2015). Soil moisture, which influences the thickness of the organic layers of soil and the vegetation cover, also has an impact on the active layer thickness (Almeida et al., 2014; Fisher et al., 2016 ; Genx et al., 2012). For instance, important deep soil moisture often results in a shallower TL by insulating the ground through increased understory and forest canopy cover, while important surface soil moisture may lead to a deeper TL by increasing the thermal conductivity of the soil (Fisher et al., 2016). On the other hand, dried moss and peat layer in the summer have a smaller heat conductivity which leads to shallower TL (Fisher et al., 2016; Smith, 1975).

In winter, snow cover insulates the ground, limiting the influence of the atmosphere to the ground temperature. Snowpack thus reduces and delays the freezing of the ground (Chang et al., 2015). Snow accumulation is normally more important in denser and higher vegetation (Burn and McDonald, 2014; Chang et al., 2015; Kokelj et al., 2010; Palmer et al., 2012; Roy-Léveillé, Burn and McDonald, 2014; Thompson et al., 2004). Therefore, areas of dense and high vegetation cover are expected to have cooler ground temperatures in the summer and warmer ground temperatures in the winter compared to areas of sparse and low vegetation cover. It is then possible to affirm that permafrost areas with denser and higher vegetation should be characterized by shallower

active layer thicknesses and permafrost areas with sparse and lower vegetation by deeper active layer thicknesses in summer.

However, active layer thickness patterns are often more complicated than explained above, as other factors do impact permafrost temperature. For example, Roy-Léveillé, Burn and McDonald (2014) found unexpected lower annual mean near-surface permafrost temperature in taiga patches than in shrub tundra. This ground temperature inversion was related to the taiga patches being large enough to limit snow accumulation and the wind-blown snow being trapped at the patches edge. Therefore, not only the snow-holding capacity of the local vegetation, but also the larger scale conditions which control snow input, such as being surrounded by high vegetation that has the capacity to trap wind-blown snow, influence the snow cover depth and, consequently, near-surface permafrost temperature (Pomeroy et al., 1995; Roy-Léveillé, Burn and McDonald, 2014; Smith, 1975). Similarly, O'Neill et al. (2015), studying annual mean near-surface permafrost temperature in different vegetation covers at different elevations on the Peel Plateau, found that, in tundra sites, there is no correlation between mean maximum vegetation height and late winter snow depth. They suggest that vegetation acts as a secondary control of snow depth at the site scale. Mesoscale controls, such as topography and winds, would have a more important impact on snow accumulation (O'Neill et al., 2015). Furthermore, the difference in ground temperature in forest compared to tundra is usually explained by deeper snow covers in forest, as expressed by the vegetation height-snow depth relation. However, O'Neill et al. (2015) describe that since snow accumulation can also be significant in tundra sites on the Peel Plateau because of mesoscale controls, the importance of the timing of snow accumulation also has considerable impact on near-surface ground temperature. By monitoring snow accumulation at a high elevation dwarf shrub tundra site (same as this study's DST site) and at a low elevation spruce forest site (same as this

study's LSF site), they found that >90 cm of snow accumulated by early November in the tundra, whereas snow depth in the forest reached 90 cm in early February. This more gradual snow accumulation at the LSF site partially explains why the annual mean near-surface permafrost temperature is higher in the DST site, and it may also explain the discontinuity our data shows in the thaw layer thickness at the DST site. That is because even though considerable amounts of snow accumulated at the DST site, the tundra was isolated from atmosphere conditions earlier in winter. Another important factor that may have contributed to the warmer near-surface permafrost temperature at the DST site is the air temperature regime, which shows strong inversions between the high elevation DST site and the low elevation LSF site during the winter. This causes for daily mean air temperature to be frequently higher at the DST site than at the forest site, especially during the coldest months (55% of the days when forest air temperatures were below 0°C), and for a greater number of freezing degree days to occur in the forest.

Therefore, although active layer thickness is usually monitored and analysed based on its summer conditions, and thus is strongly associated with summer temperatures and vegetation cover type, winter conditions seem to also have a considerable influence, mainly because of the mesoscale conditions modifying the snowpack, the timing of the snow accumulation, and, in mountainous regions, winter air temperature inversions. The gradient and discontinuity of the thaw layer thicknesses measured at our six sites may therefore be caused by residual effects of winter conditions on the region.

6.2 Massive Ground Ice Origin

Based on the visual aspect of the four massive ice units in this study, the nature of the contact between them and the overlying sediments, their geochemistry, and a comparison of their

geochemistry with that of the ice contained in the overlying sediments, the massive ice exposed at Roger Thaw Slump (RTS) shows evidence of both typical massive ground ice origins in northwestern Canada; buried glacier ice and segregated-intrusive ice.

The four massive ice units contain very little sediments and that is consistent with glacier ice, as segregated ice usually has relatively high particle content (Lorrain and Demeur, 1985). Moreover, the fact that Unit 2 is banded with sediments supports the hypothesis that this ice could be basal glacier ice, which is often stratified with sediments (French and Harry, 1990). The contact between the ice units and the RTL is sharp and corresponds to a thaw unconformity, which points towards a glacier ice origin. Also, no trend exists between the geochemistry of the massive body and the ice in the overlying sediments. That is shown by the difference in the δD and $\delta^{18}O$ slopes, which is higher for the RTL ice (8.001) compared to the massive ice units (6.539, 6.911, 5.64, 6.3) (Fig. 5.8), and by the difference in the D-Excess and δD slopes, which is much lower and positive for the RTL ice (0.005) compared to the massive ice units which are highly negative (−0.203, −0.106, −0.3, −0.219) (Fig. 5.9). DOC concentrations are also low in Units 1, 3, and 4 (Fig. 5.5), as can be expected for buried glacier ice (Fritz et al., 2015). Unit 2 values are a little higher, which is consistent with the higher concentrations it presents for most ions. As highlighted above, Unit 2 is stratified with sediments which points towards a basal glacier ice origin, and this type of ice can be defined as segregation-intrusive ice because it has experienced regelation (French and Harry, 1990), which explains the higher DOC concentrations.

On the other hand, the fact that Units 1 and 3 show elongated air bubbles is more consistent with the segregated-intrusive ice origin. Also, the D-Excess-δD slopes (Fig. 5.9) point towards a segregated-intrusive ice origin of the units, as explained by Lacelle (2011). The four massive ice units plot on a highly negative slope that corresponds to freezing of water under equilibrium

conditions. The δD-$\delta^{18}O$ relation is also expected to plot on a lower slope compared to the LMWL (<7.3) for segregated-intrusive ice. In the case of the massive ice units, all four plotted on lower slopes than 7.3 (Fig. 5.8).

Another important factor to take into account is that our site is located at the western margin of the Laurentide Ice Sheet. Marginal glacier ice presents varying facies and chemical parameters, as there may be open-system refreezing within basal cavities that form at the glacier margins (Hubbard and Sharp, 1995).

Our hypothesis is therefore that the ice exposed at RTS is buried glacier ice that experienced water infiltration and partial refreezing, because of the physical evidence (i.e. lack of sediments or stratified sediments, sharp contact, varied bubble aspects, variations in colorations), and because of the chemical evidence (i.e. varied isotopic composition, absence of a trend between the massive body and the ice in the overlying sediments, varied DOC concentrations). We could characterize this type of massive ice as a co-existence of basal and segregated ice, which would have formed within the margin of the Laurentide Ice Sheet (Waller, Murton and Knight, 2009). The important thickness of this buried glacier ice can be explained by the glacier being polythermal, meaning that it experienced both warm and cold-based conditions, causing melting and refreezing which contributes to the accretion of new and existing ice (and sediments) onto the bottom of the glacier (Moorman and Murton, 2000; Waller, Murton and Knight, 2009). During the deglaciation, stagnation of the ice sheet, permafrost aggradation and burial by melt-out of till from the ice surface would have preserved the marginal ice (Waller, Murton and Knight, 2009).

6.3 Relict Thaw Layer

The layer of material of lighter color situated between the sharp upper contact of the massive ice units and the thaw layer was already identified as being a relict thaw layer (RTL) (Fig. 5.1). Indeed, sediments found above a thaw unconformity generally have a lighter coloration (Burn, 1997). Additionally, the fact that buried organic sections were found within that layer is indicative of it being a RTL. There are two scenarios that could explain the origin of the presence of these organic sections; They could have been incorporated in the soil during a period of permafrost degradation and active layer deepening by cryoturbation (Burn, 1997; Mackay, 1981), or Roger Thaw Slump could be located on the floor of an ancient thaw slump where the slumped vegetation was incorporated in the soil following permafrost aggradation. Radiocarbon dating of materiel from one of the buried organic sections gave an average age of 9498.3 cal yr BP (Fig. 5.3). This age represents an indication of the period of maximum active layer deepening. It is consistent with the Holocene thermal maximum and its warm and humid climate in northwestern Canada between ca. 12.2 and 5.6 ka (Clark et al., 2004; Delorme et al., 1977; Kaufman et al., 2016; Ritchie and Hare, 1971). It represents a period of important active layer deepening and thermokarst activity that resulted in widespread paleo-thaw unconformities in northwestern Canada (Burn, 1997; Burn, Michel and Smith, 1986; Fritz et al., 2016; Kokelj, Smith and Burn, 2002; Mackay, 1992, 1978; Malone et al., 2013; Murton, 2001; Murton and French, 1993, 1994; Rampton, 1982; Worsley, 2000)

The Holocene thermal maximum relict thaw layer hypothesis is also supported by the oxygen isotopic composition of the ground ice (Fig. 5.7). It is typical to find ice of low $\delta^{18}O$ ($<-27‰$) below a paleo-thaw unconformity and ice of higher $\delta^{18}O$ ($>-25‰$) above it (Burn, 1997). That explains how the ice below the unconformity was formed from Pleistocene water, and the ice

above it is a mix of Pleistocene and Holocene water of higher ^{18}O concentration, giving it its less negative $\delta^{18}O$ values (Fritz et al., 2016; Mackay, 1983; Murton and French, 1994)

Moreover, the ice content of the RTL provides information on the rate of aggradation of the permafrost table following the active layer deepening responsible for the paleo-thaw unconformity. As explained above, an ice rich layer may form just below the permafrost table during a slow permafrost aggradation in relation with water migrating through the active layer to the freezing front and being incorporated to the permafrost (Harry, 1986; Mackay, 1972; O'Neill and Burn, 2012). For instance, a study conducted near Inuvik, NWT by Kokelj and Burn (2003) has related ice-poor material beneath the permafrost table with a rapidly aggrading permafrost, and ice-rich material with a period of permafrost table stability. The low GWC and the absence of excess ice in the RTL is therefore indicative of a rapidly aggrading permafrost table following the creation of Roger Thaw Slump.

6.4 Thaw Slump Activity during the Holocene

Thaw slump initiation in highlands is the result of ground ice ablation following ice-rich permafrost exposure through active layer deepening and detachment which has been related to wildfires, warmer summer and annual air temperatures, and water tracks or streams formation following important rainfall events (Burn and Lewkowicz, 1990; Kokelj, Zajdlik and Thompson, 2009; Lacelle et al., 2010; Lantz and Kokelj, 2008; Lewkowicz and Harris, 2005). When plotting events of thaw slump activity (i.e. initiation and retrogression) in the Richardson Mountains against insolation values, temperature and precipitations anomalies, and elevation, two distinct periods of thaw slump activity seem to emerge (Fig. 6.1).

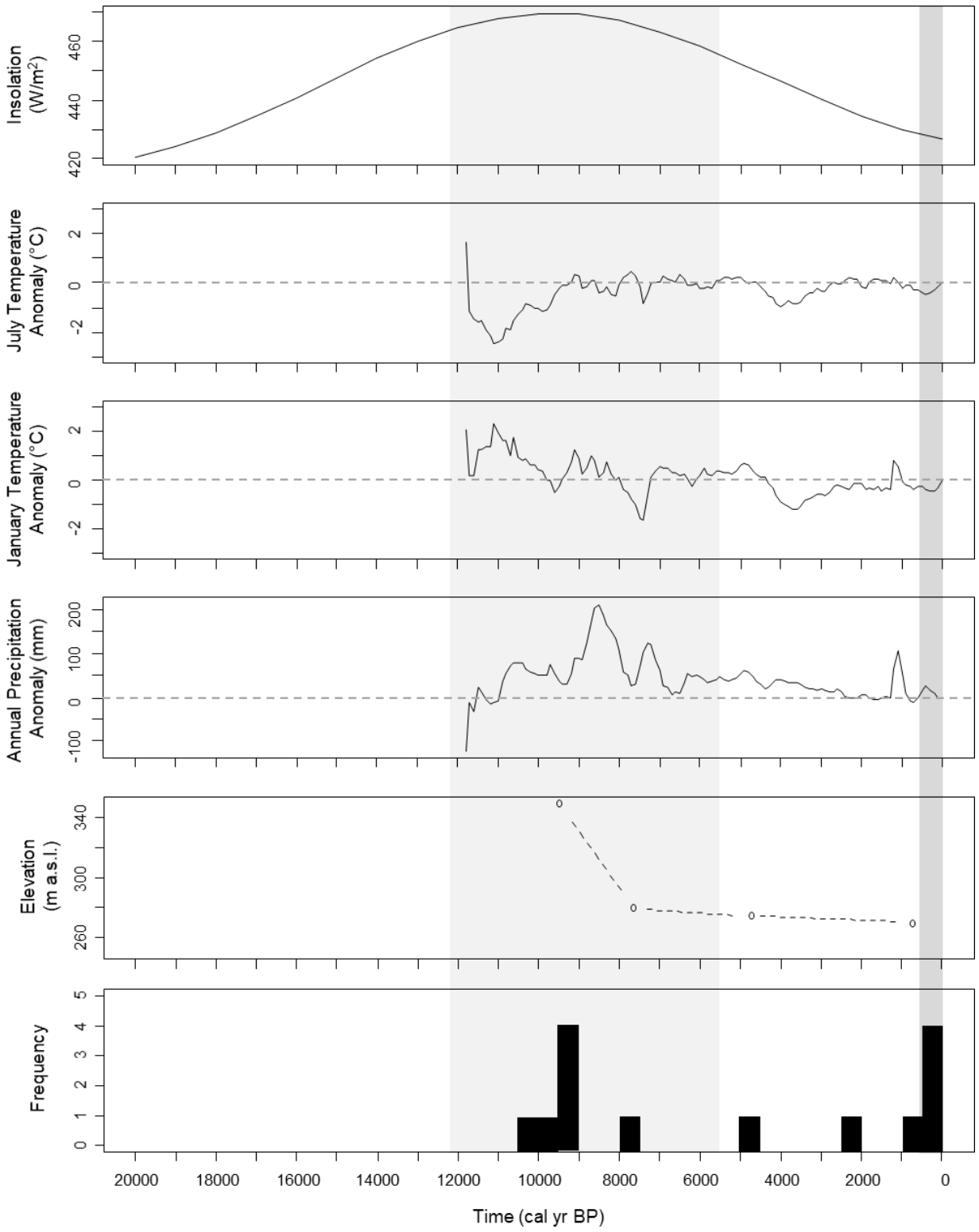

Fig. 6.1 Insolation (July 65°N, Berger and Loutre, 1991), July temperature, January temperature and annual precipitation anomalies for western Canada (Viau and Gajewski, 2009), elevation of stream incisions in the Bonnet Plume Creek terraces (Lacelle et al., 2010), and thaw slumps activity in the Richardson Mountains region (Lacelle et al., 2004; this study). The light gray area represents the extent of the Holocene Thermal Maximum, and the dark gray shaded area represents the extent of the Little Ice Age.

The most recent period took place in the late Holocene and four out of the five events of thaw slumps activity dated correspond to the Little Ice Age (AD 1400-1900 = 550-50 yr BP, where BP = AD 1950), which could indicate that cooler air temperatures are susceptible to trigger thaw slump activity. These thaw slumps were also active during a period of positive precipitation anomalies, therefore linking thaw slump activity to important precipitations. Observation of 70 modern thaw slumps in the Richardson Mountains by Lacelle et al. (2010) has revealed that in 68% of the cases (46 out of 70) thaw slumps were initiated during a period of cooler air temperature (1930-1950), which is also known as a period being wetter than present-day (Wahl et al., 1987). On the other hand, this study found that the rate of thaw slumps initiation increased between the periods of 1954-74 and 1985-2004 from 0.35 new thaw slumps per year to 0.68, a trend that follows the 10-year running average summer air temperature, but that is inversely related to the 10-year total precipitation record. This is however contradicted by a study conducted by Kokelj et al. (2015) of thaw slumps number and size in the Peel Plateau which looks at a more extensive period of time. It shows that since the mid-‘80s, no trend with summer temperatures (1986-2010) exists but rather a strong correlation with increased magnitude and intensity of rainfall. Colder air temperatures being linked to thaw slump activity is also observed on the Fosheim Peninsula on Ellesmere Island in Canada’s High Arctic. The peninsula has a much colder and drier climate compared to the Peel Plateau, with a mean annual air temperature of -19.7°C and mean annual precipitations of 64 mm, with 60% of it being snow (Pollard and Bell, 1998; Pollard 2000). Nevertheless, many thaw slumps occur in the region (Pollard, 1991; Robinson, 2000; Robinson and Pollard, 1998)

The second period of important thaw slump activity occurs between 10236 and 9071 cal yr BP (10439-10120 (83.9%)-9288-8858 (91%)), which falls within the extent of the Holocene

Thermal Maximum (HTM). In western Canada, July temperatures experienced an increase between 11 and 9 ka and stayed fairly high until after 5 ka (Fig. 6.1; Viau and Gajewski, 2009). Paleoclimate reconstructions of northwestern Canada suggest a general warming of temperatures between approximately 12.2 and 5.6 ka, with maximum temperatures being reached between 7 and 5 ka (Kaufman et al., 2004, 2016). Also, the region was wetter than present-day during the vast majority of the Holocene and most significantly between 11 and 7 ka (Fig. 6.1). Thaw slump initiation during the HTM can be linked to warmer air temperatures and important precipitations. Six out of the seven HTM thaw slumps dated to a period of important July temperature and annual precipitation increase (Fig. 6.1).

While it is not possible to make a direct relation between thaw slump activity and large-scale fluctuations in air temperatures based on these two periods of thaw slump activity, they seem to have at least one thing in common: increased precipitations. This is consistent with thaw slump initiation and growth being associated with important rainfall events, as they can create stream tracks susceptible to induce active layer deepening and detachment and as they contribute to evacuation of the slumped sediments that accumulate at the base of the headwall, keeping the thaw slump active (Kokelj et al., 2015; Lacelle, Bjornson and Lauriol, 2010; Lacelle et al., 201;). However, in order for these effects of precipitations to take place, the landscape must also present favourable settings. Thaw slump activity in the Richardson Mountains-Peel Plateau has been associated with post-glacial stream network incision (Kokelj et al., 2017, 2015; Lacelle, Bjornson and Lauriol, 2010; Lacelle et al., 2015). Stream incision occurs through water channel eroding the bedrock and moving the sediments downstream (Phillips and Robert, 2005). Incision rates are usually highly influenced by precipitation rates (Ferrier, Huppert and Perron, 2013) and, in formerly glaciated regions by direct meltwater and fluctuations in proglacial lakes level (Phillips

and Robert, 2005). When scars of stream systems larger than present-day are visible in the landscape, it usually represents an evidence of the action of wetter paleoclimates and deglaciation meltwater (Phillips and Robert, 2005). After the deglaciation, the rapid initial development of the fluvial system in the Richardson Mountains has led to unstable slopes across the landscape, creating conditions suitable to the exposure of ice-rich permafrost and thaw slump initiation (Lacelle et al., 2010). The stream network has been developing ever since and the decrease in age with elevation of the stream incision in Bonnet Plume Creek terraces (Fig. 6.1) support the idea that it is still gradually being incised downslope (Lacelle et al., 2010).

When analyzing the spatial distribution of thaw slumps in northwestern Canada, coastline and fluvially incised environments are the areas that are the most susceptible to thaw slump occurrence because of their sensitivity to erosion and their more pronounced relief (Kokelj et al., 2017). These sensitive areas are described by Kokelj et al. (2017) as being driven by their past climate, ground thermal conditions, topography, and geomorphic settings. The formerly glaciated continuous permafrost moraine dominated terrains of the Richardson Mountains-Peel Plateau are ice-rich and have a relative relief because of stream incision, and that makes them prone to the creation of large thaw slumps, especially during increased precipitation periods (Kokelj et al., 2017, 2015; Lacelle et al., 2015). In fact, many thaw slumps in the region are located on or at the base of hillslopes along streams (Lacelle et al., 2015). When looking at an aerial view of the region, it becomes clear that many thaw slumps in the region are distributed following the fluvial network. That is also the case for Roger Thaw Slump, which is located along one of the tributaries of Longstick River.

Moreover, the vast majority of the thaw slumps in the region occur between the Last Glacial Maximum Limit (LGM) and the Tutsieta Lake Phase limit, an area characterized by ice-rich broad hummocky rolling moraine terrain (Duk-Rodkin and Hughes, 1992; Hughes et al., 1972). Indeed, analysis of qualitative data from 121 seismic shothole drillers' log records (Smith and Lesk-Winfield, 2012) has revealed that between the LGM and Tutsieta Lake Phase, ground is more likely to contain ice, with about 70% of shotholes having massive ice within 4 meters below the surface (Fig. 6.2). On the other hand, only 28 to 44% of shotholes east of the Tutsieta Lake Phase showed evidence of massive ice above 4 meters.

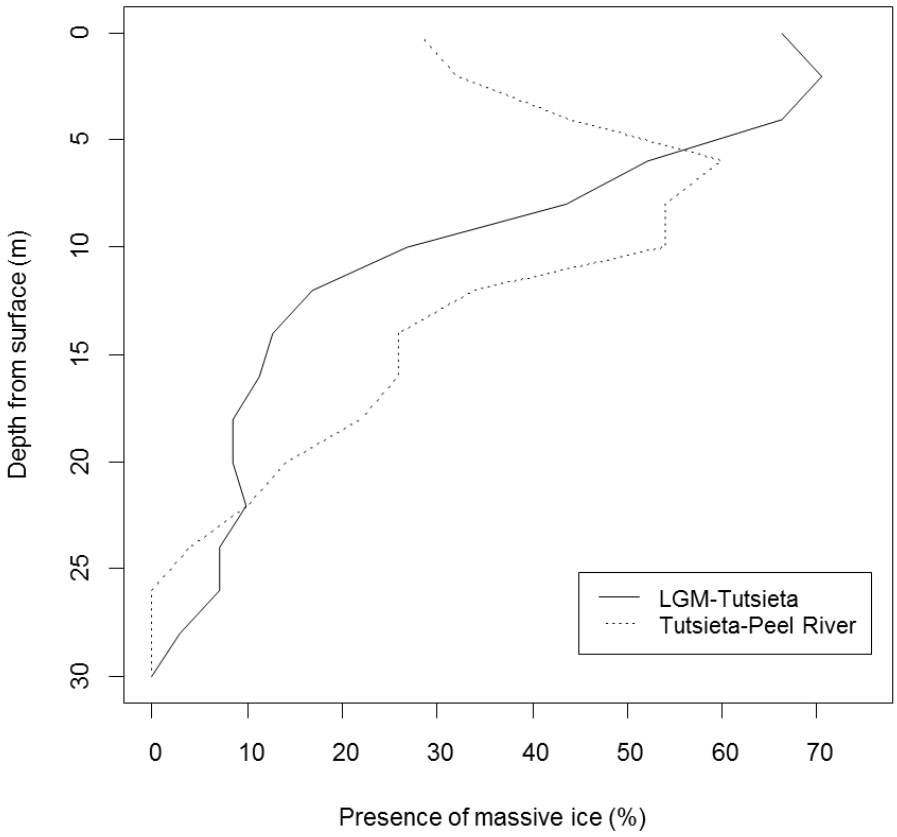

Fig. 6.2 Comparison of shotholes massive ice occurrence at given depths between the Last Glacial Maximum (LGM) and the Tutsieta Lake Phase, and between the Tutsieta Lake Phase and the Peel River.

Therefore, stream incision of ice-rich ground results in slope instability and easy removal of slumped sediments and creates a landscape that has a great potential for thaw slump activity (Lacelle et al., 2015), while precipitation increase plays a role in augmenting this potential (Kokelj et al., 2015). For Kokelj et al. (2017), the most recent period of thaw slump activity shows how permafrost has delayed the postglacial landscape modifications, and they qualify it has being a resumption of deglaciation and postglacial processes, with the main driver being increased rainfall.

Overall, Roger Thaw Slump represents a witness of its region's climate history since the Last Glacial Maximum. Throughout the glaciation, ice and meltwater accreted on the base of the LIS, forming a thick layer of basal ice. During the deglaciation, the glacier thinned at its margins, permafrost aggregated and till buried the ice, preserving it. Following the deglaciation, the rapid initial stream network incision created a relief susceptible to slope instability and mass wasting. During the Holocene Thermal Maximum, the warm and humid climate caused active layer deepening and detachment following the stream network and this led to the initiation of many thaw slumps. Following that, permafrost aggregated rapidly, leaving a paleo-thaw unconformity marking the extent of a relict thaw layer.

Chapter 7: Conclusions

7.1 Conclusions

Studying the headwall of Roger Thaw Slump enabled us to make detailed observations of the thaw layer, the relict thaw layer, and four massive ice units. These contribute to the understanding of the genesis of thaw slumps and how they fit in the climate history and terrain conditions of the region. We were able to draw the following main conclusions:

a) Summer air temperatures, vegetation cover type (height and density), mesoscale conditions modifying the snowpack, timing of the snow accumulation and winter air temperature inversions are the main drivers of active layer thickness in the Richardson Mountains-Peel Plateau.

b) The physical and chemical parameters of the four units of massive ground ice exposed at Roger Thaw Slump are characteristic of buried glacier ice that experienced water infiltration and partial refreezing. This layer most likely formed at the margin of the Laurentide Ice Sheet as it was experiencing an alternation of warm and cold-based conditions, causing melting and refreezing which contributes to the accretion of ice onto the bottom of the glacier. During the deglaciation, this ice was preserved by glacier stagnation, permafrost aggradation and till burial.

c) The layer above the massive ground ice and below the thaw layer at Roger Thaw Slump, which presents a lighter coloration, buried organic sections, and ice of low $\delta^{18}O$ values, is identified as a relict thaw layer (RTL). It dates to the Holocene thermal maximum, which represents a period of important active layer deepening and thermokarst activity that resulted in widespread paleo-thaw unconformities across northwestern Canada.

d) The combination of formerly glaciated continuous permafrost, hummocky rolling moraine terrain, stream-incised relief, and massive ground ice in the Richardson Mountains, coupled with major rainfall events, represents a set of condition that is favourable to thaw slump activity (i.e. initiation and retrogression), by inducing slope instability and easy removal of slumped sediments.

7.2 Limitations of Study

Limitations of this study mainly concern field methods and sampling. The profile of the thaw layer and the relict thaw layer was done by combining data from the core extracted on top of the thaw slump and from the samples taken with a trowel from the headwall. It would have been more precise to be able to either core down to the bottom of the relict thaw layer, or to take all of the samples from the headwall. However, giving the depth of the thaw unconformity (2.5 m) and the height of the headwall (5-6 m), it was only possible to do one series of sampling in the same place. This resulted in a gap in the soil profile, has seen in Fig. 5.3. Generally, it would have been very useful to be able to undergo a second field season to fill in the gaps, but the headwall would have still been difficult to access.

This thesis is based on one thaw slump and it would have been interesting to include more thaw slumps and do the same type of analyses. The recent data published on the region was nevertheless efficient in supporting this study. Also, only one section of buried organics was sampled and used to date the thaw slump. This is again due to hard accessibility of the headwall. More dates would have added confidence to the chronological results.

Finally, there are some limitations concerning the link made between thaw slump activity and increased precipitations during the Holocene, because it is impossible to differentiate between

rain and snow when working with paleo-climatic reconstructions as the seasonal variability determining the limit between rainfall and snow varied.

7.3 Future Work

More thaw slumps could be studied on the regional scale, to further support the idea that stream-incised, ice-rich permafrost in formerly glaciated areas present great potential for thaw slump activity. Also, dating more thaw slumps would help strengthen the link between thaw slump activity and precipitations, or possibly establish a relation with air temperatures.

Furthermore, as highlighted in this study, distinguishing between ground ice origin being glacier ice or segregated-intrusive ice is very difficult. It would be interesting to study more massive ground ice, especially by comparing formerly glaciated and unglaciated regions and how they react during periods of increased thermokarst activity.

Finally, the discontinuity of the thaw layer thicknesses measured at our six sites was linked to residual effects of winter conditions in the region. Measuring the active layer at the end of the summer season would determine if this residual effect fades during the summer or if active layer thickness is also strongly related to winter conditions.

References

Almeida, I.C.C., Schaefer, C.E.G.R., Fernandes, R.B.A., Pereira, T.T.C., Nieuwendam, A., Pereira, A.B. (2014). Active layer thermal regime at different vegetation covers at Lions Rump, King George Island, Maritime Antarctica. *Geomorphology, 225,* 36-46. doi: 10.1016/j.geomorph.2014.03.048

Anisimov, O. A., Shiklomanov, N.J. and Nelson, F.E. (1997). Effects of global warming on permafrost and active layer thickness: results from transient general circulation models. *Global and Planetary Change, 15*(3), 61–77. doi: 10.1016/S0921-8181(97)00009-X

Beget, J. (1987). Low profile of the northwest Laurentide ice sheet. *Arctic & Alpine Research, 19*(1), 81-88. doi: 10.2307/1551003

Berman, E. S. F., Levin, N., Landais, A., Li, S., & Owano, T. (2013). Measurement of $\delta^{18}O$, $\delta^{17}O$, and ^{17}O-excess in Water by Off-Axis Integrated Cavity Output Spectroscopy and Isotope Ratio Mass Spectrometry. *Analytical Chemistry, 85*(21), 10392-10398. doi:10.1021/ac402366

Broadbent, F.E. (1953). The soil organic fraction. *Advances in Agronomy, 5,* 153-183.

Brock. F, Higham T, Ditchfield P, Bronk Ramsey C. (2010). Current pretreatment methods for AMS radiocarbon dating at the Oxford Radiocarbon Accelerator Unit (ORAU). *Radiocarbon, 52*(1), 103–12. doi: 10.1017/S0033822200045069

Bronk Ramsey, C. (2009). Bayesian analysis of radiocarbon dates. *Radiocarbon, 51,* 337–360.

Burn, C. R. (1997). Cryostratigraphy, paleogeography, and climate change during the Early Holocene warm interval, western Arctic coast, Canada. *Canadian Journal of Earth Sciences, 34*(7), 912-925. doi:10.1139/e17-076

Burn, C.R. (2000). The thermal regime of a retrogressive thaw slump near Mayo, Yukon Territory. *Canadian Journal of Earth Sciences, 37*(7), 967-981. doi: 10.1139/e00-017

Burn, C.R. and Lewkowicz, A.G. (1990). Canadian Landform Examples – 17 Retrogressive Thaw Slumps. *The Canadian Geographer, 34*(3), 273-276. doi: :10.1111/j.1541-0064.1990.tb01092.x

Burn, C.R., Michel, F.A., and Smith, M.W. (1986). Stratigraphic, isotopic, and mineralogical evidence for an early Holocene thaw unconformity at Mayo, Yukon Territory. *Canadian Journal of Earth Sciences*, 23(6), 794-803. doi:10.1139/e86-081

Callaghan, T.V. and Jonasson, S. (1995). Implications for changes in Arctic plant biodiversity from environmental manipulation experiments. In Chapin, F.S. III and Körner, C.H. (eds.).

Arctic and Alpine Biodiversity: Patterns, Causes and Ecosystem Consequences (151–164). Springer-Verlag Berlin Heidelberg.

Callaghan, T.V., Johansson, M., Anisimov, O., Christiansen, H.H. , Instanes, A., Romanovsky, V., and Smith, S. (2011). Chapter 5: Changing Permafrost and its Impacts. In AMAP, *Snow, Water, Ice and Permafrost in the Arctic (SWIPA): Climate Change and the Cryosphere*, Arctic Monitoring and Assessment Programme (AMAP): Oslo, Norway.

Chang, X., Jin, H., Zhang, Y., He, R., Luo, D., Wang, Y., Lü, L., and Zhang, W. (2015). Thermal Impacts of Boreal Forest Vegetation on Active Layer and Permafrost Soils in Northern da Xing'Anling (Hinggan) Mountains, Northeast China. *Arctic, Antarctic, and Alpine Research, 47*(2), 267-279. doi: 10.1657/AAAR00C-14-016

Clark, I.D., Lauriol, B., Marschner, M., Sabourin, N., Chauret, Y., and Desrochers, A. (2004). Endostromatolites from permafrost karst, Yukon, Canada: paleoclimatic proxies for the Holocene hypsithermal. *Canadian Journal for Earth Sciences, 41*(4), 387-399. doi: 10.1139/e04-014

Collins, M., R. Knutti, J. Arblaster, J.-L. Dufresne, T. Fichefet, P. Friedlingstein, X. Gao, W.J. Gutowski, T. Johns, G. Krinner, M. Shongwe, C. Tebaldi, A.J. Weaver and M. Wehner (2013). *Long-term Climate Change: Projections, Commitments and Irreversibility*, In: STOCKER, T.F., D. Qin, G.-K. Plattner, M. Tignor, S.K. Allen, J. Boschung, A. Nauels, Y. Xia, V. Bex and P.M. Midgley (eds.), *Climate Change 2013: The Physical Science Basis*, Contribution of Working Group I to the Fifth Assessment Report of the Intergovernmental Panel on Climate Change, Cambridge University Press: Cambridge, United Kingdom and New York, NY, USA, pp. 1029-1136.

Couture, R., Smith, S., Robinson, S.D., Burgess, M.M., Solomon, S.(2003). On the hazards to infrastructure in the Canadian North associated with thawing of permafrost. In *Proceedings of Geohazards 2003, Third Canadian Conference on Geotechnique and Natural Hazards* (pp. 97–104), Edmonton, AB: The Canadian Geotechnical Society.

Craig, H. (1961). Isotopic variations in meteoric waters. *Science, 133*, 1702–1703.

Crann, C., Murseli, S., St-Jean, G., Zhao, X., Clark, I., & Kieser, W. (2016). First Status Report on Radiocarbon Sample Preparation Techniques at the A.E. Lalonde AMS Laboratory (Ottawa, Canada). *Radiocarbon, 1*(10). doi:10.1017/RDC.2016.55

Dansgaard, W. (1964). Stable isotopes in precipitations. *Tellus, 16*(4), 436-468. doi:10.1111/j.2153-3490.1964.tb00181.x

Delorme, L.D., Zoltai, S.C., and Kalas, L.L. (1977). Freshwater shelled invertebrate indicators of paleoclimate in northwestern Canada during late glacial time. *Canadian Journal of Earth Sciences, 14*(9), 2029-2046. doi:10.1139/e77-174

Duk-Rodkin, A. and Hughes, O.L. (1992). *Map 1745A: Surficial Geology: Fort McPherson – Bell River, Yukon - Northwest Territories* [cartographic material]. 1:250 000. Ottawa: Geological Survey of Canada.

Dyke, A.S. (2005). Late Quaternary Vegetaiton History of Northern North America Based on Pollen, Macrofossil, and Faunal Remains. *Géographie physique et Quaternaire, 59*(2-3), 211-262. doi: 10.7202/014755ar

Ferrier, K.L., Huppert, K.L., and Perron, J.T. (2013). Climatic control of bedrock river incision. Nature, 496(7444), 206-209. doi: 10.1038/nature111982

Fisher, J.P., Estop-Argonés, C., Thierry, A., Charman, D.J., Wolfe, S.A., Hartley, I.P., Murton, J.B., Williams, M., and Pheonix, G.K. (2016). The influence of vegetation and soil characteristics on active-layer thickness of permafrost soils in boreal forest. *Global Change Biology*, *22*, 3127–3140. doi: 10.1111/gcb.13248

French, H.M. (1974). Active Thermokarst Processes, Eastern Banks Island, Western Canadian Arctic. *Canadian Journal of Earth Sciences, 11*(6), 785-794. doi : 10.1139/e74-078

French, H.M. (1996). *The Periglacial Environment* (2nd edition). London, England: Addison Wesley Longman Limited.

French, H.M. and Harry, D.G. (1988). Nature and origin of ground ice, Sandhills Moraine, southwest Banks Island, Western Canadian Arctic. *Journal of Quaternary Science, 3*(1), 19-30. doi: 10.1002/jqs.3390030105

French, H.M. and Harry, D.G. (1990). Observations on buried glacier ice and massive segregated ice, western arctic coast, Canada. *Permafrost and Periglacial Processes, 1*(1), 31-43. doi: 10.1002/ppp.3430010105

Fritz, M., Wetterich, S., Schirrmeister, L., Meyer, H., Lantuit, H., Preusser, F., and Pollard, W.H. (2012). Eastern Beringia and beyond: Late Wisconsinian and Holocene landscape dynamics along the Yukon Coastal Plain, Canada. *Palaeogeography, Palaeoclimatology, Palaeoecology, 319-20,* 28-45. doi:10.1016/j.palaeo.2011.12.015

Fritz, M., Wolter, J., Rudaya, N., Palagushkina, O., Nazarova, L., Obu, J., Rethemeyer, J., Lantuit, H., and Wetterich, S. (2016). Holocene ice-wedge polygon development in northern Yukon permafrost. *Quaternary Science Reviews, 147,* p. 279-297. doi: 10.1016/j.quascirev.2016.02.008

Froese, D.G., Westgate, J.A., Reyes, A.V., Enkin, R.J, and Preece, S.J. (2008). Ancient Permafrost and a Future, Warmer Arctic. *Science, 321*(5896), 1648-1648. doi:10.1126/science.1157525

Fukuda, M. (1994). Methane flux from thawing Siberian permafrost (ice complexes) results from field observations. *Eos, Transactions, American Geophysical Union, 75*, 86.

Genxu, W., Guangsheng, L., Chunjie, L., and Yan, Y. (2012). The variability of soil thermal and hydrological dynamics with vegetation cover in a permafrost region. *Agricultural and Forest Meteorology, 162-163,* 44-57. doi: 10.1016/j.agrformet.2012.04.006

Harris, C. and Murton, J.B. 2005. Interactions between glaciers and permafrost: an introduction. In Harris, C. and Murton, J.B. (eds). *Cryospheric Systems: Glaciers and Permafrost*. Geological Society, London, Special Publications, *242*, 1-9. doi: 10.1144/GSL.SP.2005.242.01.01

Harry, D. G. (1986). Ground Ice. In FRENCH, Hugh M., Focus: Permafrost geomorphology (362-363), *The Canadian Geographer - Le Geographe Canadien, 30*(4).

Heiri, O., Lotter, A.F., Lemcke, G. (2001). Loss on ignition as a method for estimating organic and carbonate content in sediments: reproducibility and comparability of results. *Journal of Paleolimnology, 25*, 101-110.

Hubbard, B. and Sharp, M.J. (1989). Basal ice formation and deformation: a review. *Progress in Physical Geography, 13*(4), 529–558. doi: 10.1177/030913338901300403

Hubbard, B. and Sharp, M.J. (1995). Basal ice facies and their formation in the Western Alpes. Arctic and Alpine Research, 27(4), 301-310.

Hughes, O.L., Hodgson, D.A. and Pilon, J. (1972). *Surficial geology, Fort Good Hope, Arctic Red River, Fort McPherson, District of Mackenzie* [cartographic material]. 1:125,000. Ottawa: Geological Survey of Canada.

IPCC. (2013). *Climate Change 2013: The Physical Science Basis, Contribution of Working Group I to the Fifth Assessment Report of the Intergovernmental Panel on Climate Change* [Stocker, T.F., D. Qin, G.-K. Plattner, M. Tignor, S.K. Allen, J. Boschung, A. Nauels, Y. Xia, V. Bex and P.M. Midgley (Eds.)]. Cambridge University Press, Cambridge, United Kingdom and New York, NY, USA.

Kaufman, D.S., Ager, T.A., Anderson, N.J., Anderson, P.M., Andrews, J.T., Bartlein, P.J., Brubaker, L.B., Coats, L.L., Cwynar, L.C., Duvall, M.L., Dyke, A.S., Edwards, M.E., Eisner, W.R., Gajewski, K., Geirsdottir, A., Hu, F.S., Jennings, A.E., Kaplan, M.R., Kerwin, M.W., Lozhkin, A.V., MacDonald, G.M., Miller, G.H., Mock, C.J., Oswald, W.W., Otto-Bliesner, B.L., Porinchu, D.F., Rühland, K., Smol, J.P., Steig, E.J., Wolfe,

B.B. (2004). Holocene Thermal Maximum in the western Arctic (0-180°W). *Quaternary Science Reviews, 23*(5), 529-560. doi:10.1016/j.quascirev.2003.09.007

Kaufman, D.S., Axford, Y. L., Henderson, A. C. G., McKay, N. P., Oswald, W.W., Saenger, C., Anderson, R. S., Bailey, H. L., Clegg, B., Gajewski, K., Hu, F. S., Jones, M. C., Massa, C., Routson, C. C., Werner, A., Wooller, M. J., and Yu, Z. (2016). Holocene climate changes in eastern Berginia (NW North America) – A systematic review of multi-proxy evidence. *Quaternary Science Reviews, 147*, 312-339. doi: 10.1016/j.quascirev.2015.10.021

Kokelj S.V., Lantz, T.C., Tunnicliffe, J., Segal, R. and Lacelle, D. (2017). Climate-driven thaw of permafrost preserved glacial landscapes, northwestern Canada. *Geology, 45*(4), 371-374. doi: 10.1130/G38626.1v.

Kokelj, S.V., Tunnicliffe, J., Lacelle, D., Lantz, T.C., Chin, K.S. and Fraser, R. (2015). Increased precipitation drives mega slump development and destabilization of ice-rich permafrost terrain, northwestern Canada. *Global and Planetary Change, 129*, 56-68. doi: 10.1016/j.gloplacha.2015.02.008.

Kokelj, S.V., Riseborough, D., Coutts, R., and Kanigan, J.C.N. (2010). Permafrost and terrain conditions at northern drilling-mud sumps: Impacts of vegetation and climate change and the management implications. *Cold Regions Science and Technology, 64*(1), 46-56. doi: 10.1016/j.coldregions.2010.04.009

Kokelj, S.V., Smith, C.A.S., and Burn, C.R. (2002). Physical and Chemical Characteristics of the Active Layer and Permafrost, Herschel Island, Western Arctic Coast, Canada, *Permafrost and Periglacial Processes, 13*(2), 171-185. doi:10.1002/ppp.417

Kokelj, S.V., Zajdlik, B. and Thompson, M.S. (2009). The Impacts of Thawing Permafrost on the Chemistry of Lakes across the Subarctic Boreal-Tundra Transition, Mackenzie Delta Region, Canada. *Permafrost and Periglacial Processes, 20*(2), 185–199. doi: 10.1002/ppp.641

Knight, P.G. (1997). The basal ice layer of glaciers and ice sheets. *Quaternary Science Reviews, 16*(9), 975–993. doi: 10.1016/S0277-3791(97)00033-4

Lacelle, D. (2011). On the $\delta^{18}O$, δD and D-excess Relations in Meteoric Precipitation and During Equilibrium Freezing: Theoretical Approach and Field Example. *Permafrost And Periglacial Processes, 22*(1), 13–25. doi: 10.1002/ppp.712

Lacelle, D., Bjornson, J. and Lauriol, B. (2010). Climatic and geomorphic factors affecting contemporary (1950–2004) activity of retrogressive thaw slumps on the Aklavik Plateau, Richardson Mountains, NWT, Canada. *Permafrost And Periglacial Processes, 21*(1), 1–15. doi: 10.1002/ppp.666

Lacelle, D., Brooker, A., Fraser, R.H., Kokelj, S.V. (2015). Distribution and growth of thaw slumps in the Richardson Mountains-Peel Plateau region, northwestern Canada. *Geomorphology, 235*, 40-51. doi: 10.1016/j.geomorph.2015.01.024

Lacelle, D., Fontaine, M., Forest, A. P., Kokelj, S. (2014). High-resolution stable water isotopes as tracers of thaw unconformities in permafrost: A case study from western Arctic Canada, *Chemical Geology, 368*, 85-96. doi: 10.1016/j.chemgeo.2014.01.005

Lacelle, D.. Juneau, V., Pellerin, A., Lauriol, B., Clark, I. D. (2008). Weathering regime and geochemical conditions in a polar desert environment, Haughton impact structure region, Devon Island, Canada. *Canadian Journal of Earth Sciences, 45*(10), 1139-1157. doi:10.1139/E08-063

Lacelle, D, Lauriol, B.,Zazula, G., Ghaleb, B., Utting, N, & Clark, I. D. (2013). Timing of advance and basal condition of the Laurentide Ice Sheet during the last glacial maximum in the Richardson Mountains, NWT. *Quaternary Research, 80*(2), 274-283, doi:10.1016/j.yqres.2013.06.001

Lachenbruch, A. H., and Marshall, B.V. (1986). Changing climate: geothermal evidence from permafrost in the Alaskan Arctic. *Science, 234*(4777), 689–696. doi:10.1126/science.234.4777.689

Lang, S., McIntyre, C., Bernasconi, S., Früh-Green, G., Voss, B., Eglinton, T., & Wacker, L. (2016). Rapid ^{14}C Analysis of Dissolved Organic Carbon in Non-Saline Waters. *Radiocarbon, 58*(3), 505-515. doi:10.1017/RDC.2016.17

Lantz, T.C. and Kokelj, S.V. (2008). Increasing rates of retrogressive thaw slump activity in the Mackenzie Delta region, N.W.T., Canada. *Geophysical Research Letters, 35*(6), L06502. doi: 10.1029/2007GL032433

Lewkowicz, A.G. (1986). Rate of short-term ablation of exposed ground ice, Banks Island, Northwest Territories, Canada. *Journal of Glaciology, 32*(112), 511–519. doi: 10.1017/S0022143000012223

Lewkowicz, A.G. (1987). Headwall retreat of ground-ice slumps, Banks Island, Northwest Territories. *Canadian Journal of Earth Sciences, 24*(6), 1077-1085. doi: 10.1139/e87-105

Lewkowicz, A.G. and Harris, C. (2005). Morphology and geotechnique of active-layer detachment failures in discontinuous and continuous permafrost, northern Canada. *Geomorphology, 69*(1-4), 275-297. doi: 10.1016/j.geomorph.2005.01.011

Lis, G., Wassenaar, L.I., and Hendry, M.J. (2008). High-Precision Laser Spectroscopy D/H and $^{18}O/^{16}O$ Measurements of Microliter Natural Water Samples. *Analytical Chemistry,80*(1), 287-293. doi:10.1021/ac701716q

Mackay, J.R. (1995). Active layer changes (1968 to 1993) following the forest - tundra fire near Inuvik, N.W.T., Canada. *Arctic and Alpine Research, 27*(4), 323-336. doi:10.2307/1552025

Mackay, J.R. (1992). Lake stability in an ice-rich permafrost environment: examples from the western Arctic coast. In Robarts, R. D. and Bothwell, M. L. (Eds.). *Aquatic Ecosystems in Semi-Arid Regions: Implications for Resource Management,* N.H. R.I. Symposium Series 7, Environment Canada: Saskatoon, 1-26.

Mackay, J.R. (1981). Active layer slope movement in a continuous permafrost environment, Garry Island, Northwest Territories, Canada. *Canadian Journal of Earth Sciences, 18*(11), 1666-1680. doi: 10.1139/e81-154

Mackay, J.R. (1983). Oxygen isotope variations in permafrost, Tuktoyaktuk Peninsula area, Northwest Territories. In *Current Research, Part B*, Geological Survey of Canada, Paper 83- *IB,* 67-74.

Mackay, J.R. (1978). Freshwater shelled invertebrate indicators of paleoclimate in northwestern Canada during late glacial times: Discussion. *Canadian Journal of Earth Sciences, 15*(3), 461-462. doi: 10.1139/e78-052

Menviel, L., Timmermann, A., Elison Timm, O. and Mouchet, A. (2011). Deconstructing the Last Glacial Termination: the role of millennial and orbital-scale forcings. *Quaternary Science Reviews, 30*(9-10), 1155-1172. doi: 10.1016/j.quascirev.2011.02.005

Moorman, B.J. and Michel, F.A. (2000). The Burial of Ice in the Proglacial Environment on Bylot Island\ Arctic Canada. *Permafrost Periglacial Processes, 11*(3), 161-175. doi: 10.1002/1099-1530(200007/09)11:3<161::AID-PPP347>3.0.CO;2-F

Murton, J.B. (2001). Thermokarst sediments and sedimentary structures, Tukotoyaktuk Coastlands, western Arctic Canada. *Global and Planetary Change, 28*(1-4), 175-192. doi: 10.1016/S0921-8181(00)00072-2

Murton, J.B. and French, H.M. (1993). Thermokarst Involutions, Summer Island, Pleistocene Mackenzie Delta, Western Canadian Arctic. *Permafrost and Periglacial Processes, 4*(3), 217-229. doi: 10.1002/ppp.3430040304

Murton, J.B. and French, H.M. (1994). Cryostructures in permafrost, Tuktoyaktuk coastlands, western arctic Canada. *Canadian Journal of Earth Sciences, 31*(4), 737-747. doi:10.1139/e94-067

Murton, J.B., Whiteman, C.A. and Allen, P. (1995). Involutions in the Middle Pleistocene (Anglian) Barham Soil, eastern England: a comparison with thermokarst involutions from arctic Canada. *Boreas, 24*(3), 269-280. doi: 10.1111/j.1502-3885.1995.tb00779.x

Nelson, F.E. (2003). Geocryology: (Un)frozen in time. *Science, 299*(5613), 1673–1675.

Nelson, F.E. and Hinkel, K.M. (2004). Methods for measuring active-layer thickness. In Humlum, O., and Matsuoka, N (Eds.), *A handbook on periglacial field methods* (10-20). International Permafrost Association (IPA), The Working Group on Periglacial Processes and Environments.

Norris, D.K. (1985). Eastern Cordilleran Foldbelt of northern Canada; its structural geometry and hydrocarbon potential. *AAPG Bulletin, 69*(5), 788-808. doi: 10.1306/AD462812-16F7-11D7-8645000102C1865D

O'Neill, H.B., Burn, C.R., Kokelj, S.V. and Lantz, T.C. (2015). "Warm" tundra: atmospheric and near-surface ground temperature inversions across an alpine treeline in continuous permafrost, western Arctic, Canada. *Permafrost and Periglacial Processes, 26*(2), 103-118. doi: 10.1002/ppp.1838

Osterkamp, T.E., Viereck, L., Shur, Y., Jorgenson, M.Y., Racine, C., Doyle, A., and Boone, R.D. (2000). Observations of thermokarst and its impact on boreal forests in Alaska. *U.S.A. Arctic, Antarctic and Alpine Research, 32*(3), 303–315. doi:10.2307/1552529

Palmer, M.J., Burn, C.R., Kokelj, S.V. (2012). Factors influencing permafrost temperatures across tree line in the uplands east of the Mackenzie Delta, 2004–2010. *Canadian Journal of Earth Sciences, 49*(8), 877–894. doi: 10.1139/e2012-002.

Palstra, S., & Meijer, H. (2014). Biogenic carbon fraction of biogas and natural gas fuel mixtures determined with ^{14}C. *Radiocarbon, 56*(1), 7-28. doi:10.2458/56.16514

Phillips, R.T.J. and Robert, A. (2005). River incision in relation to post-glacial events in the Humber River Basin, Ontario. *Géographie physique et Quaternaire, 591*, 17–30. doi: 10.7202/013734ar

Pomeroy, J.W., Marsh, P., Jones, H.G., and Davies, T.D. (1995). Spatial distribution of snow chemical load at the tundra-taiga transition, In *Biogeochemistry of Seasonality Snow-Covered Catchments*, Tonnessen, K. A., Williams, M.W., and Tranter, M. (eds.). International Association of Hydrological Sciences, No. 228, IAHS Press: Wallingford, 191-203.

Pollard, W.H. (1991). Observations On Massive Ground Ice On Fosheim Peninsula, Ellesmere Island, Northwest Territories. *Current Research, Part E/Recherches En Cours, Partie E; by Geological Survey of Canada; Geological Survey of Canada, Paper no. 91-1E*, 223-231. doi: 10.4095/132647.

Pollard, W.H. (2000). Ground ice aggradation on Fosheim Peninsula, Ellesmere Island, Nunavut. *Geological Survey of Canada Bulletin 529*, 325-333.

Pollard, W.H. and Bell, T. (1998). Massive ice formation in the Eureka Sound Lowlands: a landscape model. Lewkowicz, A. G. and Allard, M. (Eds.) In: *Proceedings, Seventh*

International Permafrost Conference, Yellowknife, Université Laval, Centre d'etudes nordiques, Collection Nordicana. No. 57, 903-908.

Rampton, V. N. (1982). Quaternary geology of the Yukon Coastal Plain, Canada. *Geological Survey of Canada*, Bulletin 317. doi: 10.4095/126937

Reimer, P.J., Bard, E., Bayliss, A., Beck, J.W., Blackwell, P.G., Bronk Ramsey, C., Buck, C.E., Cheng, H., Edwards, R.L., Friedrich, M., Grootes, P.M., Guilderson, T.P., Haflidason, H., Hajdas, I., Hatté, C., Heaton, T.J., Hogg, A.G., Hughen, K.A., Kaiser, K.F., Kromer, B., Manning, S.W., Niu, M., Reimer, R.W., Richards, D.A., Scott, E.M., Southon, J.R., Turney, C.S.M. and van der Plicht, J. (2013). IntCal13 and MARINE13 radiocarbon age calibration curves 0-50000 years calBP. *Radiocarbon 55*(4), 1869–1887.

Riseborough, D.W. (1990). Soil latent heat as a filter of the climate signal in permafrost. In *Proceedings of the Fifth Canadian Permafrost Conference* (199–205), Université Laval, Quebec, Collection Nordicana, 54.

Ritchie, J. C. (1984). *Past and present vegetation of the Far Northwest of Canada*. Toronto, Ontario, Canada: University of Toronto Press.

Ritchie, J. C. and Hare, F.K. (1971). Late-Quaternary Vegetation and Climate Near the Arctic Tree Line of Northwestern North America. *Quaternary Research, 1*(3), 331-342. doi: 10.1016/0033-5894(71)90069-X

Robinson, S.D. (2000). Thaw-slump-derived thermokarst near Hot Weather Creek, Ellesmere Island, Nunavut. *Bulletin of the Geological Survey of Canada*. 335-345.

Robinson, S.D. and Pollard W.H. (1998). Massive ground ice within Eureka Sound Bedrock, Ellesmere Island, Canada. In *Proceedings of Seventh International Conference on Permfafrost, Yellowknife, Canada,* Collection Nordica, 55, 949-954.

Roy-Léveillé, P., Burn, C.R. and McDonald, I.D. (2014). Vegetation-Permafrost Relations within the Forest-Tundra Ecotone near Old Crow, Northern Yukon, Canada. *Permafrost and Periglacial Processes, 25*(2), 127-135. doi: 10.1002/ppp.1805

Ruddiman, W.F. (2008). *Earth's Climate: Past and Future*. New York, United States of America: Basingstoke, England: W.H. Freeman and Company.

Schneider Von Deimling, T., Ganopolski, A. and Held, H. (2006). How Cold was the Last Glacial Maximum?. *Geophysical Research Letters*, *33*(14), L14709. doi:10.1029/2006GL026484

Serreze, M.C. and Barry, R.G. (2005). *The Arctic Climate System*. New York, United States of America: Cambridge University Press.

Smith, M.W. (1975). Microclimatic influences on ground temperatures and permafrost distribution, Mackenzie Delta, Northwest Territories. *Canadian Journal of Earth Sciences, 12*(8), 1421–1438. doi: 10.1139/e75-129

Smith, M.W. (1993). Climatic Change and Permafrost. In French, H.M. and Slaymaker, O. (eds.), *Canada's Cold Environments* (291-311). Montreal, Quebec, Canada: McGill University Press.

Smith, I.R. and Lesk-Winfield, K. (2012). *An updated assessment of ground ice and permafrost geology-related observations based on seismic shothole drillers' log records, Northwest Territories and northern Yukon*, Geological Survey of Canada, Open File 7061.

Sparrman, T., Oquist, M., Klemdtsson, L., Schleucher, J., and Nilsson, M. (2004). Quantifying unfrozen water in frozen soil by high- field 2H NMR. *Environmental Science & Technology, 38*(20), 5420–5425. doi: 10.1021/es0493695

St-Jean, G. (2003). Automated quantitative and isotopic (^{13}C) analysis of dissolved inorganic carbon and dissolved organic carbon in continuous-flow using a total organic carbon analyser. *Rapid Communications in Mass Spectrometry, 17*(5), 419-428. doi: 10.1002/rcm.926

St-Jean, G., Kieser, W., Crann, C., & Murseli, S. (2016). Semi-Automated Equipment for CO_2 Purification and Graphitization at the A.E. Lalonde AMS Laboratory (Ottawa, Canada). *Radiocarbon, 1*(16). doi: 10.1017/RDC.2016.57

Tarasov, L. and Peltier, W.R. (2007) The co-evolution of continental ice cover and permafrost extent over the last glacial-interglacial cycle in North America. *Journal of Geophysical Research, 112*, F02S08. doi: 10.1029/2006JF000661

Thompson C., Beringer, J., Chapin, F.S. III, McGuire, A.D. (2004). Structural complexity and land-surface energy exchange along a gradient from arctic tundra to boreal forest. *Journal of Vegetation Science, 15*(3), 397–406. doi: 10.1111/j.1654-1103.2004.tb02277.x

van Everdingen, R. O. (ed.). (1998). *Multi-language Glossary of Permafrost and Related Ground-ice Terms*. Calgary, AB, Canada: International Permafrost Association, Terminology Working Group.

van Reeuwijk, L.P. (Ed.). (2002). *Procedures for soil analysis* (6th ed.). The Netherlands: International Soil Reference and Information Centre.

Wahl, H.E., Fraser, D.B., Harvey, R.C. and Maxwell, J.B. (1987). *Climate of Yukon*, Climatological Studies No. 40. Environment Canada, Atmosphere Environment Service, Supply and Services Canada: Ottawa; 323 pp.

Waller, R.I., Murton, J.B. and Knight, P.G. (2009). Basal glacier ice and massive ground ice: different scientists, same science. *Geological Society, London, Special Publications,320,* 57-69. doi: 10.1144/SP320.5

Williams, P.J. and Smith, M.W (1989). *The frozen earth : fundamentals of geocryology*. Cambridge, New York, USA : Cambridge University Press.

Worsley, P. (2000). Late-Quaternary cryostratigraphy of a coastal cliff at Martha Point, southwest Banks Island, western Canadian Arctic. *The Holocene, 10*(3), 395-400.

Zazula, G.D., Mackay, G., Andrews, T.D., Shapiro, B., Letts, B. and Brock. (2009). A late Pleistocene steppe bison (Bison priscus) partial carcass from Tsiigehtchic, Northwest Territories, Canada. *Quaternary Science Reviews, 28*(25), 2734-2742. doi: 10.1016/j.quascirev.2009.06.012

Zhou, Y., Guo, H., Lu, H., Mao, R., Zheng, H. and Wang, J. (2015). Analytical methods and application of stable isotopes in dissolved organic carbon and inorganic carbon in groundwater. *Rapid Communications in Mass Spectrometry, 29*(19), 1827-1835. doi: 10.1002/rcm.7280

APPENDIX A: LABORATORY ANALYSES RESULTS

Table A1 Major cations measurements results

		Concentration (ppm)				
Sample ID	Sample Unit	Ca^{2+}	Fe^{+}	K^{+}	Mg^{2+}	Na^{+}
RS1-16-16+17+18+19	RTL	127.34	0.02	6.37	25.81	8.77
RS2-16-MI-1	Unit 1	11.55	0.02	0.47	1.96	1.87
RS2-16-MI-2	Unit 1	14.15	0.02	0.39	1.56	2.17
RS2-16-MI-3	Unit 1	21.98	0.02	0.42	1.79	1.83
RS2-16-MI-4	Unit 1	10.63	0.00	0.59	1.35	2.03
RS2-16-MI-5	Unit 1	25.87	0.00	0.83	2.62	2.45
RS2-16-MI-7	Unit 1	17.08	0.00	1.87	2.58	2.96
RS2-16-MI-8	Unit 1	17.50	0.02	0.62	1.59	1.96
RS2-16-MI-9	Unit 1	19.67	0.02	0.55	3.00	2.38
RS2-16-MI-10	Unit 1	14.58	0.00	4.60	2.49	2.75
RS2-16-MI-11	Unit 1	21.57	0.00	3.75	2.83	2.36
RS2-16-MI-12	Unit 1	20.96	0.00	0.97	3.42	3.23
RS2-16-MI-13	Unit 1	21.59	0.03	0.75	4.68	3.69
RS2-16-MI-14	Unit 1	9.54	0.02	0.26	1.90	1.89
RS2-16-MI-15	Unit 1	22.74	0.12	3.67	4.44	4.42
RS2-16-MI-16	Unit 1	22.08	0.19	1.25	6.93	7.28
RS2-16-MI-17	Unit 1	16.82	0.07	1.11	3.75	2.92
RS2-16-MI-18	Unit 1	13.26	0.07	0.47	2.18	1.92
RS2-16-MI-26	Unit 2	39.87	0.02	1.34	3.70	2.75
RS2-16-MI-28	Unit 2	23.39	0.02	2.47	6.19	4.81
RS2-16-MI-29	Unit 2	46.97	0.07	3.12	8.51	7.24
RS2-16-MI-31	Unit 2	141.70	0.00	7.93	30.52	16.62
RS2-16-MI-32	Unit 2	272.96	0.00	13.01	59.68	29.20
RS2-16-MI-33	Unit 2	253.73	0.00	11.12	51.58	22.19
RS2-16-MI-34	Unit 2	302.99	0.00	12.39	80.60	43.90
RS2-16-MI-35	Unit 2	83.90	0.00	5.18	19.94	11.31
RS2-16-MI-36	Unit 3	3.79	0.04	0.15	1.27	0.94
RS2-16-MI-37	Unit 3	3.65	0.07	0.20	1.04	0.86
RS2-16-MI-38	Unit 3	3.68	0.03	0.78	1.21	1.39
RS2-16-MI-39	Unit 3	8.46	0.00	0.60	2.24	1.05
RS2-16-MI-40	Unit 3	7.26	0.05	1.26	1.93	1.95
RS2-16-MI-41	Unit 3	3.67	0.06	0.51	1.15	1.06
RS2-16-MI-42	Unit 3	5.06	0.01	0.42	1.76	1.21
RS2-16-MI-43	Unit 3	3.92	0.08	0.38	1.20	1.15

RS2-16-MI-44	Unit 3	3.03	0.06	0.75	0.91	1.39
RS2-16-MI-45	Unit 3	3.36	0.09	0.35	1.02	1.14
RS2-16-MI-46	Unit 3	2.92	0.00	0.58	0.89	0.99
RS2-16-MI-47	Unit 3	2.33	0.01	0.34	0.62	1.05
RS2-16-MI-48	Unit 3	3.07	0.03	0.42	0.96	1.27
RS2-16-MI-49	Unit 3	3.69	0.03	0.69	1.22	1.09
RS2-16-MI-51	Unit 4	6.99	0.00	0.21	1.60	1.14
RS2-16-MI-53	Unit 4	8.71	0.38	1.41	2.63	1.18
RS2-16-MI-54	Unit 4	8.53	0.08	0.25	2.82	0.92
RS2-16-MI-55	Unit 4	10.62	0.13	0.52	2.59	2.88
RS2-16-MI-56	Unit 4	4.92	0.11	3.08	1.56	1.16
RS2-16-MI-57	Unit 4	4.30	0.04	6.60	1.24	1.33
RS2-16-MI-59	Unit 4	3.84	0.06	0.36	1.19	0.97
RS2-16-MI-60	Unit 4	3.60	0.26	0.27	1.21	1.00
RS2-16-MI-61	Unit 4	5.56	0.00	0.07	1.97	0.50
RS2-16-MI-62	Unit 4	4.67	0.16	1.09	1.45	1.57
RS2-16-MI-63	Unit 4	7.41	0.08	2.98	1.95	1.84
RS2-16-MI-64	Unit 4	14.65	0.22	0.77	3.75	3.70

Table A2 Major anions measurements results

		Concentration (ppm)		
Sample ID	Sample Unit	Cl^-	SO^{4-}	NO^{3-}
RS1-16-16+17+18+19	RTL	1.96	205.29	5.47
RS2-16-MI-1	Unit 1	1.08	18.35	0.21
RS2-16-MI-2	Unit 1	1.39	17.18	0.19
RS2-16-MI-3	Unit 1	1.10	9.36	0.09
RS2-16-MI-4	Unit 1	1.66	11.44	0.15
RS2-16-MI-5	Unit 1	1.45	42.22	0.04
RS2-16-MI-7	Unit 1	2.64	23.71	0.19
RS2-16-MI-8	Unit 1	1.62	14.56	0.04
RS2-16-MI-9	Unit 1	1.10	27.84	0.02
RS2-16-MI-10	Unit 1	5.14	27.27	0.13
RS2-16-MI-11	Unit 1	4.29	29.82	0.13
RS2-16-MI-12	Unit 1	1.74	33.23	0.23
RS2-16-MI-13	Unit 1	1.47	34.54	0.20
RS2-16-MI-14	Unit 1	1.14	15.80	0.15
RS2-16-MI-15	Unit 1	4.53	34.95	0.01
RS2-16-MI-16	Unit 1	8.28	25.39	0.80
RS2-16-MI-17	Unit 1	1.96	21.52	0.02
RS2-16-MI-18	Unit 1	1.17	17.63	0.01
RS2-16-MI-26	Unit 2	1.79	42.09	0.02
RS2-16-MI-28	Unit 2	1.88	34.33	0.17
RS2-16-MI-29	Unit 2	3.40	60.90	3.69
RS2-16-MI-31	Unit 2	0.56	452.54	0.03
RS2-16-MI-32	Unit 2	0.65	988.20	2.77
RS2-16-MI-33	Unit 2	0.62	864.88	0.79
RS2-16-MI-34	Unit 2	1.67	1791.80	0.40
RS2-16-MI-35	Unit 2	7.85	215.21	2.77
RS2-16-MI-36	Unit 3	0.40	1.05	0.27
RS2-16-MI-37	Unit 3	0.48	1.27	0.28
RS2-16-MI-38	Unit 3	1.27	0.95	0.28
RS2-16-MI-39	Unit 3	0.63	1.95	0.18
RS2-16-MI-40	Unit 3	1.74	1.82	0.31
RS2-16-MI-41	Unit 3	0.84	0.88	0.29
RS2-16-MI-42	Unit 3	0.74	1.49	0.33
RS2-16-MI-43	Unit 3	0.81	0.92	0.27
RS2-16-MI-44	Unit 3	1.34	0.74	0.02
RS2-16-MI-45	Unit 3	0.63	0.83	0.26

RS2-16-MI-46	Unit 3	1.03	0.79	0.13
RS2-16-MI-47	Unit 3	0.84	0.67	0.01
RS2-16-MI-48	Unit 3	0.95	1.06	0.23
RS2-16-MI-49	Unit 3	1.06	0.89	0.01
RS2-16-MI-51	Unit 4	0.71	3.97	0.18
RS2-16-MI-53	Unit 4	1.54	2.06	0.00
RS2-16-MI-54	Unit 4	0.59	1.69	0.01
RS2-16-MI-55	Unit 4	1.53	5.33	0.03
RS2-16-MI-56	Unit 4	3.08	1.35	0.16
RS2-16-MI-57	Unit 4	6.23	2.08	0.24
RS2-16-MI-59	Unit 4	0.77	0.77	0.24
RS2-16-MI-60	Unit 4	0.66	0.94	0.01
RS2-16-MI-61	Unit 4	0.35	1.22	0.03
RS2-16-MI-62	Unit 4	1.59	2.22	0.05
RS2-16-MI-63	Unit 4	3.38	5.61	0.02
RS2-16-MI-64	Unit 4	1.33	20.44	0.04

Note: Grayed values are below LOD

Table A3 Dissolved organic carbon (DOC) and $\delta^{13}C$ measurements results

Lab ID	Sample ID	Sample Unit	DOC (ppm)	$\delta^{13}C_{DOC}$ (‰)
C-111354	RS1-16-16+17+18+19	RTL	30.15	-26.33
C-111355	RS2-16-MI-1+2	Unit 1	4.53	-28.19
C-111356	RS2-16-MI-3+4	Unit 1	4.3	-28.61
C-111357	RS2-16-MI-5	Unit 1	1.83	-28.24
C-111358	RS2-16-MI-7	Unit 1	3.72	-27.03
C-111359	RS2-16-MI-8+9	Unit 1	4.15	-29.36
C-111360	RS2-16-MI-10	Unit 1	2.67	-28.57
C-111361	RS2-16-MI-11	Unit 1	3.16	-27.1
C-111362	RS2-16-MI-12	Unit 1	3.23	-27.85
C-111363	RS2-16-MI-13+14	Unit 1	4.2	-28.4
C-111364	RS2-16-MI-15	Unit 1	4.82	-28.64
C-111365	RS2-16-MI-16	Unit 1	4.38	-28.79
C-111366	RS2-16-MI-17+18	Unit 1	6.16	-27.79
C-111367	RS2-16-MI-26	Unit 2	4.37	-29.82
C-111368	RS2-16-MI-27+28+29	Unit 2	8.4	-27.82
C-111369	RS2-16-MI-31+32	Unit 2	6.31	-26.98
C-111370	RS2-16-MI-33+34+35	Unit 2	5.51	-26.89
C-111371	RS2-16-MI-36	Unit 3	3.09	-28.1
C-111372	RS2-16-MI-37+38	Unit 3	3.14	-27.85
C-111373	RS2-16-MI-39+40	Unit 3	4.91	-27.86
C-111374	RS2-16-MI-41+42	Unit 3	4.21	-28.32
C-111375	RS2-16-MI-43+44	Unit 3	4.77	-28.97
C-111376	RS2-16-MI-45+46	Unit 3	4.33	-27.83
C-111377	RS2-16-MI-47	Unit 3	3.42	-29.48
C-111378	RS2-16-MI-48+49	Unit 3	3.83	-28.09
C-111379	RS2-16-MI-51	Unit 4	2.54	-27.82
C-111380	RS2-16-MI-53	Unit 4	3.92	-29.82
C-111381	RS2-16-MI-54	Unit 4	5.07	-28.55
C-111382	RS2-16-MI-56	Unit 4	4.1	-27.03
C-111383	RS2-16-MI-57	Unit 4	3.12	-27.65
C-111384	RS2-16-MI-59	Unit 4	3.32	-28.27
C-111385	RS2-16-MI-60	Unit 4	6.36	-28.45
C-111386	RS2-16-MI-61	Unit 4	1.84	-28.3
C-111387	RS2-16-MI-62	Unit 4	6.23	-28.12
C-111388	RS2-16-MI-63+64	Unit 4	5.75	-28.82

Table A4 Particle size analysis results

Sample ID	Sample Unit	Size (μm)								
		2,000	1,674	1,408	1,184	995.5	837.1	703.9	591.9	497.8
RS1_16_5	TL	0.00	0.00	0.00	0.00	0.00	0.00	0.00	0.00	0.00
RS1_16_6	TL	0.00	0.00	0.00	0.00	0.00	0.00	0.00	0.00	0.00
RS1_16_7	TL	0.00	0.00	0.00	0.00	0.00	0.00	0.00	0.00	0.00
RS1_16_8	TL	0.00	0.00	0.00	0.00	0.00	0.00	0.00	0.00	0.00
RS1_16_9	TL	0.00	0.00	0.00	0.00	0.00	0.00	0.00	0.00	0.00
RS1_16_10	TL	0.00	0.00	0.00	0.00	0.00	0.00	0.00	0.00	0.00
RS1_16_12	TL	0.00	0.00	0.00	0.00	0.00	0.00	0.00	0.00	0.10
RS1_16_15	RTL	0.00	0.00	0.00	0.00	0.00	0.00	0.00	0.00	0.00
RS1_16_16	RTL	0.00	0.00	0.00	0.00	0.00	0.00	0.00	0.00	0.00
RS1_16_20	RTL	0.00	0.00	0.00	0.00	0.00	0.00	0.00	0.00	0.00
RS1_16_19	RTL	0.00	0.00	0.00	0.00	0.00	0.00	0.00	0.00	0.00
RS1_16_21	RTL	0.00	0.00	0.00	0.00	0.00	0.00	0.00	0.00	0.00
RS1_16_18	RTL	0.00	0.00	0.00	0.00	0.00	0.00	0.00	0.00	0.00
RS1_16_14	RTL	0.00	0.00	0.00	0.00	0.00	0.00	0.00	0.00	0.00
RS1_16_17	RTL	0.00	0.00	0.00	0.00	0.00	0.00	0.00	0.00	0.00
RS1_16_13	RTL	0.00	0.00	0.00	0.00	0.00	0.00	0.00	0.00	0.00
RS2_16_MI_19	RTL	0.00	0.00	0.00	0.00	0.00	0.00	0.00	0.00	0.10
RS2_16_MI_20	RTL	0.00	0.00	0.00	0.00	0.00	0.00	0.00	0.00	0.00
RS2_16_MI_21	RTL	0.00	0.00	0.00	0.00	0.00	0.00	0.00	0.00	0.00
RS2_16_MI_22	RTL	0.00	0.00	0.00	0.00	0.00	0.00	0.00	0.00	0.35
RS2_16_MI_24	RTL	0.00	0.00	0.00	0.00	0.00	0.00	0.00	0.00	0.00
RS2_16_MI_25	RTL	0.00	0.00	0.00	0.00	0.00	0.00	0.00	0.00	0.11
RS2_16_MI_30	Unit 2	0.00	0.00	0.00	0.00	0.00	0.00	0.00	0.24	0.38
RS2_16_MI_31	Unit 2	0.00	0.00	0.00	0.00	0.00	0.00	0.00	0.10	0.23
RS2_16_MI_32	Unit 2	0.00	0.00	0.00	0.00	0.00	0.00	0.00	0.39	0.43
RS2_16_MI_33	Unit 2	0.00	0.00	0.00	0.00	0.00	0.00	0.00	0.35	0.39
RS2_16_MI_34	Unit 2	0.00	0.00	0.00	0.00	0.00	0.00	0.00	0.00	0.00
RS2_16_MI_35	Unit 2	0.00	0.00	0.00	0.00	0.00	0.00	0.00	0.00	0.00

Sample ID	Sample Unit	Size (µm)								
		418.6	352.0	296.0	248.9	209.3	176.0	148.0	124.4	104.6
RS1_16_5	TL	0.00	0.00	0.00	0.43	0.66	1.06	1.64	2.34	3.03
RS1_16_6	TL	0.00	0.00	0.00	0.38	0.57	0.92	1.47	2.19	2.92
RS1_16_7	TL	0.00	0.00	0.00	0.36	0.53	0.83	1.31	1.94	2.63
RS1_16_8	TL	0.00	0.00	0.00	0.44	0.69	1.14	1.83	2.70	3.57
RS1_16_9	TL	0.00	0.00	0.21	0.45	0.72	1.18	1.87	2.71	3.54
RS1_16_10	TL	0.00	0.00	0.33	0.49	0.77	1.26	1.95	2.67	3.27
RS1_16_12	TL	0.39	0.56	0.81	1.14	1.48	1.79	2.10	2.49	2.98
RS1_16_15	RTL	0.37	0.51	0.70	0.92	1.12	1.30	1.46	1.69	2.04
RS1_16_16	RTL	0.00	0.00	0.00	0.00	0.22	0.43	0.61	0.87	1.26
RS1_16_20	RTL	0.00	0.00	0.35	0.44	0.55	0.68	0.85	1.09	1.46
RS1_16_19	RTL	0.00	0.34	0.43	0.52	0.62	0.74	0.91	1.19	1.62
RS1_16_21	RTL	0.00	0.23	0.42	0.50	0.59	0.68	0.81	1.02	1.38
RS1_16_18	RTL	0.00	0.35	0.45	0.56	0.67	0.79	0.95	1.20	1.59
RS1_16_14	RTL	0.00	0.00	0.12	0.26	0.47	0.62	0.83	1.12	1.52
RS1_16_17	RTL	0.34	0.45	0.59	0.76	0.94	1.10	1.29	1.55	1.91
RS1_16_13	RTL	0.32	0.42	0.57	0.76	0.97	1.19	1.44	1.77	2.20
RS2_16_MI_19	RTL	0.41	0.57	0.78	1.01	1.21	1.35	1.50	1.70	2.03
RS2_16_MI_20	RTL	0.21	0.42	0.55	0.72	0.88	1.06	1.27	1.56	1.97
RS2_16_MI_21	RTL	0.39	0.53	0.73	0.97	1.18	1.35	1.51	1.75	2.09
RS2_16_MI_22	RTL	0.48	0.69	0.98	1.26	1.45	1.52	1.58	1.73	2.04
RS2_16_MI_24	RTL	0.21	0.42	0.56	0.72	0.90	1.09	1.32	1.64	2.12
RS2_16_MI_25	RTL	0.38	0.52	0.71	0.93	1.13	1.31	1.50	1.76	2.16
RS2_16_MI_30	Unit 2	0.53	0.76	1.05	1.28	1.32	1.22	1.08	0.99	0.98
RS2_16_MI_31	Unit 2	0.44	0.60	0.79	0.95	1.00	0.99	0.97	1.00	1.09
RS2_16_MI_32	Unit 2	0.63	0.94	1.32	1.61	1.65	1.47	1.27	1.16	1.17
RS2_16_MI_33	Unit 2	0.55	0.80	1.09	1.30	1.33	1.23	1.13	1.11	1.17
RS2_16_MI_34	Unit 2	0.00	0.24	0.42	0.50	0.55	0.60	0.66	0.76	0.93
RS2_16_MI_35	Unit 2	0.00	0.00	0.00	0.00	0.00	0.00	0.00	0.00	0.00

Sample ID	Sample Unit	Size (µm)								
		87.99	73.99	62.22	52.32	44.00	37.00	31.11	26.16	22.00
RS1_16_5	TL	3.67	4.27	4.84	5.34	5.68	5.75	5.77	5.71	5.44
RS1_16_6	TL	3.54	4.07	4.56	4.98	5.21	5.11	5.21	5.14	5.06
RS1_16_7	TL	3.31	3.97	4.63	5.21	5.62	5.72	5.69	5.72	5.56
RS1_16_8	TL	4.32	4.91	5.31	5.33	5.46	5.28	5.08	4.93	4.78
RS1_16_9	TL	4.26	4.81	5.15	5.24	5.19	5.26	5.22	5.15	4.98
RS1_16_10	TL	3.70	4.07	4.44	4.79	5.03	5.16	5.06	5.08	5.05
RS1_16_12	TL	3.51	3.99	4.32	4.48	4.54	4.50	4.57	4.44	4.48
RS1_16_15	RTL	2.54	3.17	3.82	4.37	4.70	4.64	4.81	4.75	4.64
RS1_16_16	RTL	1.84	2.64	3.66	4.74	5.60	6.02	5.89	5.82	5.46
RS1_16_20	RTL	2.01	2.77	3.70	4.65	5.40	5.79	5.65	5.63	5.30
RS1_16_19	RTL	2.24	3.05	3.94	4.69	5.15	5.14	5.27	5.14	4.97
RS1_16_21	RTL	1.91	2.61	3.43	4.24	4.88	5.25	5.15	5.23	5.02
RS1_16_18	RTL	2.14	2.85	3.62	4.32	4.80	5.02	4.90	4.98	4.79
RS1_16_14	RTL	2.10	2.87	3.82	4.77	5.51	5.71	5.82	5.50	5.09
RS1_16_17	RTL	2.41	3.04	3.73	4.39	4.89	5.08	5.01	5.00	4.77
RS1_16_13	RTL	2.73	3.34	3.93	4.45	4.82	4.94	4.87	4.89	4.69
RS2_16_MI_19	RTL	2.49	3.03	3.58	4.04	4.34	4.50	4.59	4.42	4.56
RS2_16_MI_20	RTL	2.53	3.20	3.91	4.49	4.84	4.78	4.94	4.80	4.66
RS2_16_MI_21	RTL	2.57	3.15	3.73	4.22	4.55	4.72	4.61	4.75	4.62
RS2_16_MI_22	RTL	2.51	3.10	3.69	4.16	4.43	4.31	4.50	4.39	4.29
RS2_16_MI_24	RTL	2.80	3.69	4.66	5.50	5.91	5.89	5.70	5.24	4.75
RS2_16_MI_25	RTL	2.70	3.34	3.98	4.49	4.79	4.71	4.87	4.80	4.63
RS2_16_MI_30	Unit 2	1.04	1.15	1.32	1.56	1.87	2.24	2.66	3.12	3.59
RS2_16_MI_31	Unit 2	1.23	1.41	1.62	1.85	2.11	2.39	2.71	3.06	3.43
RS2_16_MI_32	Unit 2	1.28	1.46	1.69	1.95	2.23	2.54	2.87	3.24	3.60
RS2_16_MI_33	Unit 2	1.30	1.44	1.61	1.81	2.05	2.35	2.70	3.09	3.49
RS2_16_MI_34	Unit 2	1.20	1.56	2.04	2.63	3.28	3.93	4.53	5.05	5.43
RS2_16_MI_35	Unit 2	0.33	0.38	0.45	0.56	0.72	0.94	1.25	1.65	2.13

Sample ID	Sample Unit	Size (µm)								
		18.50	15.55	13.08	11.00	9.25	7.78	6.54	5.50	4.62
RS1_16_5	TL	5.04	4.58	4.14	3.78	3.51	3.32	3.15	2.97	2.78
RS1_16_6	TL	4.90	4.62	4.26	3.93	3.68	3.52	3.40	3.31	3.19
RS1_16_7	TL	5.28	4.88	4.45	4.06	3.75	3.52	3.33	3.14	2.94
RS1_16_8	TL	4.60	4.36	4.08	3.79	3.54	3.33	3.15	2.99	2.83
RS1_16_9	TL	4.70	4.35	4.00	3.70	3.46	3.27	3.11	2.97	2.81
RS1_16_10	TL	4.86	4.58	4.23	3.91	3.65	3.46	3.30	3.16	3.00
RS1_16_12	TL	4.26	3.96	3.68	3.48	3.37	3.33	3.31	3.29	3.24
RS1_16_15	RTL	4.47	4.24	4.00	3.83	3.75	3.74	3.75	3.74	3.68
RS1_16_16	RTL	5.05	4.65	4.33	4.14	4.05	4.03	4.01	3.95	3.84
RS1_16_20	RTL	4.93	4.58	4.28	4.08	3.97	3.92	3.86	3.78	3.66
RS1_16_19	RTL	4.73	4.44	4.17	3.99	3.90	3.88	3.86	3.82	3.74
RS1_16_21	RTL	4.75	4.47	4.24	4.10	4.05	4.07	4.09	4.08	4.02
RS1_16_18	RTL	4.54	4.28	4.07	3.96	3.96	4.01	4.07	4.10	4.06
RS1_16_14	RTL	4.67	4.31	4.06	3.93	3.89	3.88	3.87	3.83	3.76
RS1_16_17	RTL	4.50	4.23	3.98	3.81	3.72	3.72	3.74	3.75	3.71
RS1_16_13	RTL	4.46	4.20	4.00	3.86	3.79	3.78	3.76	3.71	3.60
RS2_16_MI_19	RTL	4.45	4.27	4.06	3.91	3.85	3.86	3.88	3.87	3.81
RS2_16_MI_20	RTL	4.48	4.26	4.05	3.89	3.82	3.81	3.82	3.80	3.73
RS2_16_MI_21	RTL	4.42	4.19	4.00	3.90	3.86	3.85	3.84	3.79	3.70
RS2_16_MI_22	RTL	4.18	4.07	3.95	3.88	3.83	3.80	3.77	3.72	3.65
RS2_16_MI_24	RTL	4.28	3.88	3.58	3.41	3.34	3.33	3.34	3.32	3.25
RS2_16_MI_25	RTL	4.39	4.11	3.88	3.73	3.68	3.69	3.69	3.68	3.61
RS2_16_MI_30	Unit 2	4.01	4.36	4.66	4.96	5.30	5.64	5.91	5.86	6.02
RS2_16_MI_31	Unit 2	3.80	4.12	4.43	4.78	5.17	5.58	5.93	6.16	5.99
RS2_16_MI_32	Unit 2	3.91	4.15	4.36	4.60	4.90	5.21	5.47	5.42	5.61
RS2_16_MI_33	Unit 2	3.86	4.17	4.49	4.85	5.28	5.73	6.08	6.04	6.19
RS2_16_MI_34	Unit 2	5.43	5.60	5.47	5.31	5.21	5.15	5.07	4.93	4.71
RS2_16_MI_35	Unit 2	2.72	3.37	4.03	4.69	5.33	5.94	6.53	7.09	7.62

Sample ID	Sample Unit	Size (µm)								
		2.75	2.31	1.94	1.64	1.38	1.16	0.972	0.817	0.687
RS1_16_5	TL	1.93	1.52	1.12	0.78	0.53	0.37	0.00	0.00	0.00
RS1_16_6	TL	2.39	1.91	1.39	0.95	0.64	0.44	0.32	0.00	0.00
RS1_16_7	TL	2.03	1.60	1.17	0.80	0.54	0.37	0.00	0.00	0.00
RS1_16_8	TL	2.02	1.59	1.17	0.81	0.56	0.39	0.00	0.00	0.00
RS1_16_9	TL	2.03	1.62	1.20	0.84	0.58	0.41	0.00	0.00	0.00
RS1_16_10	TL	2.16	1.72	1.27	0.89	0.61	0.43	0.32	0.00	0.00
RS1_16_12	TL	2.56	2.08	1.57	1.12	0.77	0.55	0.41	0.32	0.00
RS1_16_15	RTL	2.87	2.32	1.74	1.23	0.86	0.60	0.45	0.35	0.00
RS1_16_16	RTL	2.92	2.33	1.71	1.18	0.79	0.54	0.38	0.00	0.00
RS1_16_20	RTL	2.74	2.21	1.66	1.19	0.83	0.59	0.44	0.34	0.00
RS1_16_19	RTL	2.90	2.36	1.77	1.26	0.88	0.62	0.46	0.36	0.00
RS1_16_21	RTL	3.14	2.54	1.90	1.34	0.92	0.64	0.47	0.37	0.00
RS1_16_18	RTL	3.18	2.56	1.91	1.34	0.92	0.64	0.47	0.37	0.00
RS1_16_14	RTL	2.95	2.40	1.79	1.27	0.87	0.61	0.45	0.35	0.00
RS1_16_17	RTL	2.92	2.37	1.79	1.27	0.88	0.62	0.46	0.36	0.00
RS1_16_13	RTL	2.75	2.22	1.67	1.18	0.81	0.57	0.42	0.33	0.00
RS2_16_MI_19	RTL	2.95	2.40	1.81	1.28	0.89	0.63	0.47	0.37	0.00
RS2_16_MI_20	RTL	2.91	2.37	1.78	1.27	0.88	0.62	0.46	0.36	0.00
RS2_16_MI_21	RTL	2.85	2.30	1.71	1.20	0.82	0.57	0.42	0.33	0.00
RS2_16_MI_22	RTL	2.87	2.34	1.77	1.26	0.88	0.63	0.47	0.37	0.31
RS2_16_MI_24	RTL	2.51	2.03	1.53	1.09	0.76	0.54	0.40	0.31	0.00
RS2_16_MI_25	RTL	2.78	2.24	1.68	1.19	0.82	0.58	0.43	0.33	0.00
RS2_16_MI_30	Unit 2	4.40	3.34	2.32	1.50	0.95	0.62	0.43	0.32	0.00
RS2_16_MI_31	Unit 2	4.60	3.53	2.45	1.59	1.01	0.66	0.46	0.34	0.00
RS2_16_MI_32	Unit 2	4.11	3.16	2.21	1.45	0.93	0.61	0.43	0.33	0.00
RS2_16_MI_33	Unit 2	4.14	3.04	2.03	1.27	0.78	0.50	0.34	0.00	0.00
RS2_16_MI_34	Unit 2	3.28	2.53	1.79	1.20	0.79	0.53	0.38	0.00	0.00
RS2_16_MI_35	Unit 2	7.58	6.38	4.80	3.29	2.16	1.42	0.98	0.72	0.56

Sample ID	Sample Unit	Size (µm)								
		0.409	0.344	0.289	0.243	0.204	0.172	0.145	0.122	0.102
RS1_16_5	TL	0.00	0.00	0.00	0.00	0.00	0.00	0.00	0.00	0.00
RS1_16_6	TL	0.00	0.00	0.00	0.00	0.00	0.00	0.00	0.00	0.00
RS1_16_7	TL	0.00	0.00	0.00	0.00	0.00	0.00	0.00	0.00	0.00
RS1_16_8	TL	0.00	0.00	0.00	0.00	0.00	0.00	0.00	0.00	0.00
RS1_16_9	TL	0.00	0.00	0.00	0.00	0.00	0.00	0.00	0.00	0.00
RS1_16_10	TL	0.00	0.00	0.00	0.00	0.00	0.00	0.00	0.00	0.00
RS1_16_12	TL	0.00	0.00	0.00	0.00	0.00	0.00	0.00	0.00	0.00
RS1_16_15	RTL	0.00	0.00	0.00	0.00	0.00	0.00	0.00	0.00	0.00
RS1_16_16	RTL	0.00	0.00	0.00	0.00	0.00	0.00	0.00	0.00	0.00
RS1_16_20	RTL	0.00	0.00	0.00	0.00	0.00	0.00	0.00	0.00	0.00
RS1_16_19	RTL	0.00	0.00	0.00	0.00	0.00	0.00	0.00	0.00	0.00
RS1_16_21	RTL	0.00	0.00	0.00	0.00	0.00	0.00	0.00	0.00	0.00
RS1_16_18	RTL	0.00	0.00	0.00	0.00	0.00	0.00	0.00	0.00	0.00
RS1_16_14	RTL	0.00	0.00	0.00	0.00	0.00	0.00	0.00	0.00	0.00
RS1_16_17	RTL	0.00	0.00	0.00	0.00	0.00	0.00	0.00	0.00	0.00
RS1_16_13	RTL	0.00	0.00	0.00	0.00	0.00	0.00	0.00	0.00	0.00
RS2_16_MI_19	RTL	0.00	0.00	0.00	0.00	0.00	0.00	0.00	0.00	0.00
RS2_16_MI_20	RTL	0.00	0.00	0.00	0.00	0.00	0.00	0.00	0.00	0.00
RS2_16_MI_21	RTL	0.00	0.00	0.00	0.00	0.00	0.00	0.00	0.00	0.00
RS2_16_MI_22	RTL	0.00	0.00	0.00	0.00	0.00	0.00	0.00	0.00	0.00
RS2_16_MI_24	RTL	0.00	0.00	0.00	0.00	0.00	0.00	0.00	0.00	0.00
RS2_16_MI_25	RTL	0.00	0.00	0.00	0.00	0.00	0.00	0.00	0.00	0.00
RS2_16_MI_30	Unit 2	0.00	0.00	0.00	0.00	0.00	0.00	0.00	0.00	0.00
RS2_16_MI_31	Unit 2	0.00	0.00	0.00	0.00	0.00	0.00	0.00	0.00	0.00
RS2_16_MI_32	Unit 2	0.00	0.00	0.00	0.00	0.00	0.00	0.00	0.00	0.00
RS2_16_MI_33	Unit 2	0.00	0.00	0.00	0.00	0.00	0.00	0.00	0.00	0.00
RS2_16_MI_34	Unit 2	0.00	0.00	0.00	0.00	0.00	0.00	0.00	0.00	0.00
RS2_16_MI_35	Unit 2	0.00	0.00	0.00	0.00	0.00	0.00	0.00	0.00	0.00

Sample ID	Sample Unit	Size (µm)						MV (µm)	MN (µm)
		0.0610	0.0510	0.0430	0.0360	0.0300	0.0255		
RS1_16_5	TL	0.00	0.00	0.00	0.00	0.00	0.00	34.92	2.03
RS1_16_6	TL	0.00	0.00	0.00	0.00	0.00	0.00	32.71	1.78
RS1_16_7	TL	0.00	0.00	0.00	0.00	0.00	0.00	32.37	2.04
RS1_16_8	TL	0.00	0.00	0.00	0.00	0.00	0.00	36.68	2.01
RS1_16_9	TL	0.00	0.00	0.00	0.00	0.00	0.00	37.18	1.99
RS1_16_10	TL	0.00	0.00	0.00	0.00	0.00	0.00	36.10	1.76
RS1_16_12	TL	0.00	0.00	0.00	0.00	0.00	0.00	43.06	1.49
RS1_16_15	RTL	0.00	0.00	0.00	0.00	0.00	0.00	36.34	1.50
RS1_16_16	RTL	0.00	0.00	0.00	0.00	0.00	0.00	24.35	1.77
RS1_16_20	RTL	0.00	0.00	0.00	0.00	0.00	0.00	27.91	1.50
RS1_16_19	RTL	0.00	0.00	0.00	0.00	0.00	0.00	29.84	1.49
RS1_16_21	RTL	0.00	0.00	0.00	0.00	0.00	0.00	27.68	1.51
RS1_16_18	RTL	0.00	0.00	0.00	0.00	0.00	0.00	29.32	1.51
RS1_16_14	RTL	0.00	0.00	0.00	0.00	0.00	0.00	26.84	1.50
RS1_16_17	RTL	0.00	0.00	0.00	0.00	0.00	0.00	34.33	1.49
RS1_16_13	RTL	0.00	0.00	0.00	0.00	0.00	0.00	35.46	1.51
RS2_16_MI_19	RTL	0.00	0.00	0.00	0.00	0.00	0.00	37.16	1.49
RS2_16_MI_20	RTL	0.00	0.00	0.00	0.00	0.00	0.00	33.58	1.49
RS2_16_MI_21	RTL	0.00	0.00	0.00	0.00	0.00	0.00	36.87	1.52
RS2_16_MI_22	RTL	0.00	0.00	0.00	0.00	0.00	0.00	40.90	1.27
RS2_16_MI_24	RTL	0.00	0.00	0.00	0.00	0.00	0.00	36.20	1.50
RS2_16_MI_25	RTL	0.00	0.00	0.00	0.00	0.00	0.00	37.64	1.50
RS2_16_MI_30	Unit 2	0.00	0.00	0.00	0.00	0.00	0.00	32.92	1.66
RS2_16_MI_31	Unit 2	0.00	0.00	0.00	0.00	0.00	0.00	28.81	1.64
RS2_16_MI_32	Unit 2	0.00	0.00	0.00	0.00	0.00	0.00	38.93	1.63
RS2_16_MI_33	Unit 2	0.00	0.00	0.00	0.00	0.00	0.00	35.05	1.93
RS2_16_MI_34	Unit 2	0.00	0.00	0.00	0.00	0.00	0.00	23.37	1.84
RS2_16_MI_35	Unit 2	0.00	0.00	0.00	0.00	0.00	0.00	7.73	1.16

Sample ID	Sample Unit	SD	Mz	aI	Ski	Kg	10 %tile	20 %tile
RS1_16_5	TL	29.84	30.76	31.68	0.54	1.17	3.62	6.54
RS1_16_6	TL	29.00	28.71	30.63	0.58	1.15	3.11	5.40
RS1_16_7	TL	27.26	28.30	29.08	0.54	1.17	3.51	6.20
RS1_16_8	TL	32.72	32.80	33.69	0.55	1.07	3.52	6.36
RS1_16_9	TL	33.03	32.97	34.25	0.56	1.09	3.48	6.33
RS1_16_10	TL	32.22	31.47	34.35	0.60	1.20	3.28	5.83
RS1_16_12	TL	37.44	34.48	43.70	0.67	1.43	2.86	4.97
RS1_16_15	RTL	29.01	27.40	36.42	0.67	1.61	2.69	4.43
RS1_16_16	RTL	20.34	21.25	21.29	0.52	1.07	2.77	4.48
RS1_16_20	RTL	22.21	22.75	24.75	0.56	1.23	2.75	4.56
RS1_16_19	RTL	23.95	23.70	27.07	0.60	1.27	2.66	4.37
RS1_16_21	RTL	21.90	21.71	25.01	0.61	1.30	2.57	4.10
RS1_16_18	RTL	23.55	22.87	27.29	0.64	1.35	2.56	4.06
RS1_16_14	RTL	22.20	22.54	24.07	0.55	1.15	2.65	4.33
RS1_16_17	RTL	26.94	25.92	33.21	0.64	1.54	2.65	4.36
RS1_16_13	RTL	28.81	27.51	34.46	0.65	1.48	2.76	4.59
RS2_16_MI_19	RTL	29.63	27.46	38.18	0.70	1.73	2.63	4.30
RS2_16_MI_20	RTL	27.04	25.88	32.35	0.65	1.45	2.65	4.36
RS2_16_MI_21	RTL	29.62	27.79	37.36	0.68	1.65	2.72	4.47
RS2_16_MI_22	RTL	32.26	29.45	43.18	0.71	1.85	2.61	4.34
RS2_16_MI_24	RTL	28.42	28.59	33.27	0.56	1.35	2.90	5.03
RS2_16_MI_25	RTL	30.08	28.44	37.43	0.66	1.58	2.74	4.55
RS2_16_MI_30	Unit 2	18.32	16.92	37.61	0.82	4.31	2.37	3.36
RS2_16_MI_31	Unit 2	17.62	16.28	31.37	0.82	3.45	2.31	3.26
RS2_16_MI_32	Unit 2	25.87	22.35	45.44	0.85	3.70	2.41	3.48
RS2_16_MI_33	Unit 2	21.70	19.41	40.21	0.84	3.94	2.53	3.56
RS2_16_MI_34	Unit 2	16.22	16.90	20.45	0.65	1.65	2.68	4.07
RS2_16_MI_35	Unit 2	5.09	6.23	6.15	0.63	1.58	1.67	2.27

Sample ID	Sample Unit	50 %tile	60 %tile	70 %tile	80 %tile	90 %tile	95 %tile
RS1_16_5	TL	22.13	29.93	40.46	55.97	84.34	113.10
RS1_16_6	TL	19.37	27.17	38.01	53.54	81.30	108.60
RS1_16_7	TL	20.35	27.60	37.39	51.45	77.35	104.40
RS1_16_8	TL	22.79	32.15	44.35	61.41	89.48	116.80
RS1_16_9	TL	22.73	31.73	44.21	61.70	90.76	119.40
RS1_16_10	TL	20.60	28.99	40.67	58.63	91.33	122.70
RS1_16_12	TL	20.52	30.16	44.24	65.84	110.80	166.90
RS1_16_15	RTL	16.84	24.48	35.26	51.56	88.77	146.60
RS1_16_16	RTL	15.61	21.73	29.26	39.12	55.94	75.42
RS1_16_20	RTL	16.27	22.71	30.87	41.92	62.93	92.01
RS1_16_19	RTL	15.96	22.76	31.73	44.46	67.96	101.50
RS1_16_21	RTL	14.47	20.79	29.05	40.63	62.79	94.64
RS1_16_18	RTL	14.67	21.38	30.37	43.18	67.98	104.20
RS1_16_14	RTL	16.04	22.75	30.86	41.90	61.94	87.51
RS1_16_17	RTL	16.66	23.99	33.85	48.43	81.08	132.10
RS1_16_13	RTL	17.33	25.00	35.61	51.57	85.86	134.40
RS2_16_MI_19	RTL	15.97	23.47	34.43	51.77	92.78	156.10
RS2_16_MI_20	RTL	16.35	23.78	33.92	48.87	79.78	126.20
RS2_16_MI_21	RTL	16.74	24.37	35.30	52.21	91.46	150.80
RS2_16_MI_22	RTL	16.66	24.94	36.96	55.68	105.00	180.40
RS2_16_MI_24	RTL	20.77	28.81	38.69	52.56	82.18	127.80
RS2_16_MI_25	RTL	17.67	25.60	36.75	53.49	91.39	149.70
RS2_16_MI_30	Unit 2	8.20	11.58	17.21	29.08	85.48	189.60
RS2_16_MI_31	Unit 2	7.85	11.14	16.83	28.69	68.46	150.70
RS2_16_MI_32	Unit 2	9.22	13.61	21.25	38.82	119.30	216.40
RS2_16_MI_33	Unit 2	8.55	12.24	18.76	33.43	93.92	195.70
RS2_16_MI_34	Unit 2	11.29	15.43	21.22	30.25	50.32	83.41
RS2_16_MI_35	Unit 2	4.43	5.65	7.45	10.39	16.64	25.06

Table A5 Stable water isotopes analysis results

Sample ID	Sample Unit	δD (‰)	$\delta^{18}O$ (‰)	D-Excess (‰)
RS1-16-5	TL	-170.06	-21.84	4.67
RS1-16-6	TL	-158.60	-20.48	5.21
RS1-16-7	TL	-158.26	-20.41	4.99
RS1-16-8	TL	-157.78	-20.52	6.38
RS1-16-16	RTL	-158.39	-20.64	6.74
RS1-16-17	RTL	-156.54	-20.38	6.50
RS1-16-18	RTL	-174.22	-22.68	7.24
RS1-16-19	RTL	-173.19	-22.36	5.72
RS2-16-MI-1	Unit 1	-233.22	-29.70	4.40
RS2-16-MI-2	Unit 1	-231.30	-29.51	4.77
RS2-16-MI-3	Unit 1	-228.62	-29.01	3.46
RS2-16-MI-4	Unit 1	-230.29	-29.46	5.38
RS2-16-MI-5	Unit 1	-234.70	-30.01	5.38
RS2-16-MI-7	Unit 1	-235.82	-30.17	5.52
RS2-16-MI-8	Unit 1	-241.34	-31.05	7.08
RS2-16-MI-9	Unit 1	-240.70	-30.93	6.70
RS2-16-MI-10	Unit 1	-239.20	-30.68	6.28
RS2-16-MI-11	Unit 1	-236.03	-30.29	6.30
RS2-16-MI-12	Unit 1	-236.43	-30.42	6.91
RS2-16-MI-13	Unit 1	-238.34	-30.40	4.89
RS2-16-MI-14	Unit 1	-240.22	-30.77	5.96
RS2-16-MI-15	Unit 1	-238.69	-30.74	7.24
RS2-16-MI-16	Unit 1	-242.50	-31.18	6.95
RS2-16-MI-17	Unit 1	-236.11	-30.24	5.82
RS2-16-MI-18	Unit 1	-232.04	-29.67	5.28
RS2-16-MI-26	Unit 2	-232.54	-29.70	5.05
RS2-16-MI-27	Unit 2	-228.99	-29.07	3.59
RS2-16-MI-28	Unit 2	-235.38	-30.01	4.73
RS2-16-MI-29	Unit 2	-245.55	-31.33	5.08
RS2-16-MI-31	Unit 2	-242.96	-30.87	4.02
RS2-16-MI-32	Unit 2	-240.53	-30.56	3.99
RS2-16-MI-33	Unit 2	-238.61	-30.46	5.06
RS2-16-MI-34	Unit 2	-234.65	-29.36	0.22
RS2-16-MI-35	Unit 2	-227.23	-28.69	2.30
RS2-16-MI-36	Unit 3	-224.02	-28.14	1.10
RS2-16-MI-37	Unit 3	-223.55	-28.19	1.95
RS2-16-MI-38	Unit 3	-222.67	-28.01	1.40

RS2-16-MI-39	Unit 3	-222.52	-27.88	0.53
RS2-16-MI-40	Unit 3	-223.36	-27.94	0.18
RS2-16-MI-41	Unit 3	-223.85	-28.18	1.60
RS2-16-MI-42	Unit 3	-218.45	-27.30	-0.02
RS2-16-MI-43	Unit 3	-223.21	-28.15	2.01
RS2-16-MI-44	Unit 3	-220.51	-27.64	0.62
RS2-16-MI-45	Unit 3	-222.75	-27.80	-0.38
RS2-16-MI-46	Unit 3	-222.63	-27.87	0.36
RS2-16-MI-47	Unit 3	-219.87	-27.48	-0.04
RS2-16-MI-48	Unit 3	-220.34	-27.47	-0.54
RS2-16-MI-49	Unit 3	-222.11	-27.87	0.87
RS2-16-MI-51	Unit 4	-239.97	-31.13	9.09
RS2-16-MI-53	Unit 4	-246.08	-31.98	9.80
RS2-16-MI-54	Unit 4	-239.68	-31.01	8.37
RS2-16-MI-55	Unit 4	-230.75	-29.47	5.01
RS2-16-MI-56	Unit 4	-238.64	-30.96	9.08
RS2-16-MI-57	Unit 4	-240.95	-31.27	9.23
RS2-16-MI-59	Unit 4	-243.05	-31.50	8.97
RS2-16-MI-60	Unit 4	-241.48	-31.30	8.91
RS2-16-MI-61	Unit 4	-247.06	-31.90	8.14
RS2-16-MI-62	Unit 4	-244.21	-31.69	9.28
RS2-16-MI-63	Unit 4	-242.41	-31.13	6.60
RS2-16-MI-64	Unit 4	-238.37	-30.65	6.87

Table A6 Loss on ignition (LOI) procedure results

Sample ID	Sample Unit	LOI_{105} (g)	LOI_{550} (g)	LOI_{950} (g)	Moisture (%)	Organic Matter (%)	Organic Carbon (%)[a]	Carbonates (%)
RS1-16-1	TL	0.43	0.39	0.40	3.25	92.17	46.09	0.19
RS1-16-2	TL	0.29	0.27	0.28	4.27	94.48	47.24	0.28
RS1-16-3	TL	0.37	0.35	0.35	3.87	94.14	47.07	0.30
RS1-16-4	TL	0.70	0.57	0.57	2.89	80.71	40.36	0.40
RS1-16-5	TL	4.77	0.62	0.65	0.42	12.59	6.30	0.77
RS1-16-6	TL	5.62	0.49	0.53	0.35	8.46	4.23	0.79
RS1-16-7	TL	6.16	0.71	0.75	0.32	11.25	5.63	0.81
RS1-16-8	TL	4.93	0.89	0.92	0.45	17.62	8.81	0.80
RS1-16-9	TL	4.89	0.67	0.70	0.37	13.47	6.74	0.83
RS1-16-10	TL	4.45	0.92	0.95	0.52	20.25	10.13	0.82
RS1-16-12	TL	2.15	0.28	0.30	0.49	12.77	6.39	0.90
RS1-16-13	RTL	1.35	0.12	0.13	0.44	8.50	4.25	1.55
RS1-16-14	RTL	3.82	0.30	0.35	0.25	7.74	3.87	1.63
RS1-16-15	RTL	3.70	0.21	0.27	0.24	5.57	2.79	2.00
RS1-16-16	RTL	3.22	0.18	0.22	0.29	5.24	2.62	1.88
RS1-16-17	RTL	6.09	0.38	0.49	0.04	6.28	3.14	2.34
RS1-16-18	RTL	3.51	0.21	0.27	0.01	5.90	2.95	2.52
RS1-16-19	RTL	3.59	0.18	0.26	0.02	5.02	2.51	2.92
RS1-16-19	RTL	3.37	0.15	0.21	0.16	4.29	2.15	2.59
RS1-16-20	RTL	2.71	0.14	0.20	0.08	4.92	2.46	3.19
RS1-16-21	RTL	3.99	0.23	0.31	0.05	5.75	2.88	2.80
RS2-16-MI-19	RTL	2.39	0.12	0.17	0.11	4.82	2.41	3.08
RS2-16-MI-20	RTL	2.37	0.13	0.18	0.14	5.24	2.62	3.20
RS2-16-MI-21	RTL	3.62	0.18	0.26	0.12	4.89	2.45	2.96
RS2-16-MI-22	RTL	1.47	0.13	0.19	0.21	8.62	4.31	5.21
RS2-16-MI-23	RTL	3.09	1.05	1.10	0.04	33.95	16.98	2.29
RS2-16-MI-24	RTL	3.47	0.17	0.24	0.06	4.76	2.38	2.87
RS2-16-MI-25	RTL	3.38	0.17	0.24	0.09	4.89	2.45	2.92
RS2-16-MI-30	Unit 2	2.78	0.14	0.21	0.40	4.78	2.39	3.31
RS2-16-MI-31	Unit 2	2.49	0.12	0.19	0.35	4.55	2.28	3.95
RS2-16-MI-32	Unit 2	2.82	0.14	0.22	0.37	4.76	2.38	3.63
RS2-16-MI-33	Unit 2	3.15	0.17	0.25	0.82	4.58	2.29	3.35
RS2-16-MI-34	Unit 2	2.73	0.13	0.20	0.72	4.05	2.03	3.42

[a] Obtained from the organic matter content using a conversion factor of 2 (Pribyl, 2010).

APPENDIX B: A.E. LALONDE AMS LABORATORY RESULTS

A.E. Lalonde AMS Laboratory
Canadian centre for AMS and environmental radionuclide research

February 8, 2017

Prof. Denis Lacelle
(Roxanne Frappier)
University of Ottawa
Department of Geography
60 University, Simard Hall
Ottawa, ON
K1N 6N5
562-5800-x1059
dlacelle@uottawa.ca

RE: Radiocarbon analysis results, Peel Plateau, NWT

Dear Professor Lacelle,

We are pleased to provide radiocarbon analysis results for the five samples of organics submitted mid-January. Sample RS2-16-MI-23-A was very small so the precision is low. Otherwise, there were no issues during sample processing.

The preparator for your samples was Carley Crann, and the AMS analyst was Dr. Xiao-Lei Zhao. If you have specific questions about the analyses or calibration, please direct them to ccrann@uottawa.ca. If this data is used in publication or for a graduate thesis, we would appreciate a copy of the abstract for our records. In the interest of future researchers, we encourage you to take the time to submit your radiocarbon results to either the Canadian Archaeological Radiocarbon Database (CARD), or to the Neotoma Paleoecology Database.

Thank you for choosing the André E. Lalonde AMS Laboratory. We look forward to working with you again.

Sincerely,

Dr. W. E. Kieser
Director, A. E. Lalonde AMS Laboratory
Associate Professor, Department of Physics
25 Templeton St., Ottawa, ON, K1N 6N5, Canada
www.ams.uottawa.ca

Sample Processing
Sample pretreatment techniques and definitions of media codes can be found in Crann et al. (2016). For more information about the equipment used for sample preparation, please see St-Jean et al. (2016). Both manuscripts can be found at www.ams.uottawa.ca/Research

Reporting of Data
In this analysis report, we have followed the conventions recommended by Millard (2014).

Radiocarbon Analysis
Radiocarbon analyses are performed on a 3MV tandem accelerator mass spectrometer built by High Voltage Engineering (HVE). $^{12,13,14}C^{+3}$ ions are measured at 2.5 MV terminal voltage with Ar stripping. The fraction modern carbon, $F^{14}C$, is calculated according to Reimer et al. (2004) as the ratio of the sample $^{14}C/^{12}C$ ratio to the standard $^{14}C/^{12}C$ ratio (in our case Ox-II) measured in the same data block. Both $^{14}C/^{12}C$ ratios are background-corrected and the result is corrected for spectrometer and preparation fractionation using the AMS measured $^{13}C/^{12}C$ ratio and is normalized to $\delta^{13}C$ (PDB). Radiocarbon ages are calculated as $-8033\ln(F^{14}C)$ and reported in ^{14}C yr BP (BP=AD 1950) as described by Stuiver and Polach (1977). The errors on 14C ages (1σ) are based on counting statistics and $^{14}C/^{12}C$ and $^{13}C/^{12}C$ variation between data blocks. We do not report $\delta^{13}C$ as it is measured on the AMS and contains machine fractionation.

Calibration
Calibration was performed using OxCal v4.2.4 (Bronk Ramsey, 2009). Calibrated results are given as a range (or ranges) with an associated probability as point estimates (mean, median) cannot represent the uncertainties involved (Millard, 2014). We acknowledge that point estimates are often desired and are thus included on the calibration plots in the Appendix, but we recommend that data tables used in publication maintain calibrated age ranges.

Where the $F^{14}C$ is less than 1, the IntCal13 calibration curve was used for Northern Hemisphere samples and ShCal13 for Southern Hemisphere samples (Reimer et al., 2013).

For samples with an $F^{14}C$ greater than 1, the post-bomb atmospheric curve was used (Hua et al., 2013). Post-bomb samples have two age ranges due to calibration on both sides of the bomb pulse. There are methods for deciding which side of the bomb pulse to select as the more appropriate date so feel free to contact us for further information.

Samples that calibrate between the 1700's and early 1950's will always result in a calibrated age range covering the majority of this period. This is due to the "Seuss Effect", which is a flat portion of the calibration curve caused by the burning of fossil fuels.

Rounding
Calibrated ages and ranges are rounded to the nearest year which may be too precise in many instances. Users are advised to round results to the nearest 10 yr for samples with standard deviation in the radiocarbon age greater than 50 yr, but rounding should only be done at the final reporting stage as intermediate rounding may introduce errors (Millard, 2014).

References
Bronk Ramsey C. 2009. Bayesian analysis of radiocarbon dates. *Radiocarbon* 51: 337–360.

Crann CA, Murseli S, St-Jean G, Zhao X, Clark ID, Kieser WE. 2016. First status report on radiocarbon sample preparation at the A.E. Lalonde AMS Laboratory (Ottawa, Canada). *Radiocarbon.* In Press.

Hua Q, Barbetti M, Rakowski AZ. 2013. Atmospheric radiocarbon for the period 1950-2010. *Radiocarbon* 55(4): 2059–2072.

Millard A. 2014. Conventions for reporting radiocarbon determinations. *Radiocarbon* 56(2): 555–559.

Reimer PJ, Bard E, Bayliss A, Beck JW, Blackwell PG, Bronk Ramsey C, Buck CE, Cheng H, Edwards RL, Friedrich M, Grootes PM, Guilderson TP, Haflidason H, Hajdas I, Hatté C, Heaton TJ, Hogg AG, Hughen KA, Kaiser KF, Kromer B, Manning SW, Niu M, Reimer RW, Richards DA, Scott EM, Southon JR, Turney CSM, van der Plicht J. 2013. IntCal13 and MARINE13 radiocarbon age calibration curves 0-50000 years calBP. Radiocarbon 55(4): 1869–1887.

St-Jean G, Kieser WE, Crann CA, Murseli S. 2016. Semi-automated equipment for CO2 purification and graphitization at the A.E. Lalonde AMS Laboratory (Canada). *Radiocarbon*. In press.

Table 1. Radiocarbon results. Calibration was performed using OxCal v4.2.4 (Bronk Ramsey, 2009) and the IntCal13 calibration curve (Reimer et al., 2013). Material codes are described in Crann et al. (2016).

Lab ID	Submitter ID	Material	Mat. Code	^{14}C yr BP	±	$F^{14}C$	±	cal BP
UOC-3457	RS2-16-MI-23-A	macrofossil	AAA	8717	104	0.3378	0.0044	10152–10053(8.3%) 10044–9986(4.0%) 9962–9531(83.1%)
UOC-3458	RS2-16-MI-23-B	leaves fragment	AAA	8442	68	0.3496	0.0030	9540–9302(95.4%)
UOC-3459	RS2-16-MI-23-C	wood	AAA	8566	36	0.3443	0.0015	9560–9485(95.4%)
UOC-3460	RS2-16-MI-23-D	bulk (<1mm; >0.5mm)	AAA	8488	39	0.3476	0.0017	9539–9453(95.4%)
UOC-3461	RS1-16-11	wood	AAA	2706	31	0.7140	0.0028	2860–2755(95.4%)

APPENDIX C: EXTERNAL DATA

Table C1 Radiocarbon dates used in Fig. 6.1

Lab ID	^{14}C Age (yr BP)	cal yr BP[b]	Median cal yr BP	Material type	Source
TO-8890	150±50	286-56(78.2%)	150	Organics	Lacelle et al., 2004
TO-8891	270±50	479-269(81.3%)	341	Organics	Lacelle et al., 2004
TO-8895	350±50	499-308(95.4%)	400	Organics	Lacelle et al., 2004
TO-8893	350±50	499-308(95.4%)	400	Organics	Lacelle et al., 2004
TO-8898	790±50	796-658(95.1%)	716	Organics	Lacelle, Bjornson and Lauriol, 2010
TO-8892	2040±50	2128-1887(95.4%)	2002	Organics	Lacelle et al., 2004
TO-8896	4230±60	4883-4569(94.2%)	4744	Organics	Lacelle, Bjornson and Lauriol, 2010
TO-8899	6820±60	7786-7575(95.4%)	7657	Organics	Lacelle, Bjornson and Lauriol, 2010
TO-8888	8120±70	9288-8858(91%)	9071	Organics	Lacelle et al., 2004
TO-8887	8180±70	9320-8997(92.2%)	9144	Organics	Lacelle et al., 2004
TO-8894	8240±70	9414-9027(95.4%)	9216	Organics	Lacelle et al., 2004
UOC-3457-3460[a]	−	−	9498.3	Organics	This study
TO-8889	8560±70	9688-9443(95.4%)	9536	Peat	Lacelle et al., 2004
TO-8897	9070±80	10439-10120(83.9%)	10236	Organics	Lacelle et al., 2004

[a] Mean of four samples taken from a buried organics section at Roger Thaw Slump (see Appendix B)

[b] Calibration was achieved using OxCal v4.3 (Bronk Ramsey, 2017) and the IntCal13 calibration curve (Reimer et al., 2013).

APPENDIX D: R CODE

Code 1: Basic code for box plots

```
> #Import data
> Data=read.csv(file.choose())

> #View data
> Data

> #Plot
> boxplot(Data)
```

Code 2: Basic code for line plot with trendline

```
> #Import data
> Data1=read.csv(file.choose())
> Data2=read.csv(file.choose())
> Data3=read.csv(file.choose())
> DataAv=read.csv(file.choose())

> #View data
> Data1
> Data2
> Data3
> DataAv

> #Plot 3 lines
> plot(Data1$X,Data1$Y)
> lines(Data2$X,Data2$Y)
> lines(Data3$X,Data3$Y)

> #Add trendline based on average of 3 data sets
> lines(DataAv$X,DataAv$Y,col="NA")
> abline(lm(Data$Y~Data$X))
```

Code 3: Adding a linear regression line

```
> #Import data
> Data=read.csv(file.choose())

> #View data
> Data

> #Add linear regression
> fit_Data<- glm(Data$Y~Data$X)
```

```
> co_Data<-coef(fit_Data)
> abline(fit_Data, col="#7A8B8B")

> #View regression coefficients
> co_Data
```

Code 4: Calculating Pearson product-moment correlation coefficient

```
> #Calculate Pearson correlation coefficient
> cor_Data<-cor.test(Data$X, Data$Y)

> #View Pearson correlation coefficient
> cor_Data
```